

Cyclotron Radiation Emission Spectroscopy of Electrons from Tritium Beta Decay and $^{83\text{m}}\text{Kr}$ Internal Conversion

A. Ashtari Esfahani,^{1, a} S. Böser,² N. Buzinsky,^{3, b} M. C. Carmona-Benitez,⁴ C. Claessens,^{1, 2, c} L. de Viveiros,⁴ P. J. Doe,¹ M. Fertl,² J. A. Formaggio,³ J. K. Gaison,⁵ L. Gladstone,⁶ M. Guigue,⁷ J. Hartse,¹ K. M. Heeger,⁸ X. Huyan,^{5, d} A. M. Jones,^{5, e} K. Kazkaz,⁹ B. H. LaRoque,⁵ M. Li,³ A. Lindman,² E. Machado,¹ A. Marsteller,¹ C. Matthé,² R. Mohiuddin,⁶ B. Monreal,⁶ R. Mueller,⁴ J. A. Nikkel,⁸ E. Novitski,¹ N. S. Oblath,⁵ J. I. Peña,³ W. Pettus,¹⁰ R. Reimann,² R. G. H. Robertson,¹ D. Rosa De Jesús,⁵ G. Rybka,¹ L. Saldaña,⁸ M. Schram,^{5, f} P. L. Slocum,⁸ J. Stachurska,³ Y.-H. Sun,⁶ P. T. Surukuchi,⁸ J. R. Tedeschi,⁵ A. B. Telles,⁸ F. Thomas,² M. Thomas,^{5, g} L. A. Thorne,² T. Thümmel,¹¹ L. Tvrznikova,^{9, h} W. Van De Pontseele,³ B. A. VanDevender,^{1, 5} J. Weintroub,¹² T. E. Weiss,^{8, i} T. Wendler,⁴ A. Young,^{12, j} E. Zayas,³ and A. Ziegler⁴

(Project 8 Collaboration)

¹*Center for Experimental Nuclear Physics and Astrophysics and Department of Physics, University of Washington, Seattle, WA 98195, USA*

²*Institute for Physics, Johannes Gutenberg University Mainz, 55128 Mainz, Germany*

³*Laboratory for Nuclear Science, Massachusetts Institute of Technology, Cambridge, MA 02139, USA*

⁴*Department of Physics, Pennsylvania State University, University Park, PA 16802, USA*

⁵*Pacific Northwest National Laboratory, Richland, WA 99354, USA*

⁶*Department of Physics, Case Western Reserve University, Cleveland, OH 44106, USA*

⁷*Laboratoire de Physique Nucléaire et de Hautes Énergies, Sorbonne Université, Université Paris Cité, CNRS/IN2P3, 75005 Paris, France*

⁸*Wright Laboratory and Department of Physics, Yale University, New Haven, CT 06520, USA*

⁹*Lawrence Livermore National Laboratory, Livermore, CA 94550, USA*

¹⁰*Center for Exploration of Energy and Matter and Department of Physics, Indiana University, Bloomington, IN, 47405, USA*

¹¹*Institute of Astroparticle Physics, Karlsruhe Institute of Technology, 76021 Karlsruhe, Germany*

¹²*Center for Astrophysics | Harvard & Smithsonian, Cambridge, MA 02138, USA*

(Dated: March 22, 2023)

Project 8 has developed a novel technique, Cyclotron Radiation Emission Spectroscopy (CRES), for direct neutrino mass measurements. A CRES-based experiment on the beta spectrum of tritium has been carried out in a small-volume apparatus. We provide a detailed account of the experiment, focusing on systematic effects and analysis techniques. In a Bayesian (frequentist) analysis, we measure the tritium endpoint as 18553^{+18}_{-19} (18548^{+19}_{-19}) eV and set upper limits of 155 (152) eV (90% C.L.) on the neutrino mass. No background events are observed beyond the endpoint in 82 days of running. We also demonstrate an energy resolution of 1.66 ± 0.19 eV in a resolution-optimized magnetic trap configuration by measuring $^{83\text{m}}\text{Kr}$ 17.8-keV internal-conversion electrons. These measurements establish CRES as a low-background, high-resolution technique with the potential to advance neutrino mass sensitivity.

CONTENTS

I. Introduction

2

II. Apparatus

3

A. Electron trap

4

B. Gas system

5

C. Radio-frequency system

5

III. CRES data features

6

A. Characteristics of electron events

6

B. Data set features

7

C. Scattering

8

D. Mean track duration τ

9

IV. Analysis of CRES data

10

A. Overview

10

B. CRES energy spectrum model

10

1. Instrumental resolution \mathcal{I}

10

2. Energy loss spectra $\mathcal{L}_{\text{tot}}^{*j}$

10

3. Scatter peak amplitudes \mathcal{A}_j

12

V. Simulated CRES data

13

A. Simulation basics and validation

13

^a Present Address: Department of Physics, Sharif University of Technology, P.O. Box 11155-9161, Tehran, Iran

^b Present Address: Center for Experimental Nuclear Physics and Astrophysics and Department of Physics, University of Washington, Seattle, WA 98195, USA

^c claesc@uw.edu

^d Present Address: LeoLabs, Menlo Park, CA 94025, USA

^e Present Address: Ozen Engineering, Sunnyvale, CA 94085, USA

^f Present Address: Thomas Jefferson National Accelerator Facility, Newport News, VA 23606, USA

^g Present Address: Booz Allen Hamilton, San Antonio, Texas, 78226, USA

^h Present Address: Waymo, Mountain View, CA 94043

ⁱ talia.weiss@yale.edu

^j Present Address: Department of Astrophysics/IMAPP, Radboud University, PO Box 9010, 6500 GL Nijmegen, The Netherlands

B. Simulated instrumental resolution	15
VI. Calibration with $^{83\text{m}}\text{Kr}$	15
A. Test of the frequency-energy relation	15
B. $^{83\text{m}}\text{Kr}$ fit procedure with CRES spectrum model	16
C. Instrumental resolution \mathcal{I}	17
1. SNR scaling optimization	17
2. Uncertainties on \mathcal{I} propagated to $^{83\text{m}}\text{Kr}$ fit results	17
D. Field-shifted $^{83\text{m}}\text{Kr}$ data analysis	18
1. Detection efficiency measurement	18
2. Extraction of statistical trap weights	18
E. $^{83\text{m}}\text{Kr}$ shallow-trap data and fits	19
F. $^{83\text{m}}\text{Kr}$ pre-tritium and post-tritium quad trap data and fits	19
1. Uncertainties on $^{83\text{m}}\text{Kr}$ quad trap fit results	20
2. Validating $^{83\text{m}}\text{Kr}$ scatter peak amplitudes with simulation	20
VII. Tritium model	21
A. An analytic model for tritium data analysis	21
B. Tritium beta decay model	21
C. Tritium energy response function model	22
D. Binned event rate model	24
VIII. Tritium parameter estimates and uncertainties	24
A. Mean magnetic field B	24
B. Energy resolution σ	25
C. Scatter peak amplitudes $A_j(p, q)$	25
D. Energy-dependent efficiency ϵ	27
1. Efficiency correction for energy dependence	27
2. Extraction of the SNR dependence on frequency	28
3. Efficiency correction for slope variation	29
4. Efficiency binning	30
E. Frequency dependence of energy response function \mathcal{R}_{PSF}	30
F. Summary of parameter probability distributions	31
IX. Tritium data analysis	31
A. Tritium analysis procedures	31
1. Bayesian analysis procedure	31
2. Frequentist analysis procedure	32
3. Frequency variation of scatter peak amplitudes	33
B. Monte Carlo studies	33
1. Generation of pseudo data	33
2. Coverage and bias tests	34
X. Results and conclusions	35
A. Final results for tritium endpoint and neutrino mass limit	35
B. Background limit	36
C. Neutrino mass sensitivity	36
D. Considerations for future designs	37

Acknowledgments 38

References 39

I. INTRODUCTION

The neutrino comes in three flavors—electron, muon, and tau—associated with the charged leptons. Super-Kamiokande [1] and the Sudbury Neutrino Observatory [2] showed that these flavors mix and oscillate, explaining the anomalies in atmospheric and solar neutrino fluxes. Oscillation between the neutrino flavors requires that neutrinos have mass, in contradiction with the Standard Model of particle physics wherein neutrinos are massless. It is now clear that neutrino mass eigenstates $m_{i=1,2,3}$ exist, of which at least two have non-zero mass. The flavor eigenstates are linear combinations of m_i , with amplitudes given by the elements of a 3×3 unitary mixing matrix U , the PMNS matrix [3, 4].

Oscillation experiments can determine only the differences of the squares $m_i^2 - m_j^2$, not the mass scale, but they constrain the sum of the three neutrino masses, Σm_i , to be at least 0.05 eV [5] because masses are positive definite. It is known from solar neutrino oscillations [2] that $m_2 > m_1$, but whether m_3 is the lightest mass eigenstate (“inverted ordering”) or the heaviest (“normal ordering”) is presently unknown. The neutrino constitutes the first and, so far, the only identified dark matter in the cosmos. Limits on Σm_i have been obtained from observations of the cosmic microwave background and large-scale cosmic structure (see, for example, the Planck collaboration [6] who reported a limit of <0.12 eV within the framework of the Λ CDM model).

The most sensitive technique for a direct and model-independent neutrino mass determination is the tritium beta decay endpoint method [7]. The signal for neutrino mass emerges as a phase-space modification of the spectral shape close to the beta endpoint. This signal is independent of whether neutrinos are Majorana or Dirac particles. Beta spectroscopy measures the electron-weighted neutrino mass,

$$m_\beta = \sqrt{\sum_{i=1}^3 |U_{ei}|^2 m_i^2}. \quad (1)$$

Neutrino oscillation experiments impose an ultimate lower bound of $m_\beta \geq 0.009$ eV ($m_\beta \geq 0.05$ eV) for the case of normal (inverted) mass ordering [5].

Recently, the KATRIN experiment has set a new upper limit of 0.8 eV at 90% confidence level [8]. KATRIN’s design goal is a 0.2-eV mass sensitivity limit [9], if the mass is not larger. KATRIN is expected to either exhaust the quasidegenerate range of neutrino masses that are large compared to either of the mass differences measured in oscillation experiments, or to measure the neutrino mass if it lies in that range.

The neutrino mass might turn out to be smaller than the state-of-the-art experiment KATRIN can discover. While there may be ways to extend the reach of KATRIN somewhat [10], this type of experiment approaches a fundamental limit as a result of its sheer size and use of molecular tritium (T_2). With T_2 , one relies on a theoretical prediction of the spectrum of excited states produced in beta decay, which broadens the spectral response. The neutrino mass effect is spread over a range of slightly differing endpoints for the excitations [11, 12], exacting both a statistical and a systematic price. A direct measurement of this spectrum of excited states is not possible, although specific tests can be performed [13] and are in excellent agreement with theory at the percent level. To advance significantly beyond KATRIN’s design sensitivity—which is the goal of a next-generation tritium endpoint experiment—requires a different approach. An experiment that sets a neutrino mass limit of $m_\beta < 0.04$ eV reaches the full range of neutrino masses allowed under the assumption of an inverted ordering of neutrino mass eigenvalues and would either measure neutrino mass or exclude the inverted ordering [14, 15].

The Project 8 Collaboration has devised a new method called Cyclotron Radiation Emission Spectroscopy (CRES) [14, 16] to reach this goal. In CRES, the emitted beta electron’s energy is measured by detecting its cyclotron radiation as it spirals in a magnetic field. In special relativity, the cyclotron frequency f_c in a magnetic field B is related to kinetic energy E_{kin} as follows:

$$f_c = \frac{1}{2\pi} \frac{eB}{m_e + E_{\text{kin}}/c^2}, \quad (2)$$

where e is the magnitude of the electron charge, m_e is the mass of the electron, and c is the speed of light in vacuum. Project 8 aims to combine CRES with the use of atomic tritium as the beta decay source, to remove uncertainty from molecular states.

CRES was first demonstrated with a precision measurement of the energies of single electrons from $^{83\text{m}}\text{Kr}$ decay by the Project 8 collaboration in 2014 [17] (Phase I). Subsequently, Project 8 has performed a CRES-based tritium experiment (Phase II), which is the subject of this paper. We report details of the tritium endpoint and neutrino mass results from the small-scale Phase II apparatus. These are the first measurements of the continuous tritium spectrum using CRES and the first quantitative exploration of the systematic effects in CRES. A companion Letter [18] provides a high-level overview of Project 8’s Phase II results.

This paper is organized as follows. In Sec. II, the apparatus and data-taking conditions are described in sufficient detail to give context to the analysis. A more comprehensive paper on the apparatus is in preparation. Section III describes the general features of CRES data and the data sets to be analyzed, Sec. IV provides an overview of the analysis approach, including a general CRES signal model. Section V and Sec. VI describe sim-

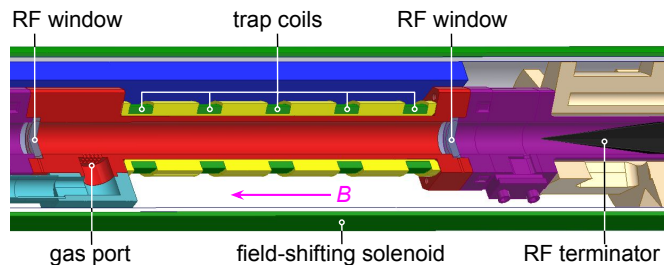


FIG. 1. Cutaway of the cryogenic CRES cell, where electrons are produced in radioactive decay and magnetically trapped. Cyclotron radiation travels axially up the waveguide (left in rotated view), toward the amplifiers and readout electronics.

ulations and calibration measurements with $^{83\text{m}}\text{Kr}$, both of which provide inputs to tritium data analysis. $^{83\text{m}}\text{Kr}$ data are also used to validate the frequency-energy relation in Eq. 2 and to demonstrate the high-resolution capabilities of CRES. The tritium model for data analysis is developed in Sec. VII. This model is an analytic version of the general CRES signal model. Parameter inputs and systematic uncertainties for the tritium analysis are described in Sec. VIII. Section IX describes procedures for analyzing tritium data using both Bayesian and frequentist approaches. In Sec. X, we present endpoint and neutrino mass results. In addition, a search for events above the endpoint produces a stringent limit on the background rate. The sensitivity of this Phase II experiment to the neutrino mass is compared to an analytic prediction.

II. APPARATUS

In the Project 8 Phase II apparatus, molecular tritium or $^{83\text{m}}\text{Kr}$ is confined in a cryogenic gas cell (the “CRES cell”) within the field of a commercial warm-bore superconducting magnet. The cell, mechanically supported on an experimental insert, is positioned in the vertical magnetic field of 0.959 T, which induces cyclotron motion and confines electrons radially. The CRES cell is shown in Fig. 1. Electrons emitted in radioactive decay are trapped axially in dips in the magnetic field created by coils wound around the gas cell. The trap geometry affects resolution, event rate, and event characteristics. For Phase II, electrons are trapped in multiple short traps where the electrons’ axial motion is near-harmonic, rather than in a single longer trap—both because of non-uniformity in the background field, and because of a Doppler shift, as explained below. The currents can be varied independently in the five coils to create traps of varying geometries. Cyclotron radiation emitted by the electrons then propagates through a waveguide, is amplified in two low-noise cryogenic amplifiers in series, and passes on to the room-temperature elements of the detection chain.

The 1.6-m insert which supports the CRES cell is

cooled by a Cryomech AL-60 Gifford-McMahon cryocooler. The cell temperature is controlled by a heater on a PID loop. The dominant noise source in the experiment is thermal, set by the temperature of a custom-made radio-frequency (RF)-absorbing terminator at the lower end of the cell. To reduce noise, the cell is kept as cold as possible. A lower limit on the cell temperature of 85 K is set by the requirement that a sufficient density of $^{83\text{m}}\text{Kr}$ remains in the gas phase.

The Phase-II apparatus was previously described in [14]. Further details on the apparatus and tests thereof will be reported in a paper in preparation [19].

A. Electron trap

The criterion for trapping a charged particle in a magnetic trap is

$$\theta_0 \geq \sin^{-1} \left(\sqrt{\frac{B_0}{B_{\text{max}}}} \right), \quad (3)$$

where θ_0 is the pitch angle at the lowest-field point, where the field is B_0 , and B_{max} is the smaller of the maximum field values on either side of B_0 . Pitch angle is defined as the angle between the electron's momentum and the local field direction.

The cyclotron radiation produced by electrons propagates along the waveguide axis toward the detection system. Because the trapped electrons undergo axial motion, their cyclotron radiation is Doppler-shifted at twice the axial frequency. The maximum Doppler shift is proportional to the electron's axial velocity as it passes through the trap minimum. The resulting frequency modulation creates sidebands to the mean cyclotron frequency (termed the 'carrier'). The modulation index h is defined as the ratio of the peak shift in carrier frequency to the modulation (here, axial) frequency. For large h , sidebands proliferate and the carrier becomes too weak to be detected [20]. Our noise threshold for detecting the carrier corresponds approximately to $h \leq 1$. In magnetic traps this condition translates directly to a pitch-angle limitation, and, equivalently, a limitation on the axial amplitude, which dictates short traps. To increase statistics, several short traps are spaced along the cell within the most uniform region of the background field.

Data were taken in two trap configurations. A deep 'quad' trap with the magnetic field shown in Fig. 2(a) was used to maximize the number of trapped electrons and to increase effective volume in this small apparatus. Four of the trap coils shown in Fig. 1 were used; the fifth was not used because the background field varies too steeply there to form a trap. The 0.959-T background field is also shown in Fig. 2. It deviates from homogeneity at the 5×10^{-4} level because of a non-functional trim coil of the superconducting magnet, which causes the slope and curvature seen in the figure. A shallow double trap was used to demonstrate the high resolution capability

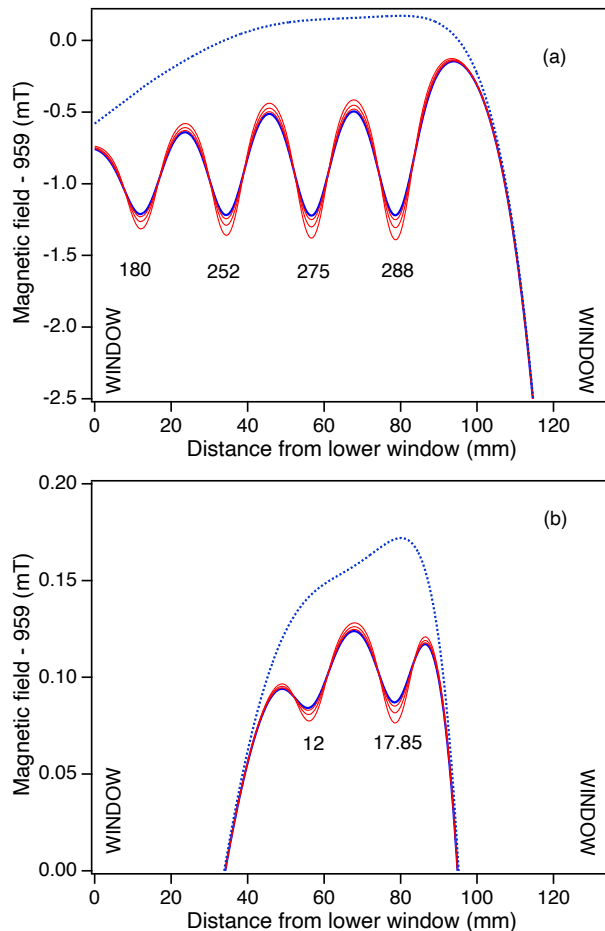


FIG. 2. (a) Calculated quad trap coil field. (b) Calculated shallow trap coil field. Note different scales on y -axes. The background field from NMR measurements is shown as a blue dotted line. The solid blue lines are for a radius 1 mm from the axis, and the red lines are for 2, 3, and 4 mm in turn. The coil currents are shown in mA under each trap. Trap depths were equalized for the 1-mm radius because the coupling to the waveguide's TE_{11} mode maximizes on the axis.

of the CRES technique; this trap is shown in Fig. 2(b). Parameters for the traps are listed in Tab. I.

Table I also gives the volumes and minimum detectable pitch angles $\theta_0(h = 1)$ at the trap centers. The effective volume of each trap V_{eff} is calculated numerically with the aid of Eq. 3 for a maximum axial amplitude equivalent to a modulation index $h = 1$ and a radius of 5.02 mm, the waveguide radius. Other sources of inefficiency, such as track and event reconstruction, are not included in V_{eff} . Also shown is the minimum pitch angle $\theta_0(\text{min})$ in each trap. In the table, z_{min} is the location of the trap minimum relative to the lower CRES cell window. Estimates of B_0 are also included in the table; calibrations with $^{83\text{m}}\text{Kr}$ produced more precise field estimates, as discussed in Sec. VIF and Sec. VIII A.

The total V_{eff} for the quad trap is about 10 times that of the shallow trap, but experimental measurements with

TABLE I. Calculated quad and shallow trap configurations.

	Coil 1	Coil 2	Coil 3	Coil 4	Unit
Turns	64	63	64	65	
Quad trap coil parameters.					
Current	180	252	275	288	mA
z_{\min}	11.9	34.4	56.7	78.6	mm
$B_0 - 959$	-1.21173	-1.21768	-1.22141	-1.21918	mT
Trap depth	0.45423	0.57720	0.70887	0.72418	mT
$\theta_0(h = 1)$	89.47	89.37	89.33	89.30	deg
$\theta_0(\min)$	88.75	88.59	88.44	88.42	deg
V_{eff}	3.0	3.6	3.9	4.1	mm ³
Shallow trap coil parameters.					
Current			12	17.85	mA
z_{\min}			55.6	78.4	mm
$B_0 - 959$			0.084724	0.087937	mT
Trap depth			0.009905	0.036838	mT
$\theta_0(h = 1)$			89.89	89.84	deg
$\theta_0(\min)$			89.82	89.64	deg
V_{eff}			0.61	0.96	mm ³

$^{83\text{m}}\text{Kr}$ give a value closer to 40 for this ratio. This discrepancy is seen in part because the deep quad trap holds more ‘invisible’ electrons with relatively small pitch angles between $\theta_0(h = 1)$ and $\theta_0(\min)$, which can scatter into the detectable pitch-angle range. In the quad trap, the first observed electron track is unscattered in approximately 50% of events (Sec. VIF), while in the shallow trap, the fraction is approximately 70% (Sec. VIE and Fig. 4). There are also small corrections for the difference in radiated electron power in the shallow and quad traps, because the frequencies are not exactly the same and only two trap coils are in common. The coupling of an electron to the waveguide depends on the trap. The main source of the discrepancy, however, is attributable to the numerical calculation of V_{eff} for very weak traps. There are inhomogeneities in the background magnetic field which are not well characterized and not included in these calculations. It is likely that these features become important when the trap is weak. Evidence for this emerged when still shallower traps were explored and the coil-3 trap disappeared below 10 mA. This last effect is not significant for the deep quad trap.

A long additional copper coil called the “field-shifting solenoid” (FSS) was inserted into the superconducting solenoid’s warm bore that encompasses the CRES cell (Fig. 1). The FSS was used to homogeneously shift the magnetic field for studies of detection efficiency as a function of frequency, which are described in Sec. VID 1. By running current through this additional coil the field was shifted in steps of $\Delta B_{\text{FSS}} = 0.07$ mT over a range of ± 3 mT.

A single-axis fluxgate magnetometer (Schonsted Instrument Co. DM2220) was used during the final $^{83\text{m}}\text{Kr}$ calibration phase to assess the role of environmental magnetic field changes in the laboratory. Over a 3-day period, peak-to-peak variations of 6% in the 0.11-mT vertical laboratory background field were observed at a distance

of 3 m from the magnet. These variations correspond to a 0.3 eV difference in reconstructed electron energies. The variation within the magnet bore is expected to have been even lower due to the self-shielding provided by a superconducting magnet in persistent mode. While the fluxgate magnetometer was not available during tritium running, the influence of environmental field variations is considered negligible at the relevant sensitivity level.

B. Gas system

The radioactive gases were released into the apparatus from a custom gas manifold. This manifold connected to the CRES cell via a delivery line running along the insert and through a grid of holes with diameter less than 0.1 wavelengths of the microwave radiation. The gas system could be run in two modes. In neutrino mass data acquisition mode, molecular tritium gas was delivered, while in calibration mode, $^{83\text{m}}\text{Kr}$ gas was delivered. Tritium was stored in a 0.5-g non-evaporable getter (SAES ST 172/HI/7.5-7/150 C), the temperature of which was controlled by an ion gauge to maintain the desired operating pressure, usually $1.6\text{--}2.6 \times 10^{-6}$ mbar (calibrated for H_2). Pressure could be maintained to $\pm 3\%$ run-to-run for the duration of data-taking. In later data sets, we prevented accumulation of ^3He (produced in tritium decay) by extracting gas continually through a leak valve to a getter-ion pump, which also lowered the concentration of traces of methane, Ar, CO and CO_2 impurities; this is referred to as the “pumped” configuration. The initial 2-Ci inventory of tritium was sufficient for a ~ 100 -d data-taking period. Gas composition could be monitored by two residual gas analyzers, an SRS-100 close to the SAES getter, and an Extorr XT100 at the getter-ion pump manifold.

For calibration studies, the $^{83\text{m}}\text{Kr}$ gas emanated from ^{83}Rb (6 mCi on July 19, 2019), adsorbed on zeolite [21]. The Kr was mixed with H_2 to tune the mean time between electron-gas collisions to match that in tritium data. The H_2 was stored in a separate getter and pressure-controlled in the same way as the tritium.

C. Radio-frequency system

The CRES cell forms the first section of the waveguide through which cyclotron radiation travels toward the amplifiers (Low Noise Factory LNF-LNC22.40WA). For the Phase II decay cell used in this work, a circular waveguide was chosen over the rectangular WR-42 used previously [17], to increase the volume and to accept circular polarization. In the frequency range 25.8 to 27.0 GHz, waveguide of radius 5.02 mm supports two propagating modes, TE_{11} and TM_{01} . The electron couples well to the TE_{11} mode and only weakly to the TM_{01} mode (Fig. 3). The coupling is maximal on-axis and falls off to a small value near the wall.

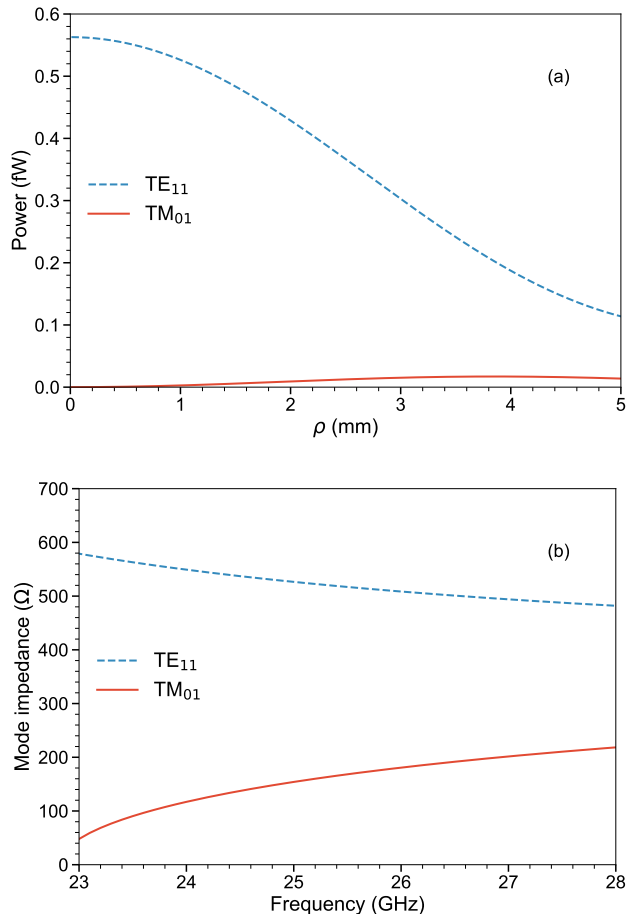


FIG. 3. (a) Coupling of the electron to the two propagating modes as a function of the distance ρ from the axis. The electron has energy 18.6 keV ($f_c \approx 25.9$ GHz) and pitch angle 90° . (b) Mode impedance for the two propagating modes.

The cyclotron radiation emitted by a trapped electron propagates both downward and upward, passing through RF-transparent CaF₂ windows (United Crystals Inc.) that confine the radioactive gas (Fig. 1). This crystalline material has a coefficient of thermal expansion that matches copper at low temperatures, and is known to have low permeability to tritium [22]. To minimize interference from reflections, the downward-propagating radiation is absorbed in a custom-made cryogenic RF terminator. Beyond the uppermost window, the upward-propagating circularly polarized radiation is converted to linear polarization by a quarter-wave ‘plate.’ The radiation is then transmitted via a WR-42 single-mode rectangular waveguide, including a gold-coated stainless steel section for thermal insulation, to cryogenic amplifiers held at 30 K. Residual reflections from the windows, joints, and transitions create weak resonant cavity modes within the gas cell, which enhance spontaneous emission at particular frequencies and locations within the trap. These resonances significantly modify the response

to signals from electrons as a function of trap position and frequency, presenting a difficult analysis challenge. For example, the quarter-wave plate’s reflection of the TM₀₁ mode creates a sharp cavity-like absorption resonance that, despite the weak coupling to the electron, can clearly be seen in the efficiency function at 25.925 GHz, as described in Sec. VIII D 3.

After cryogenic and room-temperature amplification, room-temperature RF electronics downmix the signal by 24.5 GHz. The downshifted signal is digitized by a ROACH2 DAQ system [23] at 3.2 gigasamples per second, with an FPGA performing digital downconversion to 200 megasamples per second and Fast Fourier Transforms (FFT) for three separate frequency windows with independently-set center frequencies. When two 40.96- μ s bins within any 0.5-ms window exceed a signal-to-noise ratio (SNR) threshold, a compute node writes time-series data to disk. SNR is used instead of absolute power in all stages of data analysis (triggering, event reconstruction, spectrum analysis) to avoid the effects of gain variation of the amplifiers and filters.

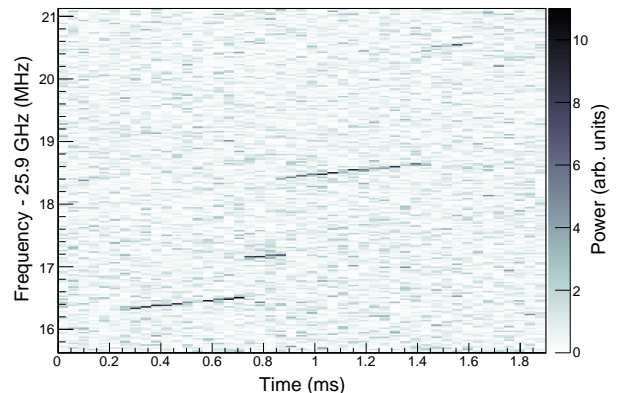


FIG. 4. Spectrogram of chirped electron signals of a single radiating electron. The bin size is 25 kHz by 40.96 μ s.

III. CRES DATA FEATURES

A. Characteristics of electron events

Electron events may be displayed in a spectrogram (or ‘waterfall plot’) of frequency vs. time, with pixels indicating signal power by color or intensity. Figure 4 shows a typical event composed of ‘tracks,’ with the jumps in frequency from track to track caused by collisions with gas molecules. Events are continuous in time but discontinuous in frequency. The frequency changes after a collision are due to changes in both energy and pitch angle. Pitch-angle changes cause the amplitude of the electron’s axial motion to increase or decrease, so the average magnetic field experienced by the electron may increase or decrease. Between collisions, signals continuously chirp upward in frequency as the electrons radiate energy [20].

TABLE II. Characteristics of key data sets. N_{events} is the number of reconstructed events in a given data set. $N_{\text{tracks}}^{\text{true}}$ is the estimated mean number of electron tracks per event (including unreconstructed tracks). τ is the mean time between electron-gas collisions.

Data Set	Purpose	Magnetic field configuration	Gas system configuration	N_{events}	$N_{\text{tracks}}^{\text{true}}$	τ (ms)	Section(s)
$^{83\text{m}}\text{Kr}$ shallow	Demonstrate best resolution and probe detector response	Shallow double trap	Not pumped	6831	1.24 ± 0.12	0.342 ± 0.005	Sec. VIA, Sec. VIE
$^{83\text{m}}\text{Kr}$ field-shifted	Measure frequency dependence of efficiency and other characteristics	Deep quad trap & deep single traps; background B field varied	Not pumped	9350	2.73 ± 0.24	0.173 ± 0.003	Sec. VID
$^{83\text{m}}\text{Kr}$ pre-tritium	Calibrate magnetic field, scattering environment	Deep quad trap	Not pumped	87634	2.40 ± 0.27	0.162 ± 0.001	Sec. VIF
Tritium	Spectroscopy of tritium endpoint	Deep quad trap	Pumped	3770	2.36 ± 0.34	0.146 ± 0.003	Sec. VII, Sec. IX
$^{83\text{m}}\text{Kr}$ post-tritium	Calibrate magnetic field, scattering environment	Deep quad trap	Pumped	47426	3.37 ± 0.21	0.188 ± 0.001	Sec. VIF

We use a point-clustering algorithm to identify high-SNR bins occurring close together in time and frequency as belonging to the same electron track [24, 25]. A reconstruction algorithm extracts the starting frequency of the first track of each event, identifying it as the “start frequency” of the event.

One of CRES’s promising features is its immunity to background. Few processes can masquerade as valid signals, which have specific signatures in frequency, duration, power, time dependence, and event structure. The interactions of cosmic rays and energetic beta and gamma backgrounds with the gas can in principle lead to the production and trapping of an electron in the right energy range, but this is a rare occurrence because of the low density of the gas. The dominant background is expected to be from RF noise fluctuations. In this analysis, we distinguish electron events from RF noise by a cut on a function of three characteristics: the number of tracks in a candidate event, the duration of the first track, and the SNR of the first track. These characteristics are distributed differently for electron events and RF noise fluctuations. We set the threshold for this cut before tritium data acquisition at a level expected to allow less than one RF-noise-induced background event beyond the endpoint per 100 days of run time per RF channel at 90% confidence level.

Even with the successful elimination of false tracks, the first track *visible* in an event is not necessarily the first track following beta decay or internal conversion. Tracks can be too short or too low in power to be detected. The response function that has been developed takes account of both of these possibilities, and includes also the effects of cyclotron radiation losses and the broadening associated with pitch-angle variations.

B. Data set features

We took data using two kinds of radioactive source, $^{83\text{m}}\text{Kr}$ and tritium. Studies of the efficiency, energy response, and magnetic field were carried out with $^{83\text{m}}\text{Kr}$ during the second half of 2019. Tritium data taking began in mid-December and extended into March 2020, with several weeks of downtime in February for laboratory maintenance. A final week of $^{83\text{m}}\text{Kr}$ measurements concluded the data-taking campaign in March as planned, just before a global pandemic precluded further data-taking and laboratory work.

Properties of key data sets are summarized in Tab. II in chronological order. Details of electron trap configurations are discussed in Sec. IIA and of gas system configurations in Sec. IIB. The mean number of electron tracks per event, $N_{\text{tracks}}^{\text{true}}$, is determined from the post-reconstruction tracks per event in data combined with simulation studies of the relationship between true and reconstructed tracks per event. Section VIIC describes how $N_{\text{tracks}}^{\text{true}}$ is used in the tritium data analysis. Section IIID describes how τ , the mean time between electron-gas collisions, is extracted from the data and used in the tritium analysis. For all data sets that provide direct calibration input to the tritium analysis— $^{83\text{m}}\text{Kr}$ field-shifted, $^{83\text{m}}\text{Kr}$ pre-tritium, tritium, and $^{83\text{m}}\text{Kr}$ post-tritium—the gas composition and scattering rate of electrons from gas molecules were kept as similar and stable as possible, despite the absence of krypton and the presence of helium in the gas system during tritium data-taking.

$^{83\text{m}}\text{Kr}$ data were acquired in periods lasting a few hours each for deep quad trap data sets. Shallow-trap data sets took several days to acquire adequate statistics. With

Data set	Tritium	$^{83\text{m}}\text{Kr}$ shallow	$^{83\text{m}}\text{Kr}$ field-shifted	$^{83\text{m}}\text{Kr}$ pre-tritium	$^{83\text{m}}\text{Kr}$ post-tritium
Hydrogen isotopes	91±5	9-98	38-98	23-91	41-99
Helium-3	8±4	0-99	0-59	0-67	0-58
Argon		<1	<1	5-10	<1
Krypton		1-3	2-3	2-5	<1
Carbon monoxide	1±1				<1

TABLE III. Possible ranges of percentages of inelastic scatters due to each of the main gas species present during the tritium data set and the primary $^{83\text{m}}\text{Kr}$ data sets. Scattering from all non-listed gases for a given data set is negligible. Values are given as ranges with near-uniform probability (with sigmoid edges) for $^{83\text{m}}\text{Kr}$ data, where deuterium contamination interfered with distinguishing ^3He from hydrogen isotopes.

maximum event durations of <10 ms and rates of ~ 1 cps (counts per second), pileup effects were negligible. A single 100-MHz-bandwidth DAQ channel was used to acquire data on the 17.8-keV K internal-conversion line, and sometimes the second channel or both the second and third channels simultaneously took data on the L lines or the M and N lines.

We took tritium data over 82 days in the deep quad trap configuration, with a mean event rate of 0.5×10^{-3} cps. The analysis window spanned 25.81–25.99 GHz, or 16.2–19.8 keV in electron energy. The three DAQ windows were overlapped to minimize efficiency variation with frequency due to windowing, with only the highest-efficiency channel analyzed in the overlap regions [26].

C. Scattering

To account for the effects of missed tracks described in Sec. III A, it is necessary to understand the spectrum of an electron’s possible energy losses between the start times of successive tracks. The dominant contributor to energy losses between successive tracks is the electron’s inelastic scattering with gas molecules; this is affected by which gas species are present in the gas cell. Here we describe our measurements and analysis of the gas composition; in Sec. IV B 2, we describe where this information comes into the broader analysis.

Inelastic scatters produce pitch angle changes of $\sim 0.1^\circ$ [27]—generally small enough that the electron remains trapped after scattering. By contrast, elastic scattering tends to produce $\geq 5^\circ$ changes [27], ejecting the electron from the trap and terminating the event. In addition, elastic scattering cross sections are an order of magnitude smaller than inelastic cross sections for the most relevant gas species in our data. We therefore neglect elastic scattering as an energy-loss mechanism between tracks.

One input to the inelastic loss spectrum must be measured in-situ: the relative likelihood γ_i of an inelastic collision with gas species i . The γ_i factors for key data sets are derived from quadrupole mass analyzer data as

follows, with

$$\gamma_i = \frac{\sigma_{i,E} C_{\text{temp},i} p_{\text{raw},i} / s_i}{\sum_n (\sigma_{n,E} C_{\text{temp},n} p_{\text{raw},n} / s_n)}, \quad (4)$$

where $\sigma_{i,E}$ is the total inelastic scattering cross section of an electron of energy E with gas i ; $C_{\text{temp},i}$ is a factor accounting for gas freezing to CRES cell walls; $p_{\text{raw},i}$ is the uncorrected partial-pressure reading of the quadrupole mass analyzer; and s_i is the sensitivity factor of the quadrupole mass analyzer to gas species i . The uncertainty on each of these quantities is propagated through to the uncertainty on γ_i in the standard way.

The inelastic scattering cross sections $\sigma_{i,E}$ are derived from literature values; contributions to uncertainties on these account for both uncertainties within and differences between published data sets. Values of $\sigma_{i,E}$ for H_2 and T_2 come from a measurement at 18.6 keV [28] and are scaled according to [29] for 17.8 keV. Cross sections on ^3He , Kr, and Ar are taken from [30], with uncertainties from [31–34]. For CO, the cross section is evaluated using the expression from [35], with uncertainties from [36, 37].

Because Kr is the only relevant gas species for which significant adsorption to cold walls is expected at 85 K, we take $C_{\text{temp},i}=1$ for all other species. The $C_{\text{temp},\text{Kr}}$ value of 0.90 ± 0.05 is measured from temperature-varying $^{83\text{m}}\text{Kr}$ CRES data, taking advantage of the direct dependence of event rate on Kr density in the cell.

We adopt sensitivity factors s_i from quadrupole mass analyzer manuals, with uncertainties estimated from differences between different manufacturers’ values.

We measured the raw partial pressures $p_{\text{raw},i}$ using the quadrupole mass analyzer. Since $^{83\text{m}}\text{Kr}$ data sets were completed in hours or at most a few days, gas conditions were stable. Therefore, each data set’s $p_{\text{raw},i}$ measurements are determined from a single representative quadrupole mass analyzer scan. In contrast, the tritium data were taken over months, with some variation in conditions, especially initially as pumping speed settings were optimized. Gas composition for the tritium data set is therefore an average, the sum of measurements taken in each of the states weighted by the accumulated counts in that state.

One additional complication in interpreting $p_{\text{raw},i}$ values comes from the inability to distinguish species

with identical charge-to-mass ratio with the available quadrupole mass analyzers. This creates a challenge because deuterium gas was used in the initial testing during commissioning of the gas system, and was mistakenly allowed to contaminate the reservoir of H_2 used for $^{83\text{m}}\text{Kr}$ data. For $^{83\text{m}}\text{Kr}$ data sets, therefore, ^3He and HD cannot be distinguished, and this uncertainty is reflected in the larger error bars on gas composition in these data sets. In contrast, the tritium gas supply was not deuterium-contaminated, so the tritium data do not suffer from this uncertainty.

Table III shows the inelastic scattering fraction results, as derived from the quadrupole mass analyzer data and Eq. 4. For fits to the $^{83\text{m}}\text{Kr}$ pre-tritium and post-tritium data sets, to propagate uncertainties, we sample γ_i from near-uniform distributions defined according to the ranges in this table, requiring that the sampled fractions sum to 1. This near-uniform shape, flat with sigmoid ends, reflects the inability to distinguish ^3He from HD in $^{83\text{m}}\text{Kr}$ data. Section VIF 1 more fully describes uncertainty propagation in $^{83\text{m}}\text{Kr}$ quad trap fits.

In tritium and $^{83\text{m}}\text{Kr}$ data, scattering from molecular hydrogen isotopes is dominant. In both data types, ^3He produced by decay of residual tritium adsorbed to the walls of the gas system is the next-largest contributor to scattering. Tritium data include a small contribution from a mass-28 gas species, likely CO . In addition to the krypton present in $^{83\text{m}}\text{Kr}$ data sets, argon is also present in the data sets taken before the pumped gas system configuration (Sec. II B) enabled lower impurity levels.

D. Mean track duration τ

Track duration is the time between successive scatters of an electron with gas molecules. In the track reconstruction process, track duration is a powerful tool for discriminating between noise and signal. The offline event reconstruction [25] removes events of which the first track's signal-to-noise ratio is below certain thresholds. These thresholds are specific to the combination of first track duration and number of tracks in the event. Hence, the gas pressure in the CRES cell impacts the overall event detection efficiency as well as the first track detection efficiency, thereby affecting the electron energy point-spread function \mathcal{R}_{PSF} (see Sec. IV B). Track duration also impacts the reconstructed mean number of tracks per event, which in turn affects the shape of the tail from missed tracks in \mathcal{R}_{PSF} , as discussed in Sec. VIII C. It was thus necessary to assess the track duration distribution for each data set.

Since track duration is determined by random scattering, which is a Poisson process, the underlying probability density function (PDF) is exponential. However, short tracks are less efficiently detected, so the number N of tracks detected with a certain duration t is given by

$$N(t) \propto P_d(t)e^{-t/\tau}, \quad (5)$$

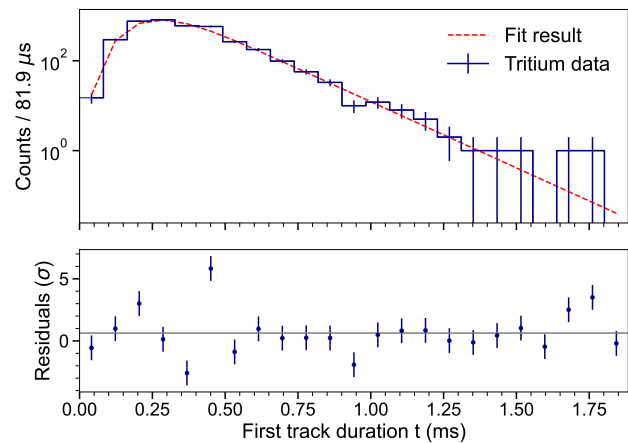


FIG. 5. Tritium data track duration fit using Eq. 5 and Eq. 6. The track reconstruction algorithm [25] favors track lengths equal to a multiple of 3 times the spectrogram (Fig. 4) time bin width ($40.96 \mu\text{s}$). This leads to larger residuals for some track lengths.

where τ is mean time between collisions with gas molecules and $P_d(t)$ is the relative probability of detection as a function of τ .

To fit the full track duration distribution and extract τ , it is necessary to have a model for $P_d(t)$ that accounts for the roll-off in detection efficiency at short track durations. We used the following empirical model, which provides good fits to the data is

$$P_d(t) = \text{erfc} \left(\psi - \sqrt{\frac{\zeta}{t}} \right), \quad (6)$$

where erfc is the complementary error function and ψ and ζ are determined solely by conditions held constant for all data sets (except the field-shifted data), such as SNR and the event-reconstruction algorithm's success rate at reconstructing short-duration tracks.

To extract τ in the core tritium and $^{83\text{m}}\text{Kr}$ calibration data sets, we first determined ψ and ζ independently by analyzing reconstructed first-track-duration distributions of $^{83\text{m}}\text{Kr}$ data sets at five different pressures, and therefore five values of mean track duration. We used the Stan software package [38] to do a Markov chain Monte Carlo (MCMC) Bayesian analysis in which ψ and ζ were shared for all data sets and τ was allowed to vary between data sets, with weakly informative priors. The best-fit values and uncertainties for ψ and ζ were determined from the resulting posterior distributions.

The resulting information about ψ and ζ is used in the track-duration distribution fits, in which we extract τ for the core tritium and $^{83\text{m}}\text{Kr}$ calibration data sets using negative log-likelihood minimization. The fit result for the tritium data set is shown in Fig. 5 and the extracted mean track durations for all data sets are listed in Tab. II.

These τ values are inputted to the instrumental resolution simulations (Sec. VIC).

IV. ANALYSIS OF CRES DATA

A. Overview

The primary content of this paper is the analysis strategy we developed for CRES data and the results we obtained using it. The analysis is complex, a consequence of the exploratory nature of the experiment. Some aspects of the experiment design and the analysis were not anticipated; for example, the gas composition measurement was more important than we had expected, but it would not be as significant in future designs with higher resolution and purer source gas. Another unexpected complication was the extent to which the efficiency as a function of frequency and energy was modulated by the presence of parasitic reflections in the waveguide, which demanded a very detailed analysis methodology. A flow chart for the analysis is given in Fig. 6. Notwithstanding the complications both expected and unexpected, we have achieved a complete and successful analysis, as reported below.

B. CRES energy spectrum model

We model a generic detected CRES signal spectrum \mathcal{S} as

$$\mathcal{S} = \epsilon(\mathcal{Y} * \mathcal{R}_{\text{PSF}}), \quad (7)$$

$$\mathcal{R}_{\text{PSF}} = \sum_{j=0}^{j_{\text{max}}} \mathcal{A}_j \left(\mathcal{I} * \mathcal{L}_{\text{tot}}^{*j} \right). \quad (8)$$

Here, all variables are functions of E_{kin} , as denoted by script lettering. The symbol $*$ represents convolution and $*^j$ represents self-convolution j times. The efficiency function ϵ encodes the probability to detect electron events and is discussed in-detail in Sec. VIII D. The underlying true energy spectrum of the electrons is \mathcal{Y} . The underlying spectrum is described in Sec. VI B for $^{83\text{m}}\text{Kr}$ and in Sec. VII for tritium. \mathcal{R}_{PSF} is the point-spread function, which represents the energy response for mono-energetic electrons—in other words, how reconstructed energies are shifted and broadened relative to true energies.

Equation 8 shows that the energy point-spread function \mathcal{R}_{PSF} is comprised of a sum of scatter peaks $\mathcal{I} * \mathcal{L}_{\text{tot}}^{*j}$ weighted by amplitudes \mathcal{A}_j , as illustrated in Fig. 7. These amplitudes describe the relative likelihood that an electron will first be detected after j scattering events. We account for the possibility of up to j_{max} scatters before the first detection. We use $j_{\text{max}} = 20$ in both $^{83\text{m}}\text{Kr}$ and tritium fits, as increasing j_{max} further has no observable effect on results, for Phase II conditions. The

instrumental resolution \mathcal{I} accounts for broadening from magnetic field inhomogeneity and noise. The distribution of electrons' energy losses between scatters \mathcal{L}_{tot} depends on the gas composition, the differential cross section on each gas component, and the loss to cyclotron radiation. The elements in \mathcal{R}_{PSF} are described further in the remainder of this section.

1. Instrumental resolution \mathcal{I}

The instrumental resolution \mathcal{I} is the spectrum that a source of mono-energetic electrons would have if they were all detected before scattering. \mathcal{I} is broadened only by noise and by the differences in the range of magnetic fields sampled by electrons with different pitch angles and radial positions. These ranges vary with trapping geometry and are determined by simulation for each experiment configuration, as described in Sec. VI C. The broadening from frequency reconstruction, *e.g.*, due to frequency binning in the Fourier-transformed data and noise, is only ~ 0.2 eV. This is small compared to the effect of magnetic field inhomogeneity and is therefore neglected, for \mathcal{I} . Reconstruction also shifts frequencies upwards by 14 kHz (equivalent to 0.3 eV), on average [25]. This effect is present in all data ($^{83\text{m}}\text{Kr}$ and tritium) and we decrease the reported magnetic field value in Sec. VIII A to account for it.

2. Energy loss spectra $\mathcal{L}_{\text{tot}}^{*j}$

Electrons lose energy primarily by inelastic scattering with gas molecules, causing the jumps in Fig. 4, as discussed in Sec. III C. Cyclotron radiation is a smaller, continuous source of electron energy loss, causing the upward track slopes in Fig. 4. $\mathcal{L}_{\text{tot}}^{*j}$ comprises the distribution of possible energy losses an electron has experienced *before* the first detected track due to inelastic scattering and cyclotron radiation, with the self-convolution j times accounting for j scatters. The electron energy loss spectrum for a single scatter is

$$\mathcal{L}_{\text{tot}} = (\gamma_1 \mathcal{L}_1 + \gamma_2 \mathcal{L}_2 + \dots + \gamma_n \mathcal{L}_n) * \mathcal{L}_r, \quad (9)$$

where \mathcal{L}_i is the electron inelastic energy loss spectrum for the i^{th} gas species, each γ_i is the fraction of inelastic scatters that are due to the specific gas species i , and \mathcal{L}_r is the energy loss spectrum due to cyclotron radiation during the missed track.

We determine bounds on γ_i from quadrupole mass analyzer data as described in Sec. III C. For the shallow trap data, the high resolution allows for a more precise estimate of gas scattering fractions for H_2 and He to be determined from the fit to $^{83\text{m}}\text{Kr}$ data. We neglect the energy dependence of the scatter fractions γ_i over the small range of energy change.

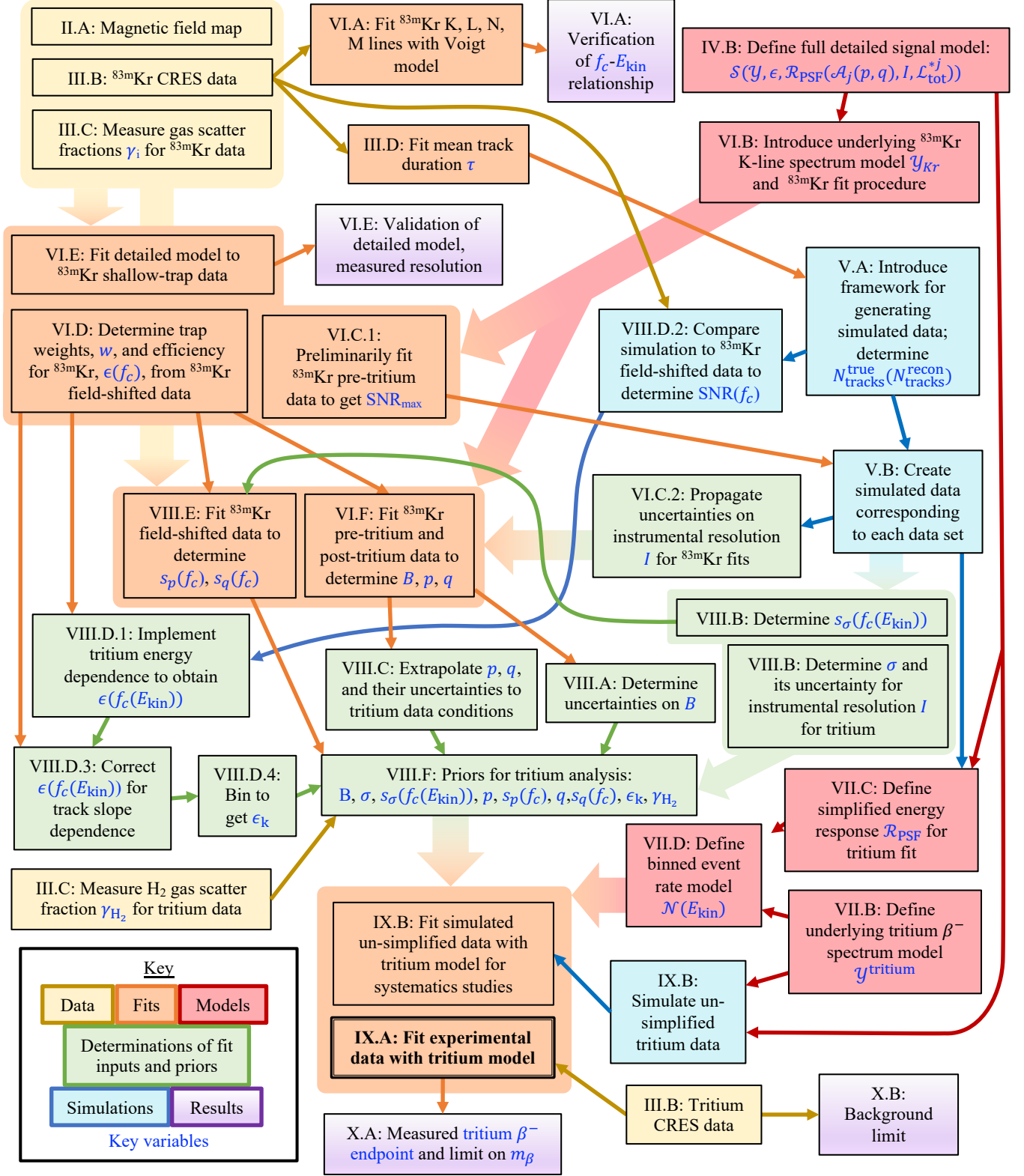


FIG. 6. Flow chart of the analysis procedure. Thin arrows represent relationships between individual boxes, while thick arrows describe shared inputs from and/or outputs to a group of boxes in the same bubble.

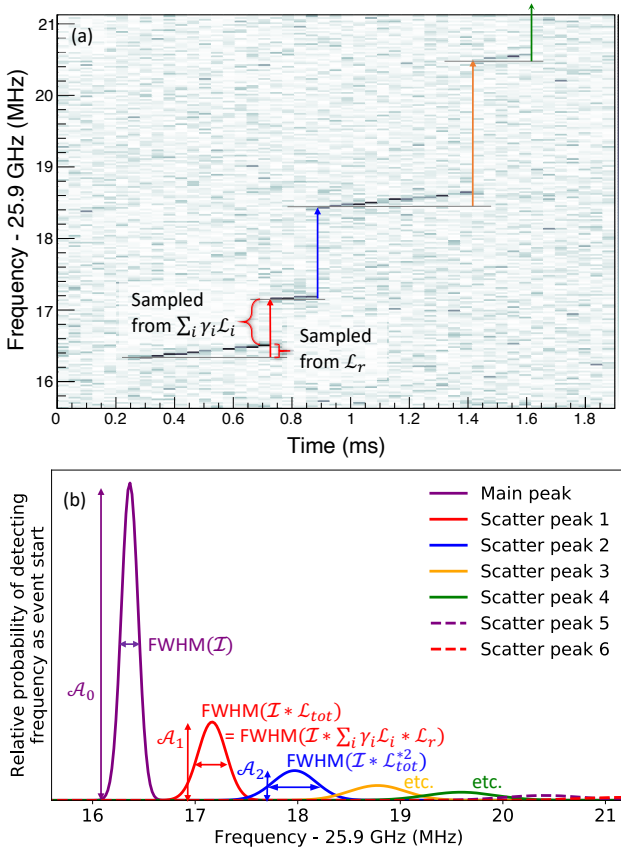


FIG. 7. (a) A CRES event with frequency jumps corresponding to inelastic scattering $\mathcal{L}_{\text{tot}} = \sum_i (\gamma_i \mathcal{L}_i)$ and energy loss due to cyclotron radiation \mathcal{L}_r labelled. (b) A modeled spectrum broken down into its constituent scatter peaks and labelled to show the roles of model parameters: scatter peak amplitudes \mathcal{A}_j , instrumental resolution \mathcal{I} (with 1.66-eV FWHM), and energy loss spectra $\mathcal{L}_{\text{tot}}^j$. Each scatter peak is displayed as a simple Gaussian for illustration purposes.

Each \mathcal{L}_i is calculated in the Bethe theory of electron inelastic scattering (as in [39]), given by

$$\frac{d\sigma}{dE} = \frac{4\pi a_0^2 R}{E_{\text{kin}}} \left[\frac{R}{E} \frac{df}{dE} \ln \left(\frac{4c_E E_{\text{kin}}}{R} \right) + \mathcal{O} \left(\frac{R}{E_{\text{kin}}} \right) \right], \quad (10)$$

where R is the Rydberg energy, a_0 is the Bohr radius, E_{kin} is the incident energy of the electron, E is the energy loss of the electron, $c_E \approx (R/E)^2$, and df/dE is the optical oscillator strength of the gas molecules. The optical oscillator strength [40–42] data for the relevant gas species are from the LXCat database [43–46].

We determine the loss due to cyclotron radiation \mathcal{L}_r using the simulated data described in Sec. V A. In these simulated data, missed tracks associated with detected events are identified. The distribution of differences between track end frequency and track start frequency among these tracks is converted to energy and taken as the radiative energy loss spectrum \mathcal{L}_r (Fig. 8), a function of track duration τ . With most of its weight in a peak between 0 and 3 eV—reflecting the low likelihood

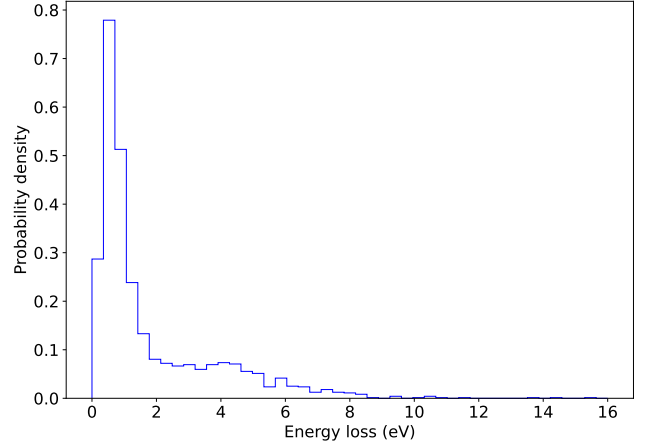


FIG. 8. Simulated \mathcal{L}_r , the energy loss distribution due to cyclotron radiation during a missed track, for conditions (e.g., track duration) corresponding to the $^{83\text{m}}\text{Kr}$ pre-tritium data set.

of missing long tracks—and a modest tail out to ~ 10 eV, \mathcal{L}_r has a much smaller impact than inelastic scatters. \mathcal{L}_r is included in the $^{83\text{m}}\text{Kr}$ fit model and in simulated data (see Sec. V A). However, we omit \mathcal{L}_r from the tritium fit model, since Monte Carlo (MC) pseudo-data studies of the type described in Sec. IX B showed that omitting \mathcal{L}_r has no measurable effect on the tritium analysis.

3. Scatter peak amplitudes \mathcal{A}_j

Each amplitude \mathcal{A}_j is the relative likelihood of missing the first $j - 1$ tracks and detecting the j^{th} track in an event. Because scattering changes the distribution of electron pitch angles, \mathcal{A}_j is not expected to follow a strictly exponential dependence on j . In addition, \mathcal{A}_j depends both on the details of the event reconstruction algorithm—its thresholds in first track duration, first track SNR, and number of tracks in the remainder of an event—and on the distributions of these properties among events in the data. Because the thresholds in the reconstruction algorithm are set empirically to exclude the expected distribution of false events rather than from an *a priori* analytical model, the model for \mathcal{A}_j is also phenomenological. The model used is

$$\mathcal{A}_j = \exp \left[-p j^{(-dp+q)} \right], \quad (11)$$

with free parameters p and q . The constant $d = -0.4955$ is chosen to minimize the correlation between p and q and held fixed. The model is found to provide sufficient flexibility to account for the deviation from exponentiality, as confirmed in simulations shown in Sec. VIF 2.

The dependence of \mathcal{A}_j on the distribution of tracks per event ($N_{\text{tracks}}^{\text{true}}$) is captured in a dependence of p and q on a data set's average $N_{\text{tracks}}^{\text{true}}$ value. The difference in $N_{\text{tracks}}^{\text{true}}$ among data sets stems mainly from differences

in gas composition. Gas species have different relative likelihoods of elastic and inelastic scattering, and elastic scattering is far likelier to cause an electron to undergo a large pitch angle change into a non-detectable pitch angle, ending the visible portion of the event. The p and q values for $^{83\text{m}}\text{Kr}$ data sets are determined from fits to the CRES spectra. The values used for the tritium analysis are extrapolated from $^{83\text{m}}\text{Kr}$ p and q values as a function of $N_{\text{tracks}}^{\text{true}}$, as described in Sec. VIII C.

V. SIMULATED CRES DATA

Simulations are an important tool in the Phase II analysis to generate inputs to the analysis model and to evaluate the performance of event detection and reconstruction methods. Simulated data are used to find numerical descriptions of the instrumental resolution \mathcal{I} (Sec. VI C) and the radiative loss spectrum \mathcal{L}_r (Fig. 8). In addition, the single deep trap K-line data of each magnetic field step in the background field scans is reproduced in simulation. This allows us to translate the measured frequency-dependent detection efficiency curve ϵ to an energy-dependent curve used in the tritium data analysis (Sec. VIII D). In Sec. V A, we discuss the basic framework and inputs to Phase II event simulations and demonstrate good agreement between simulated and real data. Section V B describes how a numerical instrumental resolution shape \mathcal{I} is constructed from an ensemble of simulated events.

A. Simulation basics and validation

The Locust package [47] simulates the detection of RF signals by modeling the response of an antenna and receiver to time-varying electromagnetic fields. Locust can independently generate a custom signal to use as input to its receiver chain algorithm, which processes the signal prior to digitization and recording. We developed a Locust signal generator module that simulates chirped signals with typical electron event properties. The Phase II waveguide and trap geometries were implemented in this generator to create realistic Phase II-like signals. Event starting conditions are sampled from probability density functions.

We generate a set of events from which the instrumental resolution \mathcal{I} can be derived. For this purpose, monoenergetic electrons are sampled at different radial and axial positions in the waveguide, and with different pitch angles, generating trajectories in response to the magnetic field map of a single-coil trap in the apparatus. To reproduce multi-trap effects (e.g. SNR and field variation differences between traps), the events from simulations with different trapping fields are combined.

The average CRES signal frequency and power are calculated from the magnetic field along the electron's trajectory and the power coupled to the TE_{11} mode. This

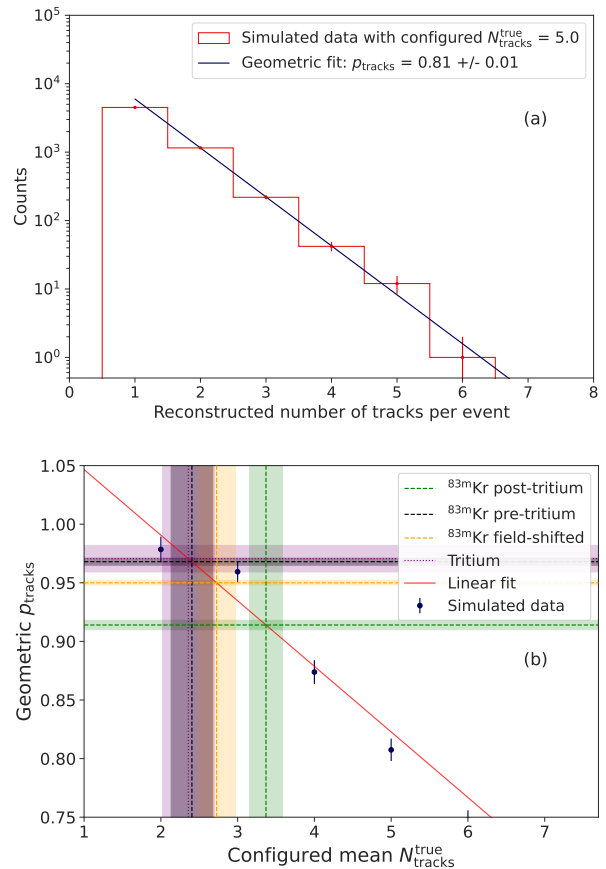


FIG. 9. Procedure for extracting the underlying mean number of tracks per event from simulations: (a) For each configured value of $N_{\text{tracks}}^{\text{true}}$, the distribution of reconstructed number of tracks per event is fitted with a geometric distribution of parameter p_{tracks} . The fit excludes the first bin since the counts are reduced in this bin by event cuts. (b) The intercepts of a linear fit to the fitted p_{tracks} for all tested $N_{\text{tracks}}^{\text{true}}$ allows us to find the optimum configuration for each data set. The uncertainty on p_{tracks} (horizontal bands) and the uncertainty of the linear fit parameters are propagated to an uncertainty on the extracted mean $N_{\text{tracks}}^{\text{true}}$ (vertical bands).

calculation accounts for the frequency modulation resulting from an electron's pitch angle [20]. Smaller pitch angles lead to reduced power in the “carrier” and more power in sidebands. Only the carrier is detected in this experiment. In the track detection process, power thresholds are applied which translate to a maximum axial excursion in the trap and a maximum variation of magnetic field seen by the electron during axial motion (see Sec. II A). The resolution \mathcal{I} thus depends on the range of SNR values accepted in analysis. Once the maximum SNR for a trap has been measured, the resolution can be predicted for any choice of threshold.

Field-shifting studies measured SNR differences between the single traps (Sec. VI D 1). These differences are accounted for by multiplying the signal power in each trap with a relative SNR factor. For generating a simu-

lated data set that can directly be compared to recorded data, the overall SNR scale is determined by iteratively adjusting the maximum coupled power until the first-track SNR distribution after reconstruction matches that of real data. The maximum coupled power corresponds to SNR_{max} , the SNR of a 90° electron at $r = 0$ mm in trap 3. This is the trap in which power is coupled most effectively into the transporting waveguide mode at the CRES frequency of the $^{83\text{m}}\text{Kr}$ K-line. Later, this procedure for setting the SNR scale is replaced by the method described in Sec. VIC 1.

To simulate multi-track events, a sequence of chirped signals is generated with start frequency and power calculated as described above and is added to a Gaussian noise floor. Track slopes are sampled from a Gaussian with a mean (352.3 MHz/s) and standard deviation (54.5 MHz/s) corresponding to the mean and standard deviation observed in the deep quad trap $^{83\text{m}}\text{Kr}$ data. The Gaussian assumption is only approximately valid, but since reconstruction efficiency is relatively insensitive to track slope as long as they are within several 100 MHz/s of the mean, achieving a better agreement of the slope distribution is irrelevant.

For each event, the track duration is drawn from a configurable exponential distribution. To propagate uncertainty on the mean track duration τ (which defines the exponential) when comparing simulated events to data, τ is drawn from a normal distribution with mean and width according to the fit results listed in Tab. II.

The number of tracks per event is drawn from a geometric distribution with a configurable expectation value. The observed mean number of tracks after event reconstruction does not correspond to the underlying truth, because regularly, tracks are missed or two tracks are combined into one during reconstruction. To find the right underlying mean number of tracks per event $N_{\text{tracks}}^{\text{true}}$, events of different $N_{\text{tracks}}^{\text{true}}$ are simulated and reconstructed using the same reconstruction methods applied in real data processing. The reconstructed number of tracks is then fitted with a geometric distribution, as shown in Fig. 9a. The success probability p_{tracks} of the fitted geometric distribution corresponds to the probability of a detected track to not be followed by another track. The relation between the reconstructed and the true mean number of tracks per event is found to be linear [25]. Figure 9b shows p_{tracks} vs. inputted $N_{\text{tracks}}^{\text{true}}$. The underlying $N_{\text{tracks}}^{\text{true}}$ for each data set can be read off from the intersection of the linear fit with the data set's p_{tracks} . For each data set, vertical bands indicate the uncertainty on $N_{\text{tracks}}^{\text{true}}$ from two contributions: the linear fit uncertainty and the p_{tracks} uncertainty.

The size of the frequency jumps between tracks is drawn from the hydrogen energy loss function from electron-molecule scattering, converted to frequency. Scattering from other gases can be neglected for obtaining \mathcal{I} , since \mathcal{I} includes only the start frequencies of first tracks, and the energy loss from scattering affects only the start frequency of consecutive tracks. Pitch angle

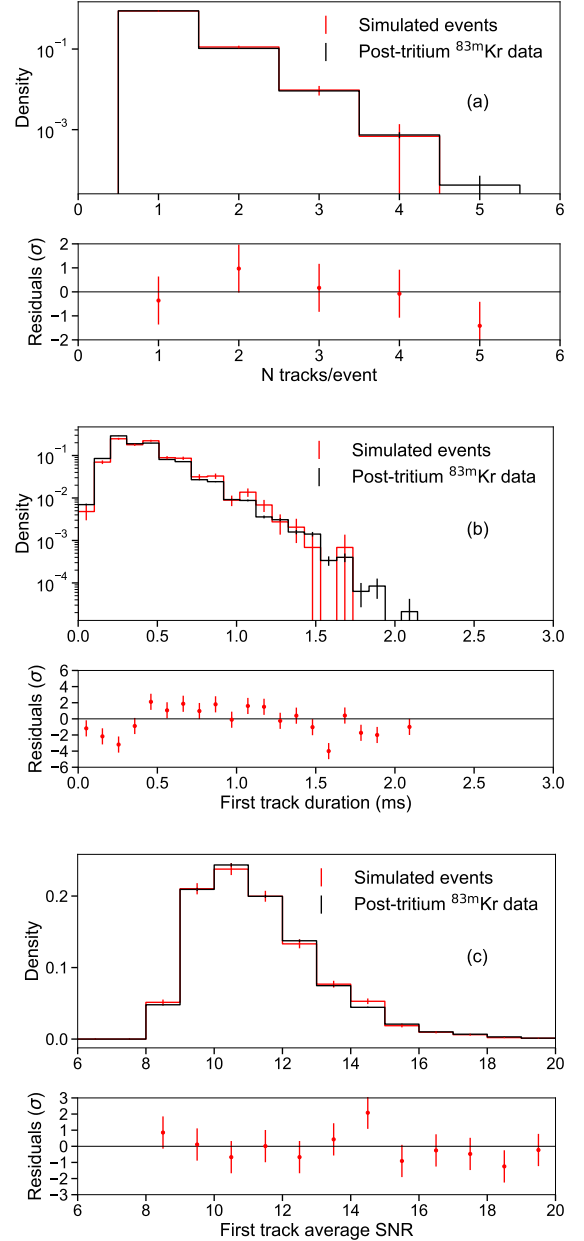


FIG. 10. Comparison of simulated data to the post-tritium $^{83\text{m}}\text{Kr}$ data set after triggering and event reconstruction: (a) number of tracks per event, (b) first track duration, and (c) first track SNR. The simulations were optimized to reproduce this data. The good agreement validates the simulations and allows to utilize them to generate simulated instrumental resolutions \mathcal{I} . For this purpose simulated data sets were generated to match each data set listed in Tab. II.

changes during inelastic scatters are assumed to be small and are ignored, and the power of consecutive tracks in an event is kept constant. Despite this approximation, after processing with the Phase II trigger and reconstruction methods, real data sets are well reproduced by simulated events in the main relevant properties: number of tracks

per event, track duration, and SNR (Fig. 10).

B. Simulated instrumental resolution

Input resolution (\mathcal{I}) shapes are required to analyze all $^{83\text{m}}\text{Kr}$ calibration data sets, shallow-trap $^{83\text{m}}\text{Kr}$ data, and tritium data. To obtain the \mathcal{I} distribution for each data set, events in all constituent single traps are simulated. For each simulated event, start frequency, number of tracks, track duration, and true power are recorded. To take into account the effect of detection efficiency, the generated events are filtered by an efficiency matrix, which is a binned look-up table of the probability for a track to be accepted as a function of SNR, track duration, and number of tracks in the event. The efficiency matrix is produced by simulating 100,000 events covering the full parameter space and analyzing the event detection probability with respect to these three decisive event properties. We use the efficiency matrix to avoid the need to process all simulated data with the trigger and reconstruction methods, thereby greatly reducing the processing time. This allows us to iteratively optimize, for example, the event SNR in a data set, with a quick turn-around time in each iteration. Before applying the efficiency filter to the tracks, the track power has to be translated to SNR. Locust adjusts the configured signal power to reflect all physical effects in the waveguide. Hence, only the power corresponding to SNR_{max} needs to be set. The optimization of SNR_{max} is described in Sec. VIC1.

The histogram of the simulated events surviving the filter constitutes the frequency resolution distribution, which is converted to an energy resolution via Eq. 2. The total \mathcal{I} is a sum of the resolutions of individual traps. For each trap, using the mapping from SNR to counts, the SNR is selected such that the number of events in the resolution distribution is proportional to the fraction of events collected in the trap in real data (see trap weight analysis in Sec. VID2). An example of a simulated \mathcal{I} is shown in Sec. VIC.

VI. CALIBRATION WITH $^{83\text{m}}\text{Kr}$

Fits to $^{83\text{m}}\text{Kr}$ electron energy lines from internal conversion are used to both test features of the apparatus setup and estimate parameters for tritium data analysis. Section VIA describes how we verify the relationship between electron energy and cyclotron frequency using simple Voigt fits to $^{83\text{m}}\text{Kr}$ lines. For all other $^{83\text{m}}\text{Kr}$ fits, instead of a Voigt profile, we employ the CRES spectrum model in Eq. 7. Accordingly, Sec. VIB, Sec. VIC and Sec. VID describe the procedure for fitting $^{83\text{m}}\text{Kr}$ lines (specifically, the 17.8-keV line) using the CRES spectrum model. Fits with this model produce estimates for the mean magnetic field B experienced by electrons, as well as the parameters p and q that control amplitudes of scatter peaks caused by missed CRES tracks.

For the fits to reliably estimate these parameters, an instrumental resolution distribution \mathcal{I} must be inputted to the fits. Section VIC describes the \mathcal{I} distributions used for $^{83\text{m}}\text{Kr}$ fits, including a procedure for finding the resolution width for each data set via an “SNR scaling optimization,” which requires additional $^{83\text{m}}\text{Kr}$ fits. Section VIC also discusses how uncertainties on \mathcal{I} are propagated to B , p and q for a $^{83\text{m}}\text{Kr}$ data set. Section VID describes how the dependence of the detection efficiency ϵ on frequency is measured by comparing the detected event rate for a range of background magnetic field values. This is the last input to the full CRES spectrum model.

Section VIE and Sec. VIF discuss how this CRES spectrum model is used to fit specific $^{83\text{m}}\text{Kr}$ data sets. In particular, Sec. VIE describes a fit to shallow-trap $^{83\text{m}}\text{Kr}$ data, which demonstrates the energy resolution capabilities of CRES. Finally, Sec. VIF discusses fits to $^{83\text{m}}\text{Kr}$ data obtained with the same deep quad trap used for tritium data. These fits most directly calibrate the tritium energy point-spread function \mathcal{R}_{PSF} . Specifically, the fit outputs are used to predict p , q and B for tritium data.

A. Test of the frequency-energy relation

To verify the predicted CRES energy-frequency relationship (Eq. 2) across a 14.3-keV range, the $^{83\text{m}}\text{Kr}$ shallow trap data included measurements of the K, L2, L3, M2, M3, N2 and N3 internal-conversion lines of the 32-keV transition. For each line, the main peak is well separated from the scattering tail and from a $^{83\text{m}}\text{Kr}$ shakeup/shakeoff structure [48], in this high-resolution trap. This makes it possible to extract frequencies by fitting the main peaks with Voigt profiles, which have fixed Lorentzian widths as tabulated in [49]. A constant background is added as a fit parameter when such a background is visible within the fit range selected around the peak. The frequencies extracted are given in Tab. IV and the fit to the K line is shown in Fig. 11.

The measured frequency of each conversion line is expected to be related to its energy according to Eq. 2. The energy of each conversion line is calculated in [49] using the 32-keV gamma energy, as well as a binding energy and recoil energy specific to that line (shown in Tab. IV). The mean magnetic field B is a fit parameter. Fig. 12 shows the frequency-energy relation, demonstrating good agreement. The magnetic field found in the fit is $B = 0.959023787(42)$ T. The points in the residual plot below the figure illustrate the good internal agreement of the data with the equation. The conversion line energies are calculated by fixing the gamma energy at the literature value 32151.6 eV provided in [49]. An improvement in the gamma energy measurement is planned by the KATRIN collaboration [50] and could also be made via CRES with a precise independent determination of the magnetic field by NMR.

TABLE IV. The frequencies of the conversion electron lines recorded in the shallow trap configuration. The N2 and N3 lines are not resolved but their frequencies are fitted separately by fixing the intensity ratio and separation between the two lines. The conversion electron line energies are calculated by fixing the gamma energy at the literature value at 32151.6 eV, and using the binding energies and recoil energies from [49]. The 0.5-eV energy scale uncertainty from the gamma energy is not included.

Line	Conversion electron energy (eV)	Binding energy (eV)	Recoil energy (eV)	Shallow trap frequency (kHz)
K	17 824.23(4)	14 327.26(4)	0.120	25 940 625.2(8)
L2	30 419.49(6)	1 731.91(6)	0.207	25 337 157.0(6)
L3	30 472.19(5)	1 679.21(5)	0.207	25 334 690.7(8)
M2	31 929.26(17)	222.12(17)	0.218	25 266 701.5(21)
M3	31 936.85(11)	214.54(11)	0.218	25 266 348.0(11)
N2	32 136.72(1)	14.67(1)	0.219	25 257 051.7(27)
N3	32137.39(1)	14.00(1)	0.219	25 257 019.2(27)

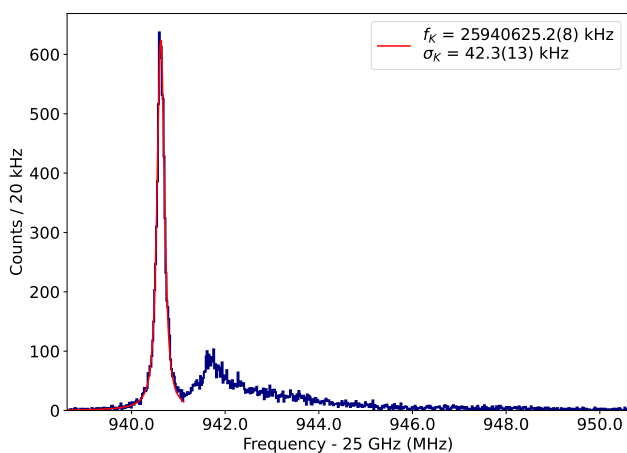


FIG. 11. The center frequency f_K of the $^{83\text{m}}\text{Kr}$ K conversion electron line in the shallow trap configuration, and the standard deviation σ_K of the instrumental resolution extracted from a fit to a Voigt profile.

B. $^{83\text{m}}\text{Kr}$ fit procedure with CRES spectrum model

For the remainder of this paper, all $^{83\text{m}}\text{Kr}$ fits use the CRES spectrum model in Eq. 7 to fit the 17.8-keV conversion-electron line. Since the structure of this CRES spectrum model is common between $^{83\text{m}}\text{Kr}$ and tritium data, we can use $^{83\text{m}}\text{Kr}$ fits to calibrate the tritium energy point-spread function \mathcal{R}_{PSF} and detection efficiency curve ϵ . The 17.8-keV $^{83\text{m}}\text{Kr}$ line is a powerful tool, given its narrow (2.774-eV) natural line width, well-understood shape, and closeness to the tritium endpoint at 18.6 keV. The underlying spectrum \mathcal{Y}_{Kr} includes the 17.8-keV $^{83\text{m}}\text{Kr}$ main peak with its natural line width, as well as a lower-energy satellite structure from shakeup and shakeoff [48].

Fits to $^{83\text{m}}\text{Kr}$ data are performed by minimizing a Pois-

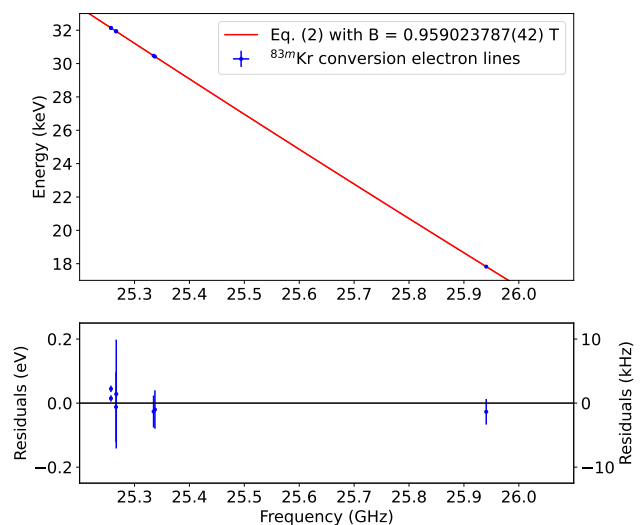


FIG. 12. Fit via Eq. 2 of the measured frequencies of conversion lines to their kinetic energies as given in Tab. IV. From right to left the lines are K, L2, L3, M2, M3, N2 and N3. The magnetic field is the fit parameter. The error bars do not include a 0.5-eV energy scale uncertainty from the gamma energy.

son likelihood χ^2 [51],

$$\chi_P^2 = 2 \sum [y_i - n_i + n_i \ln(n_i/y_i)], \quad (12)$$

where y_i is the expected number of events in bin i according to Eqs. 7 and 8, and n_i is the measured number of events in that bin. In this fit, the magnetic field B and scattering parameters p and q are left free. For the fit to the deep quad trap data, the scatter fractions γ_i are inputted, while for the shallow trap data, the scatter fractions for H_2 and He are extracted from the fit, as motivated in Sec. IV B 2. In the final fits, the detection efficiency variation with frequency ϵ (as determined in Sec. VID 1) is included in the model. No background component is included in the fits due to the short run

durations and negligible expected background rate. Section III A explains the reasons for expecting negligible background, and Sec. X B confirms this assumption.

Numerical scatter peaks serve as fixed inputs to the fitting function. These scatter peaks are produced by convolving data-set-specific simulated instrumental resolutions \mathcal{I} (see Sec. VI C) with electron energy loss spectra \mathcal{L}_{tot} . To determine \mathcal{L}_{tot} , loss spectra are combined according to Eq. 9, considering gases present in $^{83\text{m}}\text{Kr}$ data: Kr, ^3He , Ar, and H_2 and its isotopologues.

Because the spectra contain many bins with zero or few counts, goodness-of-fit testing is performed by MC sampling of the Poisson χ^2 , treating the fitted spectrum as the truth, as suggested in [51]. The Poisson χ^2 for a recorded spectrum is compared to the distribution generated from the MC simulation to check the goodness of fit.

C. Instrumental resolution \mathcal{I}

The instrumental resolution \mathcal{I} is an input to $^{83\text{m}}\text{Kr}$ fits. This resolution describes the broadening of cyclotron frequency due to the dependence on pitch angle and radius of the average magnetic field seen by a trapped monoenergetic electron. \mathcal{I} is determined for each trap configuration by simulation with Project 8's Locust software package [47] as described in Sec. V. Equations 7 and 8 show the role of \mathcal{I} in the CRES spectrum model used for $^{83\text{m}}\text{Kr}$ fits.

1. SNR scaling optimization

Each instrumental resolution \mathcal{I} has an associated value of SNR_{max} , the SNR of a 90° electron in trap 3 at $r = 0$ mm. SNR_{max} mostly affects the width of \mathcal{I} while maintaining the distribution's overall shape. In particular, higher SNR_{max} corresponds to wider \mathcal{I} distributions because the overall SNR in track bins is higher, making electrons with smaller pitch angles more detectable. These small-pitch-angle electrons explore a larger range of magnetic fields, broadening the detected frequency spectrum.

The total system gain and noise temperature are not known well enough for each data set to determine SNR_{max} . As a result, the width of \mathcal{I} is not exactly known. To find SNR_{max} for a given $^{83\text{m}}\text{Kr}$ data set, 60 fits are performed using inputted \mathcal{I} distributions corresponding to SNR_{max} values ranging from 12 to 18. When simulating these \mathcal{I} distributions, the SNR of all events is scaled relative to SNR_{max} before the efficiency filter is applied. We add a fit parameter to the $^{83\text{m}}\text{Kr}$ model: a scale factor s , which widens or compresses \mathcal{I} during the fit. When $s = 1$, this indicates that \mathcal{I} has the best width to describe the data, and thus the best SNR scale. We fit the 60 ($\text{SNR}_{\text{max}}, s$) points to a quadratic function and predict the SNR_{max} for $s = 1$. This procedure anchors

SNR_{max} to experimental data. It also produces a best-estimate for the standard deviation of \mathcal{I} , for each $^{83\text{m}}\text{Kr}$ data set.

For pre-tritium $^{83\text{m}}\text{Kr}$ data, the result of the SNR scaling procedure ($\text{SNR}_{\text{max}} = 14.3$) is shown in Fig. 13. Figure 14 displays the resulting \mathcal{I} for this data set. To simulate \mathcal{I} for the tritium analysis, we use the same SNR_{max} value as in the pre-tritium $^{83\text{m}}\text{Kr}$ data set, since its properties most closely resemble those of tritium data (see Tab. II). The two data sets are only distinguishable in track duration, which has a sub-dominant effect on the width of \mathcal{I} .

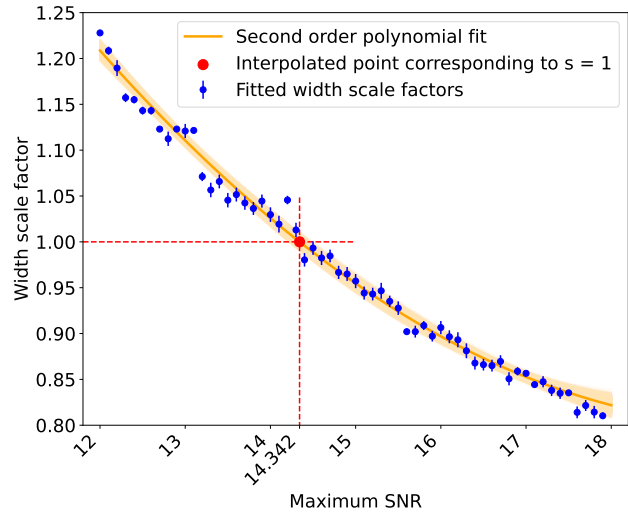


FIG. 13. SNR_{max} optimization for $^{83\text{m}}\text{Kr}$ pre-tritium data. The vertical axis is the scale factor s that adjusts the simulated width to match the experimental one for each choice of SNR_{max} in the simulation.

2. Uncertainties on \mathcal{I} propagated to $^{83\text{m}}\text{Kr}$ fit results

A simulated, fixed \mathcal{I} distribution is inputted to each $^{83\text{m}}\text{Kr}$ K-line fit listed in Tab. II. As a result, uncertainties on \mathcal{I} propagate to the fit parameter results (p , q and B), which in turn feed into the tritium analysis (see Secs. VIII A and VIII C). Thus, we estimate the uncertainties in p , q and B due to both \mathcal{I} simulation uncertainties and SNR_{max} uncertainties.

For each data set, \mathcal{I} simulation uncertainties are obtained from 100 bootstrapped resolution shapes, which are produced by repeatedly sampling counts in all bins from Gaussian distributions. Each Gaussian's standard deviation equals the bin simulation uncertainty, which includes uncertainties from Poisson counting, the efficiency matrix, and the trap weights. $^{83\text{m}}\text{Kr}$ K-line fits are then repeated 100 times, once with each bootstrapped \mathcal{I} as input, to obtain uncertainty distributions for fit parameters. Separately, we estimate the SNR_{max} contribution to $^{83\text{m}}\text{Kr}$ fit parameter uncertainties. To do so, we fit the

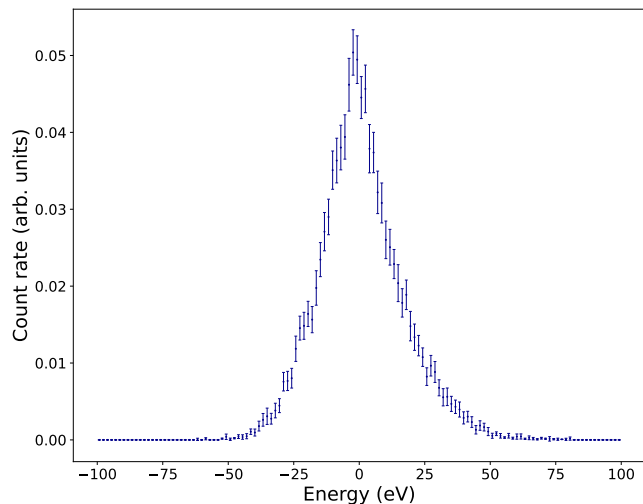


FIG. 14. Instrumental resolution \mathcal{I} of the pre-tritium $^{83\text{m}}\text{Kr}$ calibration data set. The error bars include uncertainties from Poisson counting, the efficiency matrix, and the trap weights.

data 100 times, each time using an inputted resolution simulated with a different SNR_{max} value sampled from a normal distribution (with a mean from the procedure in Sec. VI C 1 and an uncertainty calculated as described in Sec. VIII B). Simulation and SNR_{max} uncertainties are added in quadrature.

D. Field-shifted $^{83\text{m}}\text{Kr}$ data analysis

1. Detection efficiency measurement

Detection efficiency as a function of frequency is an input to the CRES spectrum model. To study the fre-

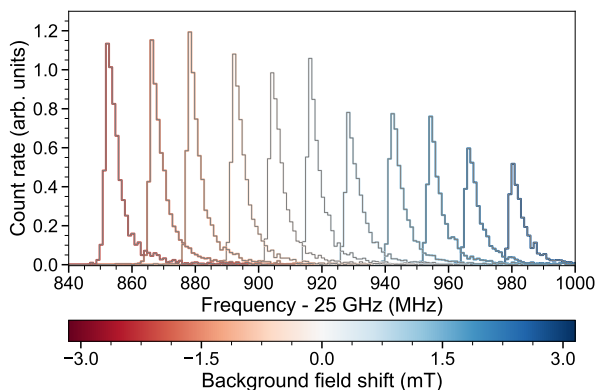


FIG. 15. The 17.8-keV $^{83\text{m}}\text{Kr}$ conversion electron line recorded in the deep quad trap at different magnetic background fields (red / blue).

quency response, we recorded $^{83\text{m}}\text{Kr}$ data at a range of background magnetic field values, as described in Sec. II A and in the “ $^{83\text{m}}\text{Kr}$ field-shifted” row in Tab. II. Data were taken in the full quad trap configuration as well as in each individual trapping coil in isolation. A subset of the $^{83\text{m}}\text{Kr}$ K-line data recorded in the quad trap configuration is shown in Fig. 15. To measure the detection efficiency vs. frequency, we extracted $\epsilon(f_c)$ at the frequency center of each recorded peak by fitting the data with a reduced version of the full CRES spectrum model that does not include $\epsilon(f_c)$. The number of reconstructed events within ± 1 MHz of the fitted peak’s frequency location is compared to the number of events for the data at the unshifted background field ($B = B_0$). The motivation for the start-frequency cut of ± 1 MHz around the peak center is to not average the detection efficiency over a larger frequency range while maintaining a high statistical precision for the efficiency analysis. The obtained relative count rate vs. frequency in a given trap (shown in Fig. 16) is equivalent to the relative $\epsilon(f_c)$ in this trap for (quasi) mono-energetic data like the $^{83\text{m}}\text{Kr}$ K-line (the energy spread of K-line electrons is small compared to the resolution width \mathcal{I}). For tritium data analysis in the quad trap, ϵ is summed from the single-trap count rates after a correction for the dependence of SNR on kinetic energy. We motivate and describe this correction in Sec. VIII D.

2. Extraction of statistical trap weights

The statistical trap weights w_i correspond to the relative number of detected events in each trap. These weights are used for two purposes: to sum the simulated instrumental resolutions of the 4 traps that compose the quad trap, and to correct the measured efficiency variation with frequency for the tritium analysis as will be discussed in Sec. VIII D 1. We extract the w_i at $B = B_0$ from the field-shifted data by minimizing the summed squared differences between the quad trap count rates vs. frequency and the weighted sum of the single-trap count rates vs. frequency, with w_i being free parameters. The resulting weights are $w_1 = 0.076(3)$, $w_2 = 0.341(13)$, $w_3 = 0.381(14)$, and $w_4 = 0.203(20)$, which are in good agreement with the observed count rate differences at $B = B_0$.

Note that the field step sizes are 0.07 mT in traps 2, 3, and the quad trap. We chose the step sizes in trap 1 and trap 4 to be 0.7 mT to reduce the total duration of these field-shifting scans for the traps with the lowest count rate at the nominal frequency position of the K-line (≈ 25.91 GHz). For the summation, the count rates from trap 1 and 4 are interpolated linearly. The uncertainties in the interpolated frequency ranges are taken to be equal to the largest deviation from a linear interpolation over the same range in trap 2 or 3 (shown in grey in Fig. 16).

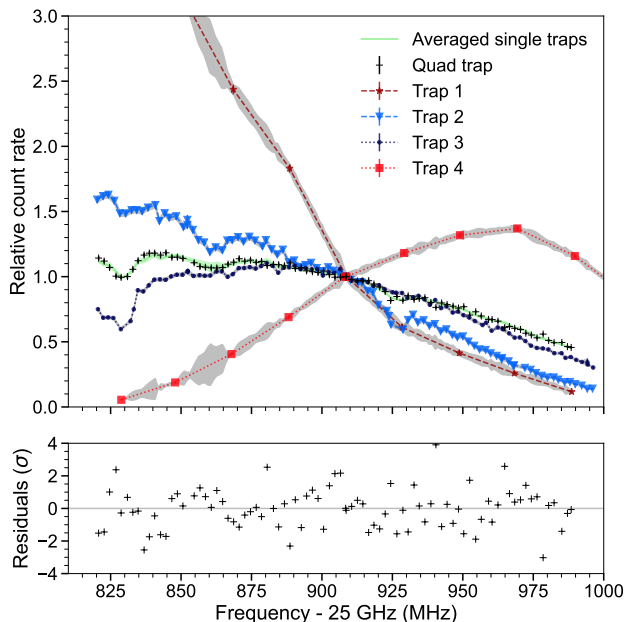


FIG. 16. Event detection rates from $^{83\text{m}}\text{Kr}$ K-line data recorded with different single-coil traps (red and blue) and the quad trap (black) in field-shifted data relative to the respective count rate at $f_c \approx 25.91$ GHz (where $B = B_0$). The uncertainties on interpolation are shown in grey. The relative count rates can be summed with weights (green) to match the quad-trap count rate curve (black). The residuals show the differences of the summed single-trap rates and the quad-trap rates divided by the quad-trap count rate uncertainties. The standard deviation of the residuals is larger than 1 and the uncertainties on the tritium efficiency ϵ (Sec. VIII D 1) are inflated to account for this.

E. $^{83\text{m}}\text{Kr}$ shallow-trap data and fits

To explore the best resolution achievable in Phase II, and to test the CRES spectrum model (Eq. 7), we took $^{83\text{m}}\text{Kr}$ data with the trap coil currents set to the shallow trap configuration in Fig. 2. Figure 17 shows the fit to these data. Also shown is the underlying $^{83\text{m}}\text{Kr}$ lineshape model \mathcal{Y}_{Kr} , which includes both the main peak and the shakeup/shakeoff satellites. The figure displays intermediate lineshapes in which additional model elements are added one by one, to exhibit the effects of magnetic field inhomogeneity (treated as equivalent to instrumental resolution \mathcal{I}) and scattering. In the shallow trap, there are only small differences between the average magnetic fields experienced by trapped electrons with different pitch angles. Accordingly, the broadening from \mathcal{I} (purple curve) is 1.66(19) eV FWHM. This combines with the natural linewidth of 2.774 eV FWHM [52] to produce a main peak with a FWHM of 4.0 eV. The Gaussian component of the Voigt profile used in Fig. 11 has a FWHM of 2.10(6) eV, in reasonable agreement given that \mathcal{I} is not Gaussian. Out of all events, 69% are detected before scattering. Additional curves in Fig. 17 show events detected after

a single scatter and after up to 20 scatters. In the low-energy tail (below 17.814 eV), scattering events comprise 61% of counts.

The summed χ^2 of the binned data falls within 1σ of the mean of the distribution of summed χ^2 values from MC simulations, verifying goodness of fit. This demonstrates the high-resolution capabilities of CRES and validates the $^{83\text{m}}\text{Kr}$ model.

F. $^{83\text{m}}\text{Kr}$ pre-tritium and post-tritium quad trap data and fits

For the small apparatus in Project 8's Phase II, low statistics are the limiting factor in neutrino mass sensitivity. Thus, to maximize statistics, we took the final tritium data in a trap configuration, shown in Fig. 2, that was deeper than the shallow trap and was composed of four individual traps rather than two. The $^{83\text{m}}\text{Kr}$ pre-tritium and post-tritium data sets (see Tab. II) were taken in the same deep quad trap, to provide calibrations of the effective mean magnetic field B and the scattering parameters p and q as inputs for the tritium analysis. Fig. 18 shows the $^{83\text{m}}\text{Kr}$ pre-tritium data and fit.

The $^{83\text{m}}\text{Kr}$ line shape is significantly broadened by the 35.6 eV FWHM instrumental resolution \mathcal{I} , due to the larger range of trapped pitch angles, and therefore larger range of average magnetic fields, experienced by electrons in this deeper trap. The larger pitch angle acceptance causes more electrons to remain trapped after scattering, leading to a higher average number of tracks per event. The larger acceptance also means that events that begin in non-detectable pitch angles have a larger phase space of detectable pitch angles to scatter into; therefore, de-

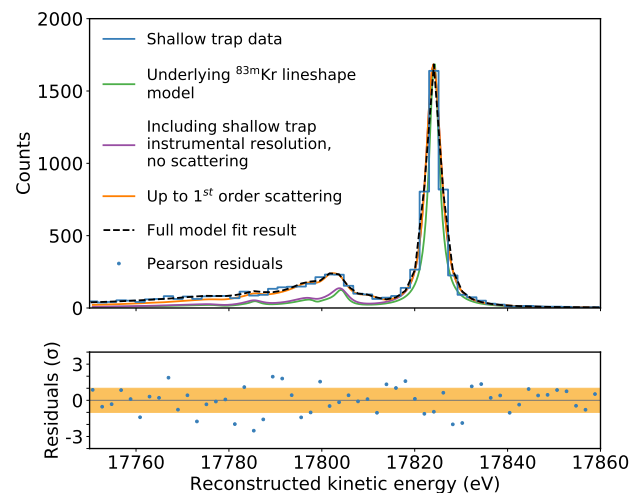


FIG. 17. The 17.8-keV $^{83\text{m}}\text{Kr}$ K-conversion electron line, as measured with CRES in the shallow (high-resolution) electron trapping configuration, with FWHM of 4.0 eV. The data are the $^{83\text{m}}\text{Kr}$ shallow data set (Table II).

tected events are more likely to come from this pool. Therefore, a smaller proportion (53%) of events are detected before scattering in the deep quad trap than in the shallow trap. This gives rise to the enhanced low-energy tail and brings the FWHM to 54.3 eV. Note that for the shallow trap spectrum, the scattering peaks contribute minimally to the width, while for the deep quad trap data, the scattering accounts for a significant portion of the width.

1. Uncertainties on $^{83\text{m}}\text{Kr}$ quad trap fit results

For the $^{83\text{m}}\text{Kr}$ pre-tritium and post-tritium data sets, the comparison of the summed χ^2 for binned data with that of the MC simulation indicated underfitting. To account for the uncertainty associated with this tension, the uncertainties for B , p and q from the maximum likelihood fit are inflated by 17% and 5% for the pre-tritium and post-tritium data sets, respectively. These fit uncertainties are combined with the larger uncertainty contributions from \mathcal{I} and gas composition to produce the total uncertainties on B , p and q .¹ Uncertainties on \mathcal{I} are propagated using the sampling-and-refitting method described in Sec. VIC2. The uncertainty on \mathcal{I} due to SNR_{max} is not propagated to B , since those variables are independent. SNR_{max} primarily affects the width of \mathcal{I} , while B controls the location of the distribution's

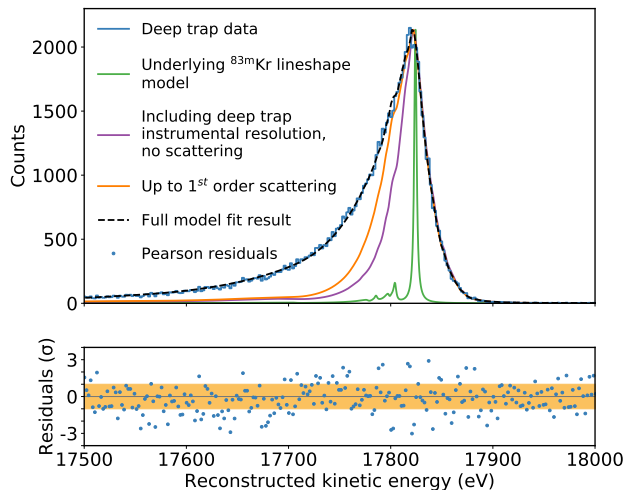


FIG. 18. The 17.8-keV $^{83\text{m}}\text{Kr}$ K-conversion electron line, as measured with CRES in the deep (high-statistics) electron trapping configuration, with FWHM of 54.3 eV. The data are the $^{83\text{m}}\text{Kr}$ pre-tritium data set (Table II).

¹ When fit uncertainties are inflated to account for underfitting, this increases the total uncertainties on B , p and q by only 1.6%, 0.3% and 0.1%, respectively.

center; these are two separate moments of \mathcal{I} . To propagate the uncertainty from gas composition, the $^{83\text{m}}\text{Kr}$ fits are repeated 300 times while sampling the inputted gas scattering contributions from the distributions defined in Tab. III. The gas composition uncertainties on B , p and q are the standard deviations of results from these 300 fits.

With fit, \mathcal{I} , and gas composition uncertainties included, the best estimates of B from $^{83\text{m}}\text{Kr}$ pre- and post-tritium data differ by 1.6σ . Estimates for p and q are not expected to be consistent between the two quad trap data sets, due to a difference in the mean number of tracks per event (see Sec. VIII C).

2. Validating $^{83\text{m}}\text{Kr}$ scatter peak amplitudes with simulation

The amplitude $\mathcal{A}_j(p, q)$ of scatter peak j is proportional to the probability of missing j tracks before detecting an event. Simulations are used to validate the model for \mathcal{A}_j (Eq. 11) as well as the fitted values of p and q for quad trap $^{83\text{m}}\text{Kr}$ data.

In the Locust simulations performed to obtain the instrumental resolution \mathcal{I} , pitch angle changes are ignored and assumed to be zero. When one is concerned with the properties of first tracks (e.g., the start frequency spread captured by \mathcal{I}), that approach is sufficient. However, this simplification does not allow the prediction of accurate \mathcal{A}_j values. Therefore, we perform a set of toy model simulations (not using Locust) in which inelastic and elastic scattering are modeled separately, with pitch angle changes included. The simulated events are not processed with the Phase II event reconstruction algorithms. Instead, the event detection process is approximated by power and track length cuts.

For the simulations, it is assumed that inelastic scattering leads to energy loss and small pitch angle changes, while elastic scattering removes electrons from the trap before the next inelastic scattering event [27]. The inelastic scattering angle θ follows the distribution [53]

$$P(\theta) \propto \left(1 + \frac{\cos^2 \theta}{\alpha^2}\right)^{-1}, \quad (13)$$

where α is a data-set-specific constant. The elastic scattering is modeled by assuming a fixed fraction κ of electrons leave the trap between inelastic scatters due to elastic scatters. As before, the track duration follows the exponential distribution in Eq. 5. The coupled power from a radiating electron is calculated given its instantaneous pitch angle and axial position. The detection status of an electron is determined by whether the electron power and track length are both above the corresponding preset thresholds. The SNR threshold chosen matches the threshold applied to tracks in real data by the Phase II track detection algorithm, prior to combining single tracks into full events (see [25]). Similarly to in Sec. V A, it is assumed that the highest simulated power

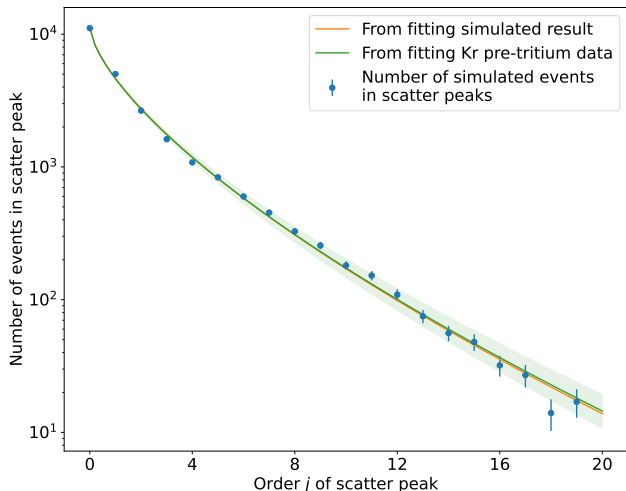


FIG. 19. Number of simulated events that are detected after j scatters. The relative scatter amplitudes \mathcal{A}_j (modeled by Eq. 11) result from the combination of track detection probability and pitch angle changes for electrons after scattering (modeled by Eq. 13). The number of detected electrons in each scatter can be modeled by a modified exponential function (solid lines) parameterized by p and q . Fitting p and q for pre-tritium $^{83\text{m}}\text{Kr}$ data results in an \mathcal{A}_j curve (green) in very good agreement with simulation (orange).

corresponds to the estimated maximum SNR observed in data. The power of all simulated events is translated to SNR accordingly. The track length detection threshold is set to the minimum recorded track length in data. Tuning α and κ , the \mathcal{A}_j curve and the mean event length can be simultaneously matched to values extracted from $^{83\text{m}}\text{Kr}$ data (see Fig. 19).

This simulation cannot be directly used to predict \mathcal{A}_j in tritium data, since α and κ are related to the gas composition and differ among data sets. Instead, the values of p and q for tritium data are found by extrapolating from the p and q results of the pre-tritium and post-tritium $^{83\text{m}}\text{Kr}$ fits, as described in Sec. VIII C.

VII. TRITIUM MODEL

A. An analytic model for tritium data analysis

This section describes an analytic model of tritium CRES data. The model is used in Bayesian and frequentist analyses (discussed in Sec. IX) to measure the tritium endpoint E_0 and to place a limit on the neutrino mass m_β . The tritium model has a similar structure to the $^{83\text{m}}\text{Kr}$ model, with differences as described in subsections B-D, below.

In the tritium model, the beta spectrum $\mathcal{Y}_{\text{tritium}}$ and response function \mathcal{R}_{PSF} are approximated to make it possible to analytically convolve the two functions, producing a fully analytic likelihood model. This en-

ables computationally efficient inference. Such efficiency is crucial for the Bayesian analysis (described in Sec. IX A 1), since algorithms that perform Bayesian inference in many dimensions—corresponding to many nuisance parameters—tend to be slow at numerical integration. The analytic model of \mathcal{R}_{PSF} also substantially speeds up the calculation of the response in the frequentist inference.

The tritium model described below includes several approximations, since a more exact model would be non-analytic. These approximations have a minimal effect on E_0 and m_β results. Monte Carlo studies test the impact of approximations, as discussed in-detail in Sec. IX B.

B. Tritium beta decay model

In the tritium model, the underlying spectrum $\mathcal{Y}_{\text{tritium}}$ is the tritium beta spectrum, given by the product of neutrino and electron phase space density factors D_ν and D_e . Equation 7 shows how this underlying spectrum is used in the full model for CRES data. When experimental sensitivity is insufficient to resolve individual mass eigenstates, the beta spectrum is given by [7]

$$\begin{aligned} \mathcal{Y}_{\text{tritium}} &= D_\nu \cdot D_e, \quad \text{where} \\ D_\nu &\propto \epsilon [\epsilon^2 - m_\beta^2]^{1/2} \Theta(\epsilon - m_\beta) \\ D_e &\propto F(Z, p_e) p_e E_e. \end{aligned} \quad (14)$$

In this equation, $\epsilon = E_0 - E_{\text{kin}}$, Θ is the Heaviside step function, $F(Z, p_e)$ is the relativistic Fermi function for charge $Z = 2$ of the daughter nucleus, and p_e are E_e are the electron momentum and total energy, respectively. The frequentist analysis model uses Eq. 14 for the beta spectrum.

In the Bayesian analysis, D_ν is approximated according to the formalism in [15]. This involves Taylor expanding in m_β^2 to produce the expression

$$D_\nu \approx [\epsilon^2 - m_\beta^2/2] \Theta(\epsilon - m_\beta). \quad (15)$$

In addition, D_e is Taylor expanded to first order around the energy at the center of the analysis region of interest (ROI), neglecting atomic physics factors that correct the Fermi function. These are good approximations for the Phase II event rate and ROI. The resulting model for $\mathcal{Y}_{\text{tritium}}$ may be analytically convolved with a normal distribution. Thus, for any model of \mathcal{R}_{PSF} that is expressed as a weighted sum of Gaussians, the full tritium model is analytic. This enables computationally efficient inference, as was discussed in Sec. VII A. Here, unlike in Ref. [15], the low-energy edge of the spectrum is not smeared out by magnetic field broadening, since a hard maximum-frequency cut is performed before analysis.²

² A low-energy smearing of 0.001 eV is included in the model for

The decay of molecular tritium creates a daughter molecule, ${}^3\text{HeT}^+$, that can be in an excited state. Thus, a beta spectrum fit must account for the final state distribution, i.e., the probability distribution for how much energy is supplied to rotational, vibrational, and electronic excitations of ${}^3\text{HeT}^+$ during the decay. We use the distribution calculated by Saenz et al. for ${}^3\text{HeT}^+$ [12]. Neglecting this final state distribution leads to a bias of $-8.1(8)$ eV on the endpoint energy, as determined by a Bayesian MC study. The analysis model uses a sparse approximation of the calculated distribution [12], shown in Fig. 20. This saves computational time and, as determined by an MC study, does not introduce bias in the results. The full tritium signal model is a weighted sum of beta decay signal functions with binding energies at the sparse values in Fig. 20, with the overall rate of each function scaled by the final state probability. This serves to discretely convolve the final state distribution with the beta spectrum.

We neglect contributions from the atomic tail extending to beyond 1 keV below the endpoint; these contributions are highly suppressed and have no measurable effect on the results. While some electrons are produced by HT, which decays to ${}^3\text{HeH}^+$, this molecule’s final state distribution is very similar to that of ${}^3\text{HeT}^+$, so the difference can be ignored for the energy point-spread function \mathcal{R}_{PSF} of our deep quad trap.

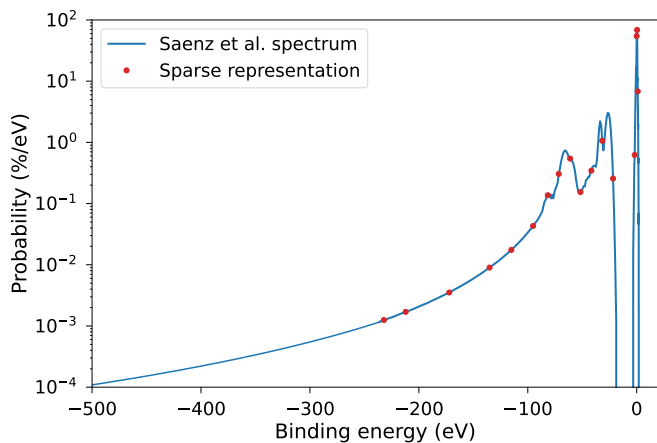


FIG. 20. Molecular final states of ${}^3\text{HeT}^+$ as calculated in [12] and the sparse approximation used in this analysis.

C. Tritium energy response function model

The β -spectrum is convolved with \mathcal{R}_{PSF} , the energy response point-spread function. \mathcal{R}_{PSF} is modeled as a sum

computational stability (negligibly affecting analysis results). In a Bayesian MCMC analysis, infinitely steep drops in probability density can cause Markov chains to behave pathologically [54, 55].

of Gaussians, as motivated in Sec. VII A and Sec. VII B. As in the case of ${}^{83\text{m}}\text{Kr}$ data, \mathcal{R}_{PSF} is composed of scatter peaks $\mathcal{I} * \mathcal{L}_{\text{tot}}^{*j}$ (see Eq. 8). The scatter spectrum model includes gases H_2 and ${}^3\text{He}$, as these have the largest inelastic scatter fractions γ_i in tritium data: 0.911(45) and 0.075(40), respectively (see Sec. III C on scatter fraction analysis). At each successive scattering, the electron may scatter from H_2 or ${}^3\text{He}$ in proportion to the species’ abundance and cross section. We simplify by modeling each scatter peak as a weighted sum of H_2 and ${}^3\text{He}$ peaks (akin to assuming that each electron scatters off of the same gas type at the end of all missed tracks). An MC study confirmed that this simplification does not alter E_0 and m_β results. Additional MC studies show that we may neglect a small scatter fraction 0.014(9) of carbon monoxide present in tritium data, as well as energy loss from cyclotron radiation.

In the tritium model, each scatter peak $\mathcal{I} * \mathcal{L}_{\text{tot}}^{*j}$ is expressed as a function of σ , the calculated standard deviation of the simulated tritium resolution \mathcal{I} . This enables us to propagate the uncertainty on the resolution width to the endpoint and neutrino mass, via σ . The $j = 0$ peak is modeled separately from the $j \geq 1$ peaks, as described below. The model includes $j_{\text{max}} = 20$ peaks, since an MC study shows that higher-order peaks have no noticeable effect on results.

For $j = 0$, the “scatter peak” reduces to \mathcal{I} . The procedure for simulating \mathcal{I} is described in Sec. V B. Because the $j = 0$ peak contributes the most events to \mathcal{R}_{PSF} , it is important to model the peak with a closely-fitting distribution. A simple Gaussian would underestimate the tails of the simulated peak and fail to account for the distribution’s small asymmetry. Instead, \mathcal{I} is fitted with a sum of two Gaussians, each described by a mean $\mu_0^{[i]}$ and standard deviation $\sigma_0^{[i]}$, with the distributions then weighted by a parameter $0 \leq \eta \leq 1$:

$$\mathcal{I} * \mathcal{L}_{\text{tot}}^{*0} \approx \eta \mathcal{N}(\mu_0^{[1]}, \sigma_0^{[1]}(\sigma)) + (1 - \eta) \mathcal{N}(\mu_0^{[2]}, \sigma_0^{[2]}(\sigma)). \quad (16)$$

As noted above, each scatter peak should be parameterized in terms of σ . Accordingly, the Gaussian standard deviations in Eq. 16 must be functions of σ . To find these functions, we perform fits to simulated resolutions with a range of σ values and observe how $\sigma_0^{[1]}$ and $\sigma_0^{[2]}$ depend on σ . To vary σ in the simulations, the value of SNR_{max} is varied. As discussed in Sec. VI C 1, σ is determined primarily by SNR_{max} . The result of this procedure is $\sigma_0^{[1]}(\sigma) = 1.1\sigma + 1.9$ eV and $\sigma_0^{[2]}(\sigma) = 0.8\sigma - 3.7$ eV.³ This procedure also demonstrates that $\eta = 0.66$ is constant as

³ To determine these expressions for $\sigma_0^{[1]}$ and $\sigma_0^{[2]}$, we use three pieces of information:

1. Simulations show that $\sigma_0^{[2]} = 0.8\sigma_0^{[1]} - 5.2$ eV for our instrumental resolution. We observe this linear relation by gen-

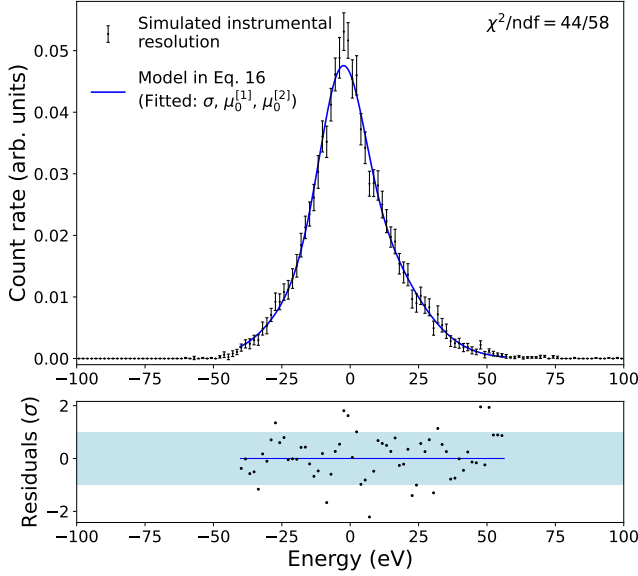


FIG. 21. Fit of Eq. 16 to the simulated instrumental resolution \mathcal{I} for tritium data. Bin errors are approximately Gaussian, from sources described in Sec. VI C. Fit parameters are means of the two normal distributions ($\mu_0^{[1]}$, $\mu_0^{[2]}$) and the resolution standard deviation σ . The fraction of counts η in the first normal distribution is inputted; we use the average η from fits to 100 resolutions with different σ values.

σ varies. By fixing η and plugging the expressions for $\sigma_0^{[1]}(\sigma)$ and $\sigma_0^{[2]}(\sigma)$ into Eq. 16, we obtain a model with only three free parameters: σ , $\mu_0^{[1]}$ and $\mu_0^{[2]}$. This “reduced model” fits the simulated resolution data closely. As a check, we confirm that the fitted value of σ matches the standard deviation σ calculated from points in a given \mathcal{I} distribution.

The reduced model for the $j = 0$ peak can scale in width based on the σ parameter, and the model captures the slight asymmetry in \mathcal{I} via $\mu_0^{[1]}$ and $\mu_0^{[2]}$. For tritium data analysis, to find best estimates of σ , $\mu_0^{[1]}$ and $\mu_0^{[2]}$, we

erating 100 simulated resolutions with different maximum detectable track SNRs (SNR_{max}), then fitting each resolution with Eq. 16. The size of SNR_{max} controls the width of \mathcal{I} (see Sec. VI C). In these fits, the Gaussian means, Gaussian standard deviations and η are all fitted.

2. We observe that $\sigma \approx \eta\sigma_0^{[1]} + (1-\eta)\sigma_0^{[2]}$ for the same 100 simulated resolutions. The relation is approximate because an exact expression for σ must depend on $\mu_0^{[1]}$ and $\mu_0^{[2]}$. In that relation, the right hand side is computed from fit results, and σ is calculated directly from the simulated resolutions.
3. We observe that $\eta = 0.66$ is constant within fit errors, for the SNR_{max} uncertainty range in tritium data (quantified in Sec. VIII B).

Combining the first and second relations, and fixing η , we find $\sigma_0^{[1]}(\sigma)$ and $\sigma_0^{[2]}(\sigma)$ —expressions that depend only on σ and constants.

fit the reduced model to an \mathcal{I} distribution generated with the best-estimate SNR_{max} value. Figure 21 displays this distribution and fit curve ($\chi^2/\text{ndf} = 44/58$). The fit energy range is limited to produce a good fit to the central region of the resolution, which has the largest impact on the tritium analysis. Uncertainties on σ are propagated to the endpoint and neutrino mass results (see Sec. VIII B), since these results would shift if we under- or over-estimated the widths of scatter peaks. In contrast, $\mu_0^{[1]}$ and $\mu_0^{[2]}$ are fixed in the tritium model because their uncertainties are found to have a negligible effect and are not propagated.

When $j \geq 1$, scatter peaks $\mathcal{I} * \mathcal{L}_{(\text{H}_2, \text{He})}^{*j}$ are again modeled as a function of the resolution standard deviation σ . Monte Carlo studies show that these higher-order peaks can each be modeled as Gaussian without biasing E_0 or m_β results, despite the asymmetry in $\mathcal{L}_{\text{tot}}^{*j}$. This is the case because the peaks are broadened by \mathcal{I} , they overlap with each other, and they each contribute sub-dominantly to the \mathcal{R}_{PSF} . Employing Gaussian distributions allows analytic convolution of \mathcal{R}_{PSF} with the β -spectrum model, simplifying computation, as discussed in Sec. VII A and Sec. VII B. For a given gas species, each scatter peak term is characterized by a mean and standard deviation that depend only on σ . The full scatter peak is a weighted sum of these terms:

$$\begin{aligned} \mathcal{I} * \mathcal{L}_{\text{tot}}^{*j} (j \geq 1) &\approx \gamma_{\text{H}_2} \left[\mathcal{I} * \mathcal{L}_{(\text{H}_2)}^{*j} \right] + (1 - \gamma_{\text{H}_2}) \left[\mathcal{I} * \mathcal{L}_{(\text{He})}^{*j} \right] \\ &\rightarrow \gamma_{\text{H}_2} \mathcal{N} \left(\mu_j^{\text{H}_2}(\sigma), \sigma_j^{\text{H}_2}(\sigma) \right) + (1 - \gamma_{\text{H}_2}) \mathcal{N} \left(\mu_j^{\text{He}}(\sigma), \sigma_j^{\text{He}}(\sigma) \right), \end{aligned} \quad (17)$$

where γ_{H_2} is the hydrogen inelastic scatter fraction and $1 - \gamma_{\text{H}_2}$ is the helium inelastic scatter fraction. The Gaussian means μ_j depend on σ because \mathcal{L}_{tot} is asymmetric, so the convolution with \mathcal{I} can shift the center of each scatter peak when σ is large enough (as is the case for deep quad trap data).

The slopes and y -intercepts of $\mu_j(\sigma)$ and $\sigma_j(\sigma)$ are fixed during tritium data analysis, so the scatter tail shape depends only on σ , γ_{H_2} and scatter peak amplitudes. For each gas, the slopes and intercepts for μ_j and σ_j are determined through the following procedure. For a given j , we fit Gaussians to 20 sets of scatter peaks broadened by 20 different resolution widths, ranging from 0.5σ to 1.5σ . This procedure produces μ_j and σ_j for a range of σ values. We then observe and fit the linear dependence of μ_j and σ_j on σ .

Combining the $j = 0$ and $j \geq 1$ scatter peaks, the full tritium-specific model for \mathcal{R}_{PSF} includes a limited set of free parameters with propagated uncertainties. Those parameters are γ_{H_2} , σ , and the two variables p and q , which control the amplitudes \mathcal{A}_j of all scatter peaks.

Each amplitude \mathcal{A}_j multiplies the j^{th} broadened scatter peak in Eq. 16 or 17. The tritium and $^{83\text{m}}\text{Kr}$ models for $\mathcal{A}_j(p, q)$ are identical; see Sec. IV B. Tritium-specific p and q values are estimated by slightly shifting p and q

from the fit to $^{83\text{m}}\text{Kr}$ pre-tritium data (see Sec. VIF), to account for a difference in the mean number of tracks per event ($N_{\text{tracks}}^{\text{true}}$) between the pre-tritium and tritium data sets. The procedure for estimating p and q for tritium data is described in more detail in Sec. VIIC.

D. Binned event rate model

Per the full CRES spectrum model (Eq. 7), we convolve the above models for the beta spectrum and \mathcal{R}_{PSF} , then multiply the result by ϵ_k , the detection efficiency for frequency bin k (see Sec. VIID4). This produces $S_k(E_{\text{kin}})$, the signal probability density function within bin k . In addition, a false event probability density function $\mathcal{F}(E_{\text{kin}})$ is introduced. $\mathcal{F}(E_{\text{kin}})$ is assumed to be flat in energy because the probability to measure RF noise (the only potentially significant expected background source; see Sec. IIIA) is uniform as a function of cyclotron frequency, and energy is approximately linearly related to frequency over a limited range. Combining signal and background, the expected tritium event rate within bin k is

$$\left(\frac{dN}{dE_{\text{kin}}}\right)_k(E_{\text{kin}}) = r_s S_k(E_{\text{kin}}) + r_f \mathcal{F}(E_{\text{kin}}), \quad (18)$$

where r_s is the signal rate and r_f is the false event rate. Binning is handled differently in Bayesian and frequentist analyses, as discussed further in Sec. IX. During analysis, for all bins, cyclotron frequencies are converted to energies according to Eq. 2, using the magnetic field B from the $^{83\text{m}}\text{Kr}$ fit procedure in Sec. VIF. The parameter B is discussed further in Sec. VIIA.

VIII. TRITIUM PARAMETER ESTIMATES AND UNCERTAINTIES

We study and quantify the following systematic effects for the tritium data analysis:

1. The mean magnetic field B that converts cyclotron frequencies to energies;
2. The tritium-specific simulated instrumental resolution \mathcal{I} , which determines σ ;
3. Scatter peak amplitudes \mathcal{A}_j (parameterized by p and q);
4. The energy-dependent event detection efficiency ϵ ;
5. The frequency dependence of the energy point-spread function \mathcal{R}_{PSF} (specifically, of σ , p , and q); and
6. Gas composition, which determines the hydrogen inelastic scattering fraction f_{H_2} in tritium data.

This section covers items 1-5. Item 6—gas composition and associated uncertainties—was discussed in Sec. IIIC and Sec. VIIC.

Systematic factors affect the tritium data analysis via three pathways. First, $^{83\text{m}}\text{Kr}$ -specific estimates of some uncertainties (on simulated resolutions and gas composition) are incorporated into the $^{83\text{m}}\text{Kr}$ quad trap analysis and propagated to B , p and q —the three tritium model parameters from $^{83\text{m}}\text{Kr}$ fits. Second, tritium-specific estimates of some uncertainties (on σ and f_{H_2}) are directly employed in tritium data analysis and propagated to the endpoint E_0 and neutrino mass m_β as described in Sec. IX. Third, $^{83\text{m}}\text{Kr}$ fits are used to estimate the variation of parameters (ϵ , σ , p and q) across the tritium ROI, as well as the uncertainty on this variation.

Below, we describe procedures for estimating parameters in the tritium model, their systematic uncertainties, and where relevant, their correlations. At the end of this section, Sec. VIIF summarizes the probability distributions for all tritium model parameters, which account for uncertainties on these parameters.

A. Mean magnetic field B

During tritium data analysis, the average magnetic field B experienced by electrons in the deep quad trap is used to convert event-start frequencies f_c to energies E_{kin} via Eq. 2. The energies then enter into the tritium model in Eq. 18. A systematic uncertainty in B shifts the overall reconstructed energy scale, so uncertainties in B are expected to propagate to E_0 . By contrast, the m_β determination is unaffected by the B systematic, since m_β is altered by the second moment of the energy PSF (spectral broadening), not the first moment (overall energy scale) [56].

The best estimate for B is determined by fitting $^{83\text{m}}\text{Kr}$ pre-tritium quad trap data, following the procedure described in Sec. VI. We choose this data set because its event features most closely resemble those of tritium data. In particular, as shown in Tab. II, the pre-tritium mean track duration differs from that of tritium data by 10% (compared with 29% for post-tritium data), and the pre-tritium mean number of tracks differs by 2% (compared with 43% for post-tritium data). This choice minimizes differences between parameters fitted from $^{83\text{m}}\text{Kr}$ data and tritium parameters. Pre- and post-tritium estimates of B differ by 1.6σ (see Sec. VIF1); indicating that the impact of discrepancies in data-taking conditions on B is relatively small. The best estimate for B is shifted downward by 5×10^{-7} T to correct for the 14 kHz (0.3 eV) mean error in start frequencies from reconstruction. The uncertainty on this shift contributes negligibly to the B uncertainty.

The uncertainty on B includes three contributions from the $^{83\text{m}}\text{Kr}$ quad trap fitting process, which were described in Sec. VIF1. These contributions are the statistical uncertainty outputted by the $^{83\text{m}}\text{Kr}$ maximum

likelihood fit ($\pm 3 \times 10^{-7}$ T), the uncertainty in the gas composition of pre-tritium $^{83\text{m}}\text{Kr}$ data ($\pm 7 \times 10^{-7}$ T), and simulation uncertainties on the instrumental resolution input to the $^{83\text{m}}\text{Kr}$ fit ($\pm 5 \times 10^{-7}$ T). Combining the three uncertainties in quadrature, we measure a mean magnetic field of $B = 0.9578099(9)$ T. Separately, there is a magnetic field uncertainty from a 0.5 eV uncertainty on the $^{83\text{m}}\text{Kr}$ K-line energy [49]. Accounting for the external K-line uncertainty, we find $B = 0.9578104(13)$ T for the tritium analysis.

B. Energy resolution σ

The simulated resolution \mathcal{I} for the tritium data analysis differs from the resolutions used for quad trap $^{83\text{m}}\text{Kr}$ analyses due to slight differences in mean track duration and mean number of tracks per event (see Sec. V). The standard deviation σ of the tritium resolution is estimated by fitting the tritium-specific simulated resolution with the model in Eq. 16. The best fit result is $\sigma = 15.10$ eV. In the tritium data fits, we include two types of uncertainties on the resolution parameter σ : (a) uncertainties from the \mathcal{I} simulation process, and (b) an uncertainty on the optimized SNR_{max} value. The procedures for determining (a) and (b) are described below.

There are three contributions to the simulation uncertainty (a): first, Poisson errors on the number of simulated events; second, uncertainties in the efficiency matrix (see Sec. VB); and third, the uncertainty in the number of events contributed from each magnetic trap in the quad trap. The resulting bin errors are propagated to each bin of the histogrammed start frequencies that comprise the simulated resolution. Combined, these uncertainties are approximately Gaussian and are included in a χ^2 fit of \mathcal{I} using Eq. 16. Accordingly, the 0.22-eV uncertainty on σ that the fit outputs accounts for simulation uncertainties.

The SNR_{max} in the tritium simulation (b) also affects σ . To estimate the SNR_{max} uncertainty, we compared the optimal SNR_{max} from Sec. VIC 1 (14.3) with the result from an alternate method, the first-track SNR matching described in Sec. VA. This produced an estimate of $\text{SNR}_{\text{max}}=18.0$. The result of the method in Sec. VIC 1 provides the SNR_{max} best estimate, because that method ensures that the distribution's width is consistent with data—our primary concern when estimating σ . Still, the discrepancy between the two estimates sets the uncertainty scale, as it quantifies the impact of small imperfections in the resolution simulation (for example, mis-modeling of pitch angle changes from scattering, which could not be directly compared to data). Thus, we take the SNR_{max} uncertainty to be half the difference between the two estimates: 1.85. This is larger than the uncertainty from the procedure in Sec. VIC 1 (0.15) and twice the difference between the optimal SNR_{max} values for pre- and post-tritium $^{83\text{m}}\text{Kr}$ data, suggesting that the uncertainty of 1.85 may be conservative.

To find the corresponding uncertainty on σ , we fit Eq. 16 to 100 tritium-specific resolutions, each simulated with an input SNR_{max} sampled from a normal distribution with a mean of 14.3 and standard deviation of 1.85. The σ uncertainty contribution from SNR_{max} is then 1.73 eV, the standard deviation of the 100 fit results. Combining simulation and SNR_{max} uncertainties in quadrature, we find $\sigma = 15.10 \pm 1.74$ eV for the tritium instrumental resolution.

Correlations of σ with scatter peak amplitude parameters are discussed at the end of Sec. VIII C.

C. Scatter peak amplitudes $\mathcal{A}_j(p, q)$

The scatter peak amplitudes \mathcal{A}_j (Sec. IV B 3) are most reliably determined from fitting $^{83\text{m}}\text{Kr}$ calibration data. Predicting \mathcal{A}_j from simulations would require better knowledge of gas composition and inelastic scattering angle distributions (see Sec. VIF 2). As demonstrated by toy simulations, the scatter peak amplitudes follow a modified exponential $\mathcal{A}_j = \exp(-pj^{-dp+q})$ (see Sec. VIF 2). We estimate p, q for tritium data using p, q results from the two $^{83\text{m}}\text{Kr}$ quad trap fits, adjusting for the difference in mean number of tracks per event ($N_{\text{tracks}}^{\text{true}}$) between data sets. More true tracks provide more opportunities to detect an event, even after early tracks are missed—increasing the number of events in higher- j scatter peaks. Accordingly, a higher $N_{\text{tracks}}^{\text{true}}$ produces a slower decline in \mathcal{A}_j as a function of j . For each data set, $N_{\text{tracks}}^{\text{true}}$ is estimated from the observed number of tracks per event (which is smaller than the true number, due to short and low-power tracks) as described in Sec. VA.

Among data sets obtained with the same magnetic trap configuration, such as the tritium and $^{83\text{m}}\text{Kr}$ quad trap data, we expect that $N_{\text{tracks}}^{\text{true}}$ is the dominant factor causing differences in p and q . Besides $N_{\text{tracks}}^{\text{true}}$, other properties affecting missed track probabilities, such as electron pitch angle distributions, are similar among data sets with the same trap configuration. In addition, the mean track duration τ is determined to be a sub-dominant factor, since fitted p and q values appear to vary randomly with τ across data sets, suggesting that they are not strongly correlated with τ .

Results from pre- and post-tritium quad trap $^{83\text{m}}\text{Kr}$ fits define functions $p(N_{\text{tracks}}^{\text{true}})$ and $q(N_{\text{tracks}}^{\text{true}})$, which predict p and q for tritium data. We have two $^{83\text{m}}\text{Kr}$ data points available with the same trap depth and similar conditions; we perform linear extrapolations from these to p and q for the $N_{\text{tracks}}^{\text{true}}$ in tritium data. Figure 22 displays the p, q estimates and uncertainties used in this extrapolation. The uncertainty on $N_{\text{tracks}}^{\text{true}}$ is larger for tritium than for $^{83\text{m}}\text{Kr}$ data because the tritium data set has fewer events. Uncertainties are propagated via Monte Carlo sampling. For each of the three quad trap data sets, we sample $N_{\text{tracks}}^{\text{true}}$ from a normal distribution defined by its mean and uncertainty, given in Tab. II.

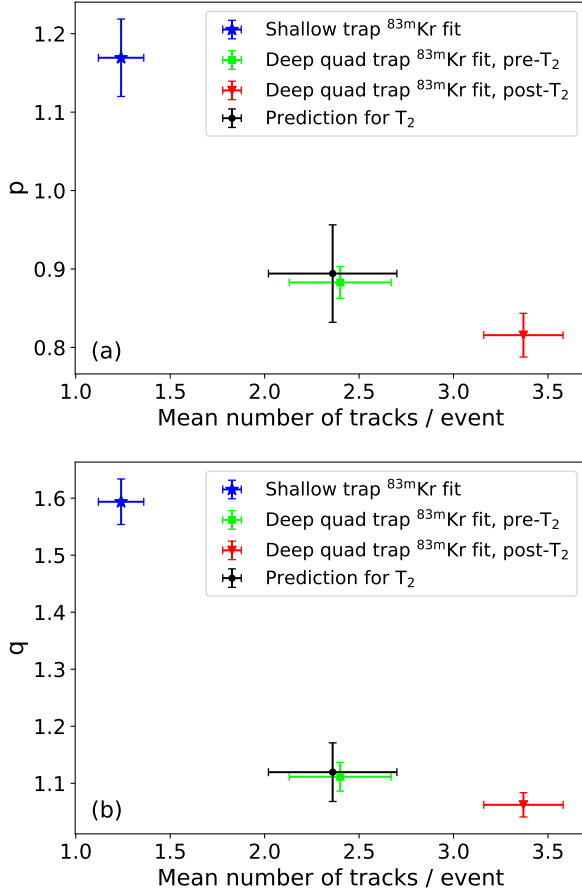


FIG. 22. Fitted scatter peak amplitude parameters (a) p and (b) q vs. mean number of tracks per event in each data set. For tritium (black dot), parameters are predicted by extrapolating deep quad trap results to the tritium data’s number of tracks per event.

For each $^{83\text{m}}\text{Kr}$ data set, we sample p and q from a bivariate normal distribution which accounts for their correlated uncertainty contributions (detailed later in this section). That set of sampled values predicts one p - q pair for tritium. By repeating the sampling process, we construct a bivariate uncertainty distribution of tritium p - q values. Means, uncertainties and a correlation are computed from this distribution and reported in the first row of Tab. V. The p , q uncertainties are larger for tritium than for $^{83\text{m}}\text{Kr}$ because of the large uncertainties in $N_{\text{tracks}}^{\text{true}}$ values, which propagate to the tritium p , q results. Note that the mean p , q values for tritium are close to the pre-tritium $^{83\text{m}}\text{Kr}$ values; this is because $N_{\text{tracks}}^{\text{true}}$ is similar for the two data sets. Best estimates for scatter peak amplitudes as a function of scatter order are shown in Fig. 23.

We include three systematic effects in the p - q bivariate uncertainty distributions for $^{83\text{m}}\text{Kr}$ quad trap data: statistical fit uncertainties, gas composition uncertainties, and resolution (\mathcal{I}) simulation uncertainties. These effects produce shifts in different directions for distinct data sets,

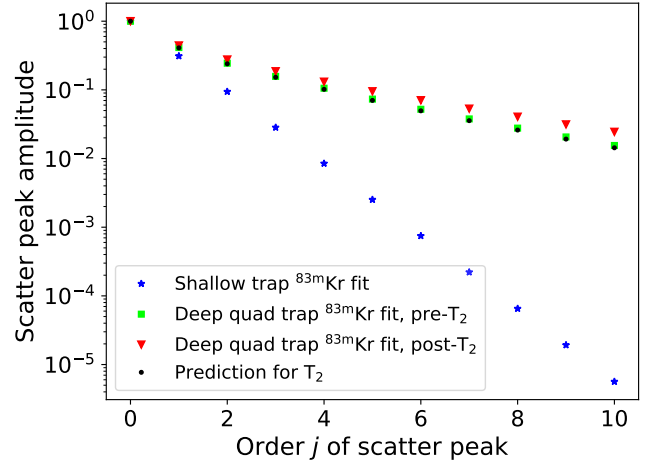


FIG. 23. Best-estimate scatter peak amplitudes \mathcal{A}_j for j missed tracks. $^{83\text{m}}\text{Kr}$ estimates are fitted from data; tritium estimates are extrapolated from $^{83\text{m}}\text{Kr}$ results.

TABLE V. Estimates and uncertainties of scatter peak amplitude parameters p and q for tritium data.

	p	q	Correlation
Best estimate	0.89	1.12	N/A
Extrapolation uncertainty	0.06	0.05	0.60
SNR _{max} uncertainty	0.09	0.01	0.56
Total uncertainty	0.11	0.05	0.38

so they may be propagated in the extrapolation using independent distributions for pre- and post-tritium $^{83\text{m}}\text{Kr}$ data. For each $^{83\text{m}}\text{Kr}$ data set, the covariance matrix for sampling p , q is the sum of three covariance matrices associated with the three systematic effects. For statistical fit uncertainties, the matrix is output by the $^{83\text{m}}\text{Kr}$ maximum likelihood fit. Gas composition uncertainties are determined as described in Sec. III C. Specifically, $^{83\text{m}}\text{Kr}$ data are re-fitted for 300 gas compositions, producing a p - q distribution from which a covariance matrix is calculated. Simulation uncertainties in \mathcal{I} are determined using the method in Sec. VIC 2, which again yields a p - q distribution and corresponding covariance matrix.

One additional effect, SNR_{max} uncertainty, is accounted for after the p - q extrapolation. This uncertainty is not propagated through the extrapolation because doing so would treat the effect as uncorrelated among data sets. In fact, mis-modeling the SNR_{max} systematically shifts p and q across data sets by altering the width of \mathcal{I} , causing p and q to compensate similarly during both quad trap $^{83\text{m}}\text{Kr}$ fits. We estimate the SNR_{max} uncertainties and correlation for tritium p , q using the method in Sec. VIC 2, with pre-tritium $^{83\text{m}}\text{Kr}$ data. Covariance matrices for the extrapolation and the SNR_{max} effect are then summed. Table V summarizes the results. We find $p = 0.89 \pm 0.11$ and $q = 1.12 \pm 0.05$, with a correlation of

0.38.

The SNR_{max} effect also causes p and q to be correlated with σ , the standard deviation of the tritium \mathcal{I} . We assume that, in the tritium analysis, the correlations of p and q with σ match correlations observed in $^{83\text{m}}\text{Kr}$ fits due to the SNR_{max} effect. Pearson correlations of p and q with σ are determined using 100 sets of (σ, p, q) values for different SNR_{max} values (see Sec. VIC 2). We find that the p - σ correlation from the SNR_{max} effect is 1.00, but the overall p - σ correlation is 0.82—accounting for the fact that the parameters’ uncertainties include other, uncorrelated contributions. The q - σ correlation from SNR_{max} is 0.60 and the overall correlation is 0.06.

D. Energy-dependent efficiency ϵ

The tritium spectrum is continuous, covering a range in frequency. The recorded spectral shape therefore depends on the variation of the event detection efficiency ϵ and the response function \mathcal{R}_{PSF} over the ROI. Mode structures and interference in the CRES cell cause a strong dependence of the received power on frequency and trap location in the cell, which affects both ϵ and \mathcal{R}_{PSF} . The measured efficiency variation with frequency in Sec. VID 1 requires a correction for energy dependence before it can be used for tritium analysis.

1. Efficiency correction for energy dependence

Determining the detection efficiency vs. frequency curve for tritium requires an additional step beyond the procedure described in Sec. VID for $^{83\text{m}}\text{Kr}$ data. This is because the field-shifted $^{83\text{m}}\text{Kr}$ data at different frequencies vary in B but are fixed at an energy of 17.8 keV, while electrons in the tritium spectrum experience the same B but have varied kinetic energies. This energy dependence leads to a difference in radiated power and therefore in detection efficiency. The power coupled to the transporting TE_{11} mode is a function of both energy and magnetic field, as derived in [20]:

$$P(f_c, E_{\text{kin}}) \propto Z_{11}(f_c) e^2 v_0^2(E_{\text{kin}}), \quad (19)$$

where Z_{11} is the TE_{11} mode impedance and v_0 is the magnitude of the electron’s velocity.

The process of correcting $\epsilon(f_c)$ for the energy-dependence of the transmitted power is depicted in Fig. 24. Since B was constant during tritium data collection and f_c and E_{kin} are linked by Eq. 2, the goal of the correction is to obtain the efficiency’s simultaneous dependence on f_c and E_{kin} which we denote $\epsilon(f_c(E_{\text{kin}}))$. The energy dependence of ϵ is added by combining information from field-shifted $^{83\text{m}}\text{Kr}$ data, simulation, and Eq. 19. The energy correction requires that a relative change of SNR leads to a predictable relative change of count rate. Because of the SNR differences between the

individual trap locations in the cell, predicting the relation between SNR and count rates is difficult in the quad-trap but can be found by summing the single-trap count rates. Hence the energy correction is done for single-trap data and the statistical weights from Sec. VID 2 are used to sum the results.

We measure the SNR of events in each trap at each frequency in the field-shifting scans relative to the SNR in trap 3 at the un-shifted background field strength. We name this relative SNR $\beta(f_c)$. In single-trap data, $\beta(f_c)$ (Fig. 25) is extracted by matching simulations to the SNR distribution in field-shifted $^{83\text{m}}\text{Kr}$ data at each frequency step in the field scans (Sec. VIID 2). Combining $\beta(f_c)$ with the relative changes of count rate vs. frequency yields the count rate vs. β (Fig. 26). With the exception of two narrow frequency ranges at around 25.828 GHz and 25.926 GHz, the relation between count rate and β is bijective and identical in each trap up to a relative scaling factor resulting from trap-depth differences. At ~ 25.828 GHz and ~ 25.926 GHz, the reconstructed event count rate is decreased by the presence of very high track slopes especially in traps 2 and 3 (see Sec. VIID 3). Excluding these frequency ranges and fitting the remaining count rate vs. SNR from all traps with a 4th-order polynomial provides a function that enables empirical prediction of a relative count rate change from a relative SNR change.

With the relation of count rate vs. SNR in hand, we perform the energy correction for each individual trap by:

- Translating relative count rates vs. frequency in each trap to relative SNR vs. frequency $\beta(f_c)$.
- Multiplying the relative SNR vs. frequency with the relative dependence of the coupled power on energy: $P(f_c, E_{\text{kin}})/P(f_c, E_{\text{kin}} = 17.83 \text{ keV})$.
- Translating the energy-corrected SNR vs. frequency $\beta(f_c(E_{\text{kin}}))$ back to relative count rates vs. frequency using the 4th-order polynomial.

After performing the energy correction in the single traps, we sum the corrected count rates using the trap weights from Sec. VID 2 to obtain energy-corrected quad-trap count rates. The resulting relative changes of the quad-trap rates with frequency directly correspond to the energy-corrected detection efficiency curve $\epsilon(f_c(E_{\text{kin}}))$, which is shown in Fig. 27(b).

Each step of the energy correction process contributes an uncertainty to ϵ . All uncertainties are propagated and amount to the width of the grey curve in Fig. 27(b). The main contributions are the statistical uncertainties from the count rates in each constituting trap and the uncertainty from interpolating the coarse field scans in traps 1 and 4 to the dense steps recorded in traps 2, 3, and the quad trap (see Sec. VID 2). Other uncertainties originate from the extraction of $\beta(f_c)$ (Sec. VIID 2) and the polynomial fit parameter uncertainties of count rates vs. β .

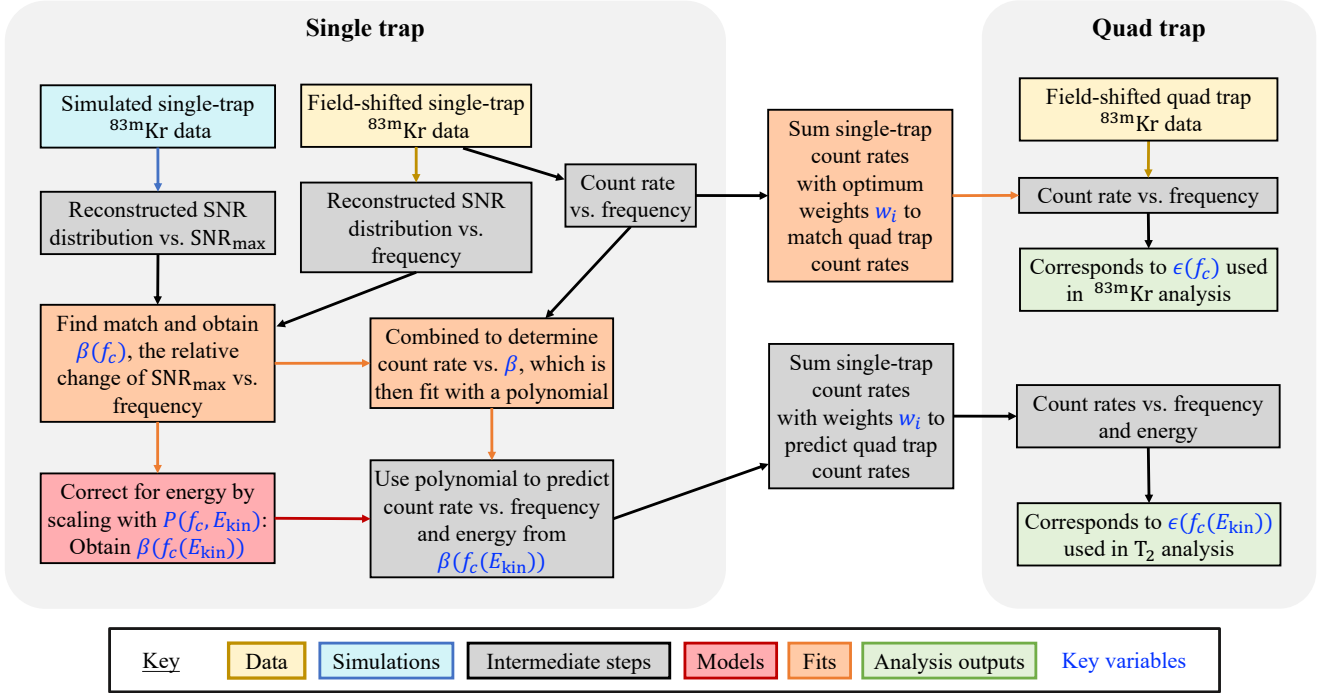


FIG. 24. Energy correction of the detection efficiency curve: Count rate dependencies on frequency are obtained from field-shifted $^{83\text{m}}\text{Kr}$ data in each single-coil trap at fixed electron energy. Matching the data to dedicated simulation sets yields $\beta(f_c)$, the relative change of SNR with frequency. From these, the count rate dependence on SNR is obtained. $\beta(f_c)$ is corrected for energy using the analytic power dependence on energy (Eq. 19) to obtain $\beta(f_c(E_{\text{kin}}))$. Combining this with the count rate vs. β yields the energy-corrected count rate vs. frequency. The energy-corrected count rates vs. frequency for single traps are summed to obtain the quad-trap rates which correspond to the quad-trap efficiency for tritium: $\epsilon(f_c(E_{\text{kin}}))$.

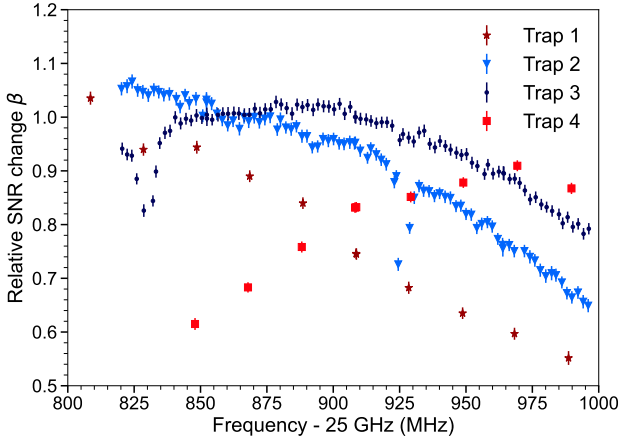


FIG. 25. Extracted relative SNR change $\beta(f_c)$ during the background field scan in each single-coil trap.

2. Extraction of the SNR dependence on frequency

The relative change of SNR $\beta(f_c)$, which is a necessary input for the energy correction, was extracted from the field-shifted $^{83\text{m}}\text{Kr}$ data by comparing the data to simulation. We simulate $^{83\text{m}}\text{Kr}$ K-line data for a single deep

trap as described in Sec. V A. From the simulation output, the coupled power from each simulated $^{83\text{m}}\text{Kr}$ event is collected for event-reconstruction processing. The trigger and offline event reconstruction process is replaced by a response matrix, mapping the true SNR of an event to a distribution of likely reconstructed SNR that integrates to the detection probability for this event. The coupled power of each event is scaled to SNR before being forward folded with the response matrix. The resulting SNR distribution is then compared to the distributions recorded in the field-shifted data for all scan steps. Prior to the comparison, the simulated and recorded data are both reduced to a frequency slice around the peak center of ± 1 MHz. The process of scaling the power to SNR, mapping it to a detected SNR distribution, and comparing it to the recorded data is repeated in a χ^2 minimization with the power-to-SNR scaling factor as the only free parameter. $\beta(f_c)$ is calculated by dividing the power-to-SNR scaling factors by the factor for $\Delta B_{\text{FSS}} = 0$ in trap 3. The results are shown in Fig. 25. The similarity to Fig. 16 (count rate vs. frequency from data) gives rise to the direct relation between count rates and β in Fig. 26. Note that the lowest frequency point at which $\beta(f_c)$ could be extracted from fits in trap 4 is ≈ 25.85 GHz. At the two scan points below this frequency, the limited statistical power of this trap prevented a successful SNR analysis.

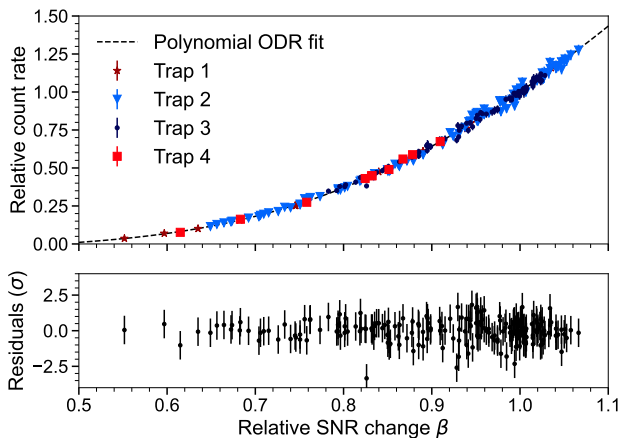


FIG. 26. Measured relative count rate vs. extracted relative SNR change during background field scans. The data points originating from ~ 25.828 GHz and ~ 25.926 GHz (where slopes in trap 2 and 3 are highest) are excluded from this plot. The count rates in each trap are scaled relative to trap 3 to minimize the orthogonal distance to a common 4th-order polynomial fit. The orthogonal distance regression (ODR) takes the x and y uncertainties into account.

sis. As a result, the energy-corrected detection efficiency in the quad trap $\epsilon(f_c(E_{\text{kin}}))$ is limited to $f_c \gtrsim 25.85$ GHz (Fig. 27(b)).

3. Efficiency correction for slope variation

In Fig. 27(a), it can be seen that the average track slope in the field-shifted data varies strongly across the scanned frequency range. The high-slope regions occur at frequencies where there is enhanced coupling of the electrons to trapped resonant modes as described in Sec. II C. The largest effects are caused by the TM_{01} mode, which is trapped at the upper end by the quarter-wave plate and at the lower end by the terminator (which were designed to match the mode impedance of TE_{11} , not TM_{01}). Other, weaker resonances arise from reflections at the windows, coupling flanges, gas connection, etc.

The detection efficiency mostly depends on frequency and trap location in the waveguide. However, the event reconstruction has a small track-slope dependence, too. Over a large range of slopes ($\Delta s \lesssim 300$ MHz/s), this is simply due to the fact that the electron tracks with larger slopes cross more frequency bins per time and hence the power in a single time-frequency bin is reduced. The SNR-scaling analysis of the field-shifted data incorporates this effect by returning a decreased optimum β in frequency regions of high slopes.

The largest slopes within the tritium analysis frequency range are found at ~ 25.926 GHz in trap 2. Here the reconstruction algorithm sometimes misses or breaks tracks and the reconstruction efficiency is reduced.

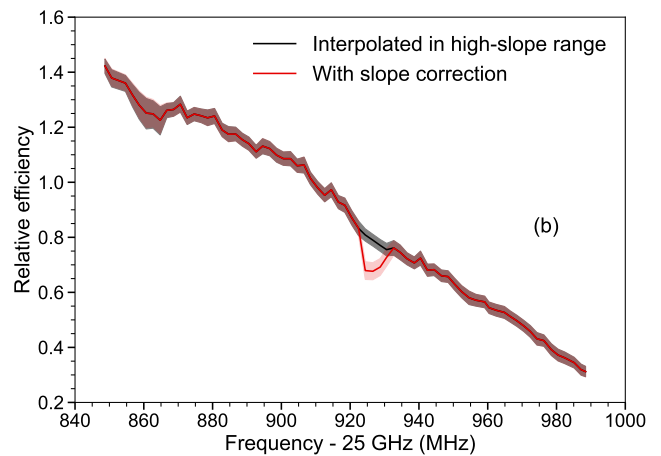
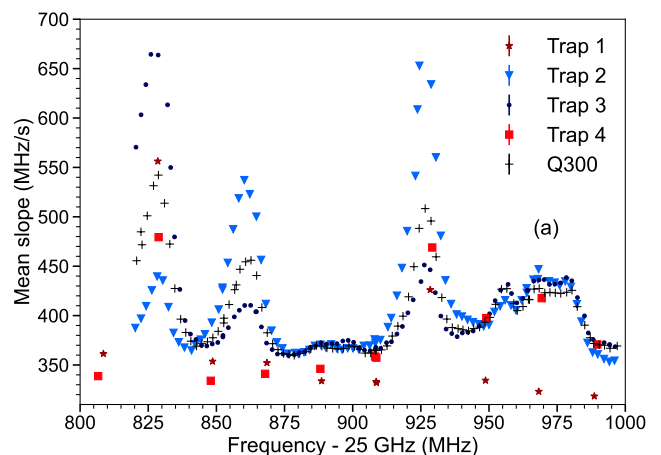


FIG. 27. (a) Mean recorded first track slope in events that start within ± 1 MHz of the fitted $^{83\text{m}}\text{Kr}$ peak position. (b) Relative detection efficiency predicted for tritium $\epsilon(f_c(E_{\text{kin}}))$. The tritium efficiency is given relative to the efficiency for $^{83\text{m}}\text{Kr}$ K-line events. As an intermediate step in the construction of $\epsilon(f_c(E_{\text{kin}}))$, the high-slope region at 25.926 GHz was excluded from the correction for energy dependence and the efficiency was linearly interpolated in this range (black). The correction for slope variation assumes that the relative decrease of detection efficiency is independent of the kinetic energy which results in the red curve. The slope peak at 25.828 GHz lies outside the calibrated efficiency range and the range covered by the tritium spectrum.

Therefore, we exclude this frequency region from the count rate vs. β correlation (Figure 26), and thus also from the efficiency correction for energy dependence. Instead, we linearly interpolate ϵ for this frequency range which results in the black efficiency curve in Fig. 27(b). The slope peak at ~ 25.828 MHz is below the efficiency analysis range. The smaller peak at around ~ 25.86 GHz is close to the expected tritium endpoint location but the event reconstruction quality is not further diminished by the increased slopes in this region.

To re-introduce the efficiency deficiency that is ob-

served in the field-shifted data at ~ 25.926 GHz, we multiply the interpolated $\epsilon(f_c(E_{\text{kin}}))$ by the relative efficiency decrease in this region. The uncertainty on $\epsilon(f_c(E_{\text{kin}}))$ increases in this process, since the multiplied ratio comes with an uncertainty that is added in quadrature to the uncertainty from interpolation. The result is shown in red in Fig. 27(b).

4. Efficiency binning

The interpolation of the measured count rates in each trap makes it possible to calculate a relative efficiency value at any frequency over the calibrated range covered by the field-shifted $^{83\text{m}}\text{Kr}$ data. The correction for energy dependence in Sec. VIII D 1 produces an efficiency curve that applies for any energy corresponding to a frequency at which the field-shifted $^{83\text{m}}\text{Kr}$ data had sufficient statistical power to perform the energy correction. This limits the energy range over which the tritium data can be modeled to 16.2–19.0 keV. However, for the background-only energy range above the tritium endpoint, $\epsilon(f_c(E_{\text{kin}}))$ is not used because the background is modeled as energy-independent.

We perform a binned tritium analysis with bin widths of approximately 2.5 MHz or 50 eV. We integrate the quasi-continuous efficiency $\epsilon(f_c(E_{\text{kin}}))$ over the tritium-analysis bins to obtain ϵ_k for each bin k .

E. Frequency dependence of energy response function \mathcal{R}_{PSF}

In $^{83\text{m}}\text{Kr}$ data analysis, the response function \mathcal{R}_{PSF} is optimized to fit the K-line at its singular frequency position. The instrumental resolution \mathcal{I} is matched to the SNR of each $^{83\text{m}}\text{Kr}$ data set (Sec. VI C 1), and p and q , which determine the scatter peak amplitudes A_j , are free in the fits (Sec. VI F). In the tritium data analysis, we use the extracted SNR_{max} from the pre-tritium $^{83\text{m}}\text{Kr}$ data, since these two data sets are most similar in average event properties (Tab. II). However, we know from Sec. VIII D 1 that the SNR varies with frequency and depends on energy, so we can expect that \mathcal{I} changes over the frequency and energy ROI. We also expect the shape of the scattering tail to vary with frequency, since the event reconstruction is impacted, for example, by power coupling changes in the waveguide that manifest in the track slope changes observed in the field-shifted data.

To obtain the variation in the shape of \mathcal{R}_{PSF} , we fit the K-line in the field-shifted $^{83\text{m}}\text{Kr}$ data at each magnetic field step. For each frequency position, a simulated instrumental resolution $\mathcal{I}(f_c)$ is created by scaling the optimum SNR_{max} for the reference field-shifted data from $\Delta B = 0$ mT by the relative SNR change $\beta(f_c)$ extracted in Sec. VIII D 2. The resulting instrumental resolution serves as input to the lineshape fits in which p and q are left free to obtain their variation with frequency. The re-

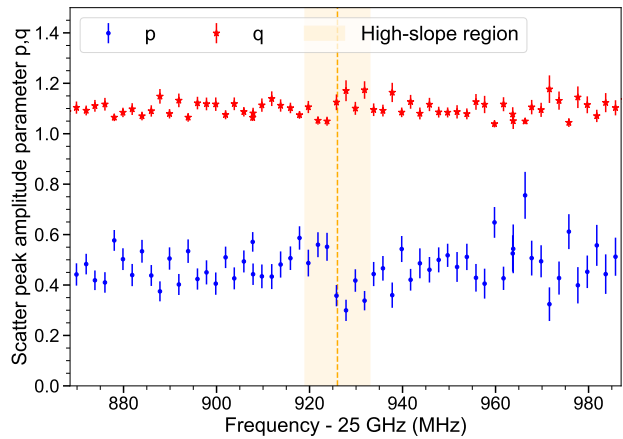


FIG. 28. The field-shifted quad trap data is analyzed at each magnetic field step with the $^{83\text{m}}\text{Kr}$ lineshape model. A separate simulated resolution shape was produced in simulations for each step and the response function parameters p and q were extracted from fits. The p and q fit results over the tritium analysis ROI are shown. The vertical yellow band indicates the high-slope frequency range at ~ 26.926 GHz.

sult is shown in Fig. 28. We verify that the relative variation with frequency is not significantly affected by the gas composition by repeating all fits for the maximum and minimum allowed helium contribution to inelastic scattering.

The variation of p with frequency is much larger than that of q . Monte Carlo studies of tritium data with varying p and q have shown that the shape of \mathcal{R}_{PSF} and its impact on the tritium analysis results are more sensitive to changes of q than they are to changes of p . It is therefore unsurprising that the $^{83\text{m}}\text{Kr}$ fits constrain q more tightly than p .

Note that the mean p and q seen in Fig. 28 are different from their values under tritium conditions due to the differences in gas composition and system noise temperature. However, we expect the tail shape to vary similarly with frequency in the tritium data. By dividing the $p(f_c)$ and $q(f_c)$ values in Fig. 28 by their means, we obtain scale factors $s_p(f_c)$ and $s_q(f_c)$. For the tritium analysis, these scale factors multiply the tritium p and q from Sec. VIII C.

The expected variation of \mathcal{I} with frequency in the tritium data is obtained similarly to the calculation of $\mathcal{I}(f_c)$ described above. However, the dependence on energy of the efficiency variation $\epsilon(f_c(E_{\text{kin}}))$ has to be accounted for. We therefore scale the optimum SNR_{max} for tritium (identical to the SNR_{max} of the pre-tritium $^{83\text{m}}\text{Kr}$ data) by $\beta(f_c(E_{\text{kin}}))$ obtained in the energy correction described in Sec. VIII D 1. This allows us to generate the expected $\mathcal{I}(f_c(E_{\text{kin}}))$ at each frequency in the tritium ROI. From these distributions, we calculate width scale factors $s_\sigma(f_c(E_{\text{kin}}))$, which multiply σ , the resolution standard deviation from Sec. VIII B.

The estimate ranges of s_p , s_q , and s_σ are given in Tab. VII. The impact of the frequency and energy variation of \mathcal{R}_{PSF} on the tritium analysis is discussed in Sec. IX B.

F. Summary of parameter probability distributions

Parameter estimates and uncertainties are summarized in Tab. VI and Tab. VII. Statistical uncertainties contribute more to the endpoint interval than the systematic uncertainties combined. When propagating systematic uncertainties to the endpoint and neutrino mass, we use normal distributions to describe the uncertainties on all parameters in Tab. VI. For the energy response (\mathcal{R}_{PSF}) parameters p , q and σ , a multivariate normal distribution is used to account for correlations. Physical parameter bounds (e.g., $\sigma > 0$) are enforced during fits to tritium data. While normal distributions do not permit such bounds, the distributions are all localized sufficiently far from bounds, as verified by MC studies (see Sec. IX B).

TABLE VI. Estimates with uncertainties for parameters in the model of tritium data, derived from $^{83\text{m}}\text{Kr}$ calibration data and simulations.

Parameter	Estimate
H ₂ inelastic scatter fraction γ_{H_2}	0.91(05)
Mean magnetic field B	0.9578099(13) T
Instrumental resolution σ	15(2) eV
Scatter peak amplitudes: p	0.89(11)
Scatter peak amplitudes: q	1.12(05)
Statistical power	3770 events after cuts

TABLE VII. Size and uncertainty of variation of ϵ , σ , p , and q with f_c in the tritium model, derived from $^{83\text{m}}\text{Kr}$ calibration data and simulations. The uncertainty on s_σ does not affect tritium analysis results and was therefore omitted.

f_c -dependent parameter scaling	Estimate (min–max)	Uncertainty (min–max)
ϵ	0.31–1.42	0.02–0.05
s_σ	0.87–1.07	not included
s_p	0.59–1.53	0.07–0.21
s_q	0.95–1.10	0.01–0.06

IX. TRITIUM DATA ANALYSIS

A. Tritium analysis procedures

We perform Bayesian and frequentist analyses of the tritium data to measure the spectral endpoint E_0 and

place a limit on the neutrino mass m_β . The analyses are not blind, but they are validated using MC studies as discussed in Sec. IX B.

1. Bayesian analysis procedure

The likelihood function used for Bayesian inference is the Poisson likelihood for the number of counts per bin according to the tritium model (Eq. 18), multiplied by prior distributions for all parameters. For bin k , the Poisson rate is $(dN/dE_{\text{kin}})_{k}^{\text{ctr}} \cdot \Delta E_{\text{kin},k}$: the tritium model at bin center multiplied by the bin width.⁴ The bins have a fixed width in frequency, so in energy their widths vary slightly across the ROI.

We evaluate the likelihood function using the Stan statistical software platform, which performs Bayesian inference via the Hamiltonian Monte Carlo algorithm [38, 57]. This produces numerical posterior distributions for E_0 and m_β , marginalized over nuisance parameters. It is valuable to directly fit m_β (instead of the unbounded variable m_β^2 used in frequentist analyses) because the beta spectrum’s Heaviside theta factor (Eq. 14) depends on m_β , without any exponents [7, 15]. Several Stan convergence diagnostics validate the algorithm’s performance for our model [55, 58]. For E_0 , we report the posterior mean and the 1σ quantile credible interval [5]. The 1σ highest posterior density (HPD) interval is consistent within < 0.5 eV. For the neutrino mass, we report a 90% credible limit [5].

Uncertainties are propagated by incorporating them into prior distributions. The uncertainty distributions described in Sec. VIII F become normal priors in the model (or multi-normal for σ , p , and q , the resolution and scatter peak parameters). The MCMC algorithm explores the probability space defined by the priors and the tritium model, propagating prior standard deviations (i.e., uncertainties) to the E_0 and m_β posteriors [5].

Bayesian inference requires a choice of prior for every parameter, not only those with measured uncertainties. Thus, the Bayesian model includes priors on the background rate r_f , as well as E_0 and m_β . For r_f , before analysis, prior knowledge constrained likely background rates within several orders of magnitude. This can be modeled with a lognormal prior (which also has the correct bound $r_f > 0$). The prior’s median is chosen to be 0.0006 events/keV/day, the target 90% C.L. used to tune event power cuts. To conservatively scale the prior width, we use the soft upper bound $r_f^{\text{max}} \approx 0.2006$ events/keV/day, the 50% C.L. from observing no events in ≈ 0.5 keV above the endpoint during an early 7-day data set taken to test the apparatus setup. The prior’s standard deviation is set equal to

⁴ Test fits with piecewise integration of the probability density in each bin (10 steps per bin) produced consistent results.

[0.2006–0.0006] events/keV/day, determining the lognormal prior shape.

Separate fits are performed to measure E_0 and place a limit on m_β . When measuring E_0 , m_β should be constrained to its known range, near zero. Otherwise, the E_0 posterior is biased upward due to the large m_β probability density above the true value—with little density below, since we require $m_\beta > 0$. By contrast, when placing a limit on m_β , a broad E_0 prior may be employed, since there is no bound in the E_0 prior which introduces an asymmetry.

For the E_0 fit, the m_β prior is a gamma distribution constructed so that 5% of its probability mass falls below 0.0085 eV (from mass splitting uncertainties [5]) and 10% falls above 0.8 eV (KATRIN’s 90% C.L. [8]). A gamma prior is appropriate because of its lower bound at zero, and because it can take on a wide range of shapes depending on the external conditions provided, making it a generic prior choice for positive parameters. Other positive priors tend to effectively rule out either high values of m_β or a region near $m_\beta = 0$ [59, 60]. We use a weakly-informative normal prior on E_0 with a standard deviation of 300 eV.⁵ MC-spectrum tests confirm that the E_0 result is robust to the specific choice of prior: when we analyze MC data, the E_0 posterior interval width remains constant as the prior standard deviation is scanned from 100 to 400 eV, within < 1 eV computational uncertainty. That uncertainty is calculated by re-analyzing the same MC spectrum 25 times and computing the standard deviation of resulting interval widths.

For the m_β fit, we use the same normal E_0 prior, and for the m_β prior we use a uniform distribution multiplied by an error function with $\mu_{\text{erf}} = 1$ keV and $\sigma_{\text{erf}} = 0.2$ keV. The m_β prior for this fit reflects assumptions made before data-taking: if $m_\beta \gtrsim 1$ keV, the apparatus’s frequency bandwidth would be too small, as this would shift $\gtrsim 2/3$ of the events out of the ROI. On the lower edge, another error function tapers the prior at 0.0085 eV ($\sigma_{\text{erf}} = [1/3$ of that value]). MC tests demonstrate that this prior is weakly informative: when we increase/decrease the high-energy error function’s parameters by $\approx 50\%$, the m_β limit is unaffected.

Frequency data are histogrammed in 71 bins, each about 50 eV in width. An analytic calculation (described in Sec. XC) indicates that a bin width near 50 eV is expected to minimize the neutrino mass uncertainty. When we instead use 65 bins (≈ 55 eV in width), the Bayesian 90% credible limit on m_β increases by 5 eV.

2. Frequentist analysis procedure

The frequentist analysis uses the tritium model of Eq. 14. There are small differences from the Bayesian

analysis model described in Sec. VII. Most notably, the analysis uses m_β^2 instead of m_β as the mass fit parameter and does not limit m_β^2 to be positive. This allows the fit parameter to range on either side of zero to allow for statistical fluctuations near the endpoint. A functional form should be chosen that yields parabolic likelihood profiles. We tried two forms for $m_\beta^2 < 0$, the Mainz implementation [63]:

$$\left[\epsilon + 0.66k \exp\left(-1 - \frac{\epsilon}{0.66k}\right) \right] \sqrt{\epsilon^2 + k^2} \cdot \Theta(\epsilon + 0.66k), \quad (20)$$

and the Livermore implementation [7]:

$$|\epsilon^2 + \frac{k^2\epsilon}{2|\epsilon|}| \Theta(\epsilon + k), \quad (21)$$

with $k^2 = -m_\beta^2$. These functions replace the phase-space factor $\epsilon[\epsilon^2 - m_\beta^2]^{1/2}\Theta(\epsilon - m_\beta)$ of Eq. 14 for $m_\beta^2 < 0$. They bracket the desired parabolic behavior, the Mainz version likelihood decreasing too slowly below 0, and the Livermore version likelihood decreasing too quickly. In the Feldman-Cousins construction used to find an upper limit on the mass with our data, these functions give the same result and refinements were not pursued.

The frequentist analysis uses uniform 50-eV-wide energy bins and employs extended binned maximum likelihood fits, assuming that the number of events in each bin are Poisson distributed with an expectation value given by the numerical integral of the tritium spectrum (Eq. 18) over each bin. For minimizing the log likelihood we use the MIGRAD algorithm from the Minuit2 library [64, 65].

All systematic parameter uncertainties listed in Tab. VI are modeled as Gaussian. For the H_2 inelastic scatter fraction γ_{H_2} and σ , the uncertainties are propagated by adding normal constraints to the log-likelihood function. A multivariate normal constraint is added for σ , p and q . Only the magnetic field and detection efficiency are not included as floating model parameters. Instead, they are propagated by MC sampling. Hard lower limits of 0 are imposed for the number of background and signal events, the resolution, and for the bin efficiencies.

The endpoint E_0 and m_β^2 are measured in separate analyses. For the endpoint measurement, m_β^2 is fixed at zero. For determining a limit on m_β^2 , both parameters are free. The analysis proceeds in 3 steps. In the first step, the data is fit with a model in which γ_{H_2} , p , q , and σ are constrained nuisance parameters and the signal rate r_s , the false event rate r_f , and E_0 (and m_β^2) are free. The magnetic field and the detection efficiency in each bin are fixed to their calibrated best values. Uncertainty intervals on E_0 (and m_β^2) are extracted by the MINOS profile method [66]. This way, the uncertainties of γ_{H_2} , p , q , and σ are propagated to the interval widths of E_0 (and m_β^2). In the next step, γ_{H_2} , p , q , and σ are fixed to the best-fit values while the magnetic field and

⁵ We follow established conventions regarding weakly-informative and ‘non-informative’ priors, see [59–62].

efficiency uncertainties are propagated by MC sampling. An Asimov data set [67] from the first-pass best-fit model is generated and then repeatedly analyzed with a model that uses a sampled magnetic field value B_j and efficiency values $\epsilon_{j,i}$, for energy bin i . This produces a distribution of fit results for E_0 (and m_β^2). The difference between the borders of the highest-density intervals and the best-fit values are added in quadrature to the profile interval widths from the first-pass analysis. In the third analysis step, the frequency variation of p and q is propagated (see Sec. IX A 3).

The Feldman-Cousins construction [68, 69] is used to translate the best-fit point of actual data to a 90% C.L. upper limit on m_β^2 , and consequently on m_β . For a range of true masses, pseudo experiments are conducted and the measured m_β^2 values are included in an interval following the likelihood-ratio ordering rule. Since systematic parameters are sampled in the generation of pseudo data, their uncertainties are included in these intervals. We find that the ordering process is impacted by a small number of pseudo experiments with higher than usual likelihood-ratio for a given fitted mass which results in over-coverage of the obtained limits. We determined these outliers to be primarily caused by the proximity of the false event rate r_f to the hard limit of 0, which is implemented in Minuit by a non-linear variable transformation. To address these outliers, we take the median of the likelihood-ratio over small ranges of fitted m_β^2 from pseudo experiments for each simulated true mass and find the likelihood-ratio level above which 90% of experiments are contained.

3. Frequency variation of scatter peak amplitudes

The tritium analysis model does not include the frequency variation of \mathcal{R}_{PSF} , controlled by parameters σ , p and q . In both frequentist and Bayesian analyses, the σ variation was found not to affect the reported results, but the p and q variation does have an effect. This variation is captured by the scale factors $s_p(f_c)$ and $s_q(f_c)$, as described in Sec. VIII E.

In the frequentist case, pseudo experiments revealed that a neglected frequency dependence of p and q shifts the endpoint result by $-1.03(90)$ eV on average. No bias was found for m_β^2 . We therefore include an uncertainty of E_0 and m_β^2 and a correction of E_0 resulting from ignoring this dependence in the frequentist analysis. For any given analysis (of pseudo data or real data), this is done by generating many Asimov data sets from the initial best-fit model modified with a randomized frequency-dependent scaling of p and q by $s_p(f_c)$ and $s_q(f_c)$ and analyzing them with the model that does not have a frequency dependence included. The average shift of the E_0 fit result is subtracted from the original fit result and the standard deviations of E_0 and m_β^2 are added in quadrature to the uncertainties of the experiment's final results. For the m_β limit construction with the Feldman-Cousins method,

$s_p(f_c)$ and $s_q(f_c)$ are sampled within uncertainties during the pseudo-data generation and hence propagated to the distribution of m_β^2 fit results and the confidence limit.

In the Bayesian analysis, MC studies show that neglecting the frequency dependence of the scatter peak amplitudes shifts the endpoint posteriors by $-3.1(12)$ eV on average. We correct for this shift by adding 3.1 eV to the calculated E_0 posterior mean. As in the frequentist case, the s_p and s_q values inputted to the MC data generator for each frequency region are sampled from distributions to account for uncertainty in the frequency variation. That sampling produces a fluctuation in the endpoint results, corresponding to an uncertainty of $[+4.1, -4.3]$ eV. This contribution is added in quadrature to the 1σ E_0 bounds from the fit to data, increasing the bounds by 0.5 eV. For m_β , MC studies show that neglecting the frequency variation of p and q reduces the coverage of 90% credible limits by 3%. To correct for this effect, MC 90% C.L.s must increase by 8 eV. This correction is added to the m_β limit result.

B. Monte Carlo studies

The Bayesian and frequentist analyses are both validated with Monte Carlo (MC) studies. Random samples of tritium decay pseudo-data are generated and fitted by the tritium model (the same model is used to fit experimental data). For ensembles of MC spectra, we confirm that E_0 and m_β (m_β^2 in the frequentist analysis) intervals have no under-coverage, and that E_0 best-fit values do not exhibit large biases (Sec. IX B 2). We follow the procedure in [15] for MC studies.

1. Generation of pseudo data

When generating data, electron energies are sampled and converted to cyclotron frequencies before binning events. The data generation model is highly detailed, to verify that analysis model approximations have a negligible effect on the spectral endpoint E_0 and neutrino mass m_β results. In the generation model, the beta spectrum is numerically convolved with the energy point-spread function \mathcal{R}_{PSF} . The result is multiplied by an efficiency function and added to a flat background. We use the beta spectrum formula in [70], which includes a relativistic Fermi function with several atomic physics corrections. The generation model includes the theoretical molecular final state spectrum from [12] down to a binding energy of -2288 eV. The \mathcal{R}_{PSF} model includes simulated, tritium-specific instrumental resolutions for the four magnetic traps in the deep quad trap (see Sec. VI C).

Before generating each MC spectrum, the simulated resolutions are combined according to measured statistical contributions from each trap. The resulting resolution histogram is numerically convolved with inelastic scatter spectra to form broadened scatter peaks. The

convolutions account for cases when the same electron successively scatters off different gases (neglected in the analysis model). In addition, CO scattering ($\approx 1\%$ of scatters) is included during generation but not analysis. Twenty scatter peaks are generated; however, we performed a separate test to confirm that including higher-order peaks does not alter results.

Before generating each spectrum, inputs to the generator are sampled from their uncertainty distributions. This ensures that the ensemble of spectra reflects the relative likelihoods of outcomes, validating inferences [15, 71]. The background rate is sampled from the prior distribution in Sec. IX A 1. The mean field B is sampled from the distribution in Tab. VI. The efficiency vs. frequency curve is translated to energy using the configured magnetic field strength before being randomized within its uncertainty. Other parameters are sampled from distributions similar to those in Tab. VI, with minor differences to avoid making simplifications. Instead of sampling σ (which is not present in the detailed generation model), we separately sample each contribution to the uncertainty on the instrumental resolution \mathcal{I} as follows. First, counts in each bin are sampled to account for Poisson and efficiency matrix uncertainties. Second, trap weights are sampled from normal distributions before combining resolutions for the four traps. Third, the maximum SNR (SNR_{max}) uncertainty is included by introducing a factor s which scales the width of the simulated \mathcal{I} , sampling s from a normal distribution.

Another difference from Sec. VIII F is that inelastic scatter fractions for H_2 , ${}^3\text{He}$ and CO are sampled from normal distributions defined by the means and uncertainties in Tab. III. This sampling is repeated until the sum of fractions is within $[0.99, 1.01]$, then fractions are normalized to make the sum exactly 1. In addition, we account for a covariance between the ${}^3\text{He}$ fraction (or equivalently, the H_2 fraction) and the gas composition contribution to scatter peak amplitude uncertainties. To do this, we sample the scattering parameters p and q from a bivariate normal distribution excluding gas composition uncertainty, then shift p and q based on the sampled ${}^3\text{He}$ fraction, using pre-tritium ${}^{83\text{m}}\text{Kr}$ fit results to estimate the expected shift.

MC studies are performed both with and without frequency variation of \mathcal{R}_{PSF} in the data generation model (see Sec. IX A 3). Three parameters are varied as a function of frequency: p , q , and σ . This is done by convolving a different \mathcal{R}_{PSF} with the beta spectrum for each frequency step in the field-shifted data, then concatenating the resulting partial-spectra. At each step, the scale factors $s_p(f_c)$ and $s_q(f_c)$ are sampled from normal distributions that account for frequency-variation uncertainties, then multiplied by p and q (see Sec. VIII E). Uncertainties on $s_\sigma(f_c(E_{\text{kin}}))$ are negligible in comparison and are neglected.

TABLE VIII. Interval coverage (covg.) and best-fit bias from analyzing ensembles of Monte Carlo tritium data sets. The Bayesian m_β coverage is computed for trials with MC true $m_\beta > 200$ eV, as the limit coverage approaches 100% for small masses.

	E_0 1σ covg.	E_0 best-fit bias	m_β 90% C.L. covg.
Bayesian	$68 \pm 2\%$	-2.9 ± 0.8 eV	$90 \pm 2\%$
Frequentist	$69 \pm 2\%$	-2.5 ± 0.7 eV	$90 \pm 1\%$

2. Coverage and bias tests

For E_0 fit MC studies, “true” m_β values inputted to the generator are sampled from the narrow prior described in Sec. IX A 1 (defined by the KATRIN limit). For m_β limit MC studies, m_β values are sampled from a uniform distribution over $[0, 300]$ eV, to observe how the model performs across a large range of “true” values. For both studies, E_0 values are sampled from a normal distribution with $\sigma = 0.07$ eV (see Sec. IX A 1).

MC study results are summarized in Tab. VIII. In the Bayesian case, the values are taken from an MC study with no frequency variation of \mathcal{R}_{PSF} in the data generator or analysis models. The values for the case with frequency variation were corrected to achieve the same coverage and bias, as explained in Sec. IX A 3. In the frequentist case, the numbers in the table are taken from an MC study with frequency variation in the data generator; for each spectrum, intervals and best-fits are corrected

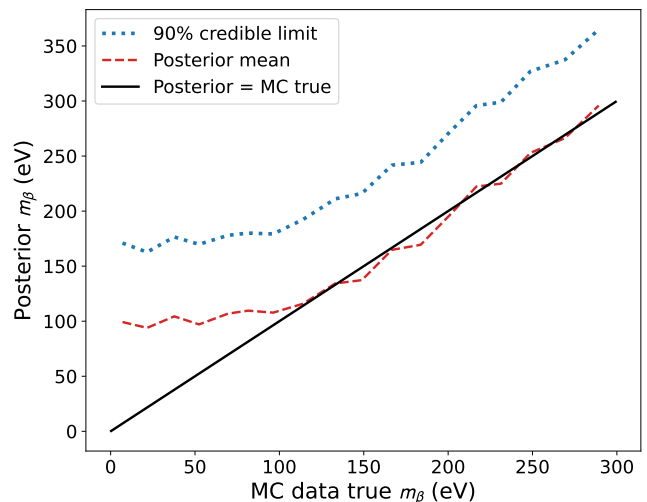


FIG. 29. Neutrino mass credible limits and posterior means from Bayesian Monte Carlo studies. As expected, m_β is overestimated for low MC true m_β . Credible limits in this region are still robust. For high true m_β , posterior means approach the expectation (solid black line) and limit coverages approach the credibility (90%). In this plot, results are averaged over ~ 20 eV regions with 33 points per region.

for this frequency variation using the Asimov sampling method described in Sec. IX A 3. Accordingly, for both Bayesian and frequentist analyses, Tab. VIII reflects the expected coverage and bias numbers for E_0 and m_β results that include corrections for the effect of \mathcal{R}_{PSF} varying with frequency.

We observe no under-coverage of E_0 1σ intervals. E_0 best-fit values have a small negative bias. For comparison, when different “best-fit” statistics (e.g. median and mode) are chosen to summarize the Bayesian E_0 posterior distributions, the average best-fit values change by a similar amount to the biases in Tab. VIII.

For the neutrino mass, the Bayesian coverage of 90% credible limits is 93.8(7)% for “true” values of $m_\beta \in [0, 300]$ eV. As expected, this coverage is inflated by trials with true $m_\beta \sim 0$ eV, for which credible limits necessarily include $\approx 100\%$ of true values. This effect may be seen in Fig. 29, showing the credible upper limits on m_β as a function of the true m_β . When we consider only trials with true $m_\beta > 200$ eV, which are negligibly affected by the physical bound at 0, the 90% limit coverage drops to 89.4(17)%.⁶ For 1σ intervals on m_β (like the one reported for tritium data in Tab. IX), the coverage is 68.4(14)%, including all trials in the MC study. Moreover, as expected, the bias in the m_β posterior mean approaches zero for high values of the MC true m_β .

The frequentist analysis is not limited to $m_\beta^2 > 0$ and gives no over-coverage for 90% confidence limits even for small m_β^2 . Neither Eq. 20 nor Eq. 21 yields a parabolic m_β^2 likelihood profile, but since our best-fit value for m_β^2 is greater than zero, the upper limit in the Feldman-Cousins construction is independent of these descriptions. The coverage of the 90% confidence limits is found to be 89.6(10)%. These results validate the model of tritium data used here, as well as the Bayesian and frequentist analysis procedures.

TABLE IX. Best-fit values with 1σ uncertainties for the tritium endpoint and neutrino mass or mass squared, and 90% credible/confidence limits on the neutrino mass. The literature endpoint value is 18574 eV [72, 73]. The reported Bayesian m_β result is a posterior median with 1σ quantiles.

	Bayesian	Frequentist	Unit
Endpoint	18553 ⁺¹⁸ ₋₁₉	18548 ⁺¹⁹ ₋₁₉	eV
m_β	57 ⁺⁶¹ ₋₃₉		eV
m_β^2		2440 ⁺¹⁰¹⁷⁵ ₋₁₃₃₅₄	eV ²
90% C.L.	$m_\beta < 155$	$m_\beta < 152$	eV

⁶ In analogy with frequentist coverage, we may also consider the coverage for trials with posterior medians near the best-estimate obtained for real data (57 eV—see Sec. X A). For MC trials with m_β medians within 5 eV of the result from data, the 90% limit coverage is 91.3(34)%.

TABLE X. Endpoint uncertainty $\sigma(E_0)$ in the frequentist analysis resulting from systematic effects and statistical precision. Here, individual uncertainties are propagated by sampling each parameter from a PDF and fitting the data with a maximum likelihood fit. The total systematic uncertainty including correlations is 2 eV smaller than adding individual systematic contributions in quadrature.

Effect	Parameters	$\sigma(E_0)$ (eV)
Systematic w/ correlations		+9, -9
Systematic quad. sum		+11, -11
Mean magnetic field	B	+4, -4
Instr. resolution std.	σ	+4, -4
Scattering energy loss	$\gamma_{\text{H}_2}, \mathcal{A}(p, q)$	+6, -6
Bin signal efficiencies	ϵ_k	+4, -4
Frequency dependence	s_σ, s_p, s_q vs. f_c	+6, -6
Statistical		+17, -17

X. RESULTS AND CONCLUSIONS

A. Final results for tritium endpoint and neutrino mass limit

Table IX displays the tritium analysis results for E_0 , m_β or m_β^2 , and 90% confidence/credible limits on m_β . Bayesian and frequentist results are similar to one another. In particular, we report a neutrino mass limit of 155 eV (152 eV) from the Bayesian (frequentist) analysis. In addition, the Bayesian (frequentist) E_0 results differ by 1.2σ (1.3σ) from the literature value. The Bayesian 1σ quantile bounds on m_β do not contain zero because all of the posterior probability mass is above zero, since m_β is a physical mass parameter. For m_β^2 in the frequentist analysis, negative values are permitted, and the 1σ bounds on m_β^2 are consistent with zero.

Table X reports frequentist systematic and statistical contributions to the total uncertainty on E_0 . The systematic contributions result from the uncertainties on tritium model parameters, summarized previously in Tab. VI and Tab. VII. The statistical uncertainty on E_0 (± 17 eV) dominates over systematics (± 9 eV), though the latter has a small effect on the total E_0 uncertainty (± 19 eV in the frequentist case). All systematic contributions are of a similar size. For m_β , the statistical uncertainty also dominates, as discussed further in Sec. X C.

In Fig. 30, the measured tritium spectrum is shown with both Bayesian and frequentist best-fit curves, which agree well. The visible best-fit model differences result from the different treatment of detection efficiency vs. energy. In the frequentist analysis, the best-fit bin-efficiencies ϵ_k are equal to the values extracted from the field-shifted ^{83m}Kr data. In the Bayesian analysis, ϵ_k are fitted from the tritium data while constrained by priors that account for uncertainties (like all other nuisance parameters). Accordingly, the Bayesian best-fit efficiency

for each bin is the mean of the ϵ_k posterior. For most bins, the efficiency posteriors are similar to the priors, due to the limited statistical power of tritium data. The exception is the low-energy bins in Fig. 30, where the tritium data pulls the ϵ_k distributions away from the best estimates from field-shifted $^{83\text{m}}\text{Kr}$ data.

The frequentist confidence intervals for the endpoint E_0 and neutrino mass squared m_β^2 are shown in the inset, with the literature values for the endpoint energy [72, 73] and neutrino mass [8] close to the 1σ contour. The shape of the contours for $m_\beta^2 < 0$ and the lower limit given in the third row of Tab. IX depend on the choice of function for the non-physical regime, here chosen to be Eq. 20.

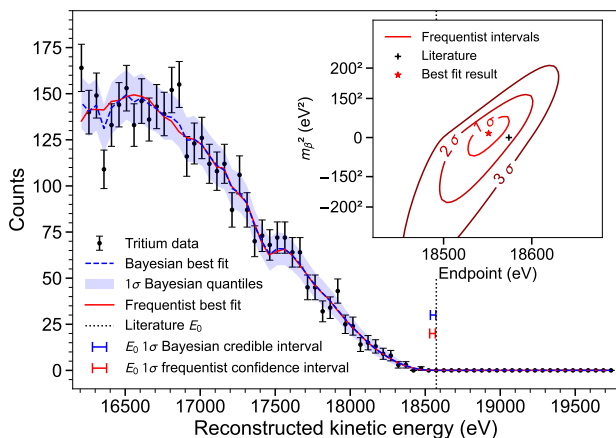


FIG. 30. Results: Measured tritium beta-decay spectrum with Bayesian and frequentist fits, as well as endpoint intervals from each analysis. (Inset) Frequentist neutrino mass and endpoint contours. The literature sources for the endpoint energy are [72, 73] and for the mass the source is [8].

B. Background limit

Zero counts were observed in the spectrum above the tritium endpoint energy. From this a background limit of $3 \times 10^{-10} \text{ eV}^{-1} \text{ s}^{-1}$ at 90% C.L. is obtained. If the background is energy independent and Poisson distributed with a mean number μ of events in the 50-eV wide analysis window ΔE defined below in Eq. 23, then the probability of there being a single background event in the window and zero events in the 1050 eV (21 bins) above the endpoint is

$$P = \frac{\mu^1 e^{-\mu}}{1!} \frac{\mu^0 e^{-21\mu}}{0!}. \quad (22)$$

The probability maximizes at 1.7% for $\mu = 1/22 = 0.045$. The bulk of the probability is for zero events in the analysis window; numbers > 1 are highly improbable. In the following section, Sec. XC, we compare the experimental limit on the neutrino mass with the prediction of an analytic model. The analytic model assumes Gaussian statis-

tics. A mean Gaussian rate of $b = 4.7 \times 10^{-11} \text{ eV}^{-1} \text{ s}^{-1}$ for the background reproduces the probability in the analysis window for the sensitivity calculation.

C. Neutrino mass sensitivity

Project 8 has developed and made extensive use of a simple analytic model for predicting the sensitivity of differential spectrometers to neutrino mass. In the model, the size of the neutrino mass m_β is deduced from the count rate in a part of the spectrum of width ΔE contiguous with the endpoint. The width of this “analysis window” is optimized with respect to the background rate b , energy resolution ΔE_{res} , and any other contributions to line broadening such as the final-state distribution in molecular T_2 beta decay. Systematic contributions from imperfect knowledge of the resolution contributions are added in quadrature with the statistical contribution. A complete description of the model may be found in [7].

The analytic sensitivity prediction model can now be confronted with data (for the first time) in Phase II. Table XI lists relevant parameters. We first calculate the effective volumes V_{eff} from the magnetic field B and the range of pitch angles that can be accommodated without exceeding a modulation index of 1, or equivalently an axial amplitude of 2.8 mm (see Tab. I).

Only a subset of electrons trapped within this axial range is detectable above the noise threshold, mainly because electrons at larger radii couple less strongly to the propagating TE_{11} waveguide mode. We compute detection efficiencies by generating simulated tracks in all 4 traps, selecting the subset with average minimum pitch angles of 89.37 degrees (see Tab. I), and passing those events through triggering and T&ER (track and event reconstruction) processors. These efficiencies are correlated and the net detection efficiency is not simply the product of the two. The results are in Fig. 31.

The density (hydrogen equivalent) found from track length data is $2.09 \times 10^{17} \text{ m}^{-3}$, with an effective T_2 density of $7.45 \times 10^{16} \text{ m}^{-3}$ from mass spectrometer data. The balance is inactive hydrogen, with a small amount of helium that is treated as hydrogen for these purposes. The standard deviation in the neutrino mass is taken from the frequentist analysis of the Phase II data. It is derived with the endpoint energy E_0 and background b floating, which is the assumption made in deriving the sensitivity curves. We use only the positive side of the 1-standard-deviation uncertainty range of the data point, because the best-fit value is in the positive, physical regime. Negative fit values require a functional form to be chosen for the negative regime [7].

In Fig. 32, we compare the measured sensitivity from the Phase II analysis described above to the predicted sensitivity for this apparatus and running time. For the theoretical curves, the analysis window ΔE is the quadrature sum of $\sqrt{b\epsilon_0^3/r} \simeq 22 \text{ eV}$ and the resolution, about 50 eV FWHM, where r is the rate in a small interval ϵ_0

TABLE XI. Calculation of Phase II sensitivity, and comparison to analytic sensitivity.

Parameter	Value	Fractional Uncertainty	Absolute Uncertainty	Unit
Total effective volume	14.6		1.2	mm ³
Trigger efficiency	0.229		0.003	
T&ER efficiency	0.101		0.002	
Combined trigger, T&ER	0.082	0.024	0.002	
Mean track duration	156	0.07		μs
Total cross section	3.9×10^{-22}	0.05		m ²
Electron speed	0.2625c			
Density as if all HDT	2.09×10^{17}	0.09		m ⁻³
Hydrogen fraction	0.918	0.046		
Activity fraction T/HDT	0.389	0.1		
T ₂ density	7.45×10^{16}	0.14		m ⁻³
Background (Poissonian)	$< 3 \times 10^{-10}$			eV ⁻¹ s ⁻¹
Detectable source activity	0.32			Bq
Detectable rate $r\epsilon_0^{-3}$	9.5×10^{-14}			eV ⁻³ s ⁻¹
Volume × Efficiency	1.20	0.09		mm ³
Run time	7185228	0.008		s
m_β^2 (E_0 free, no sys.)	2473		+9822 -13233	eV ²
$\sigma(m_\beta^2)$	9822		1520	eV ²

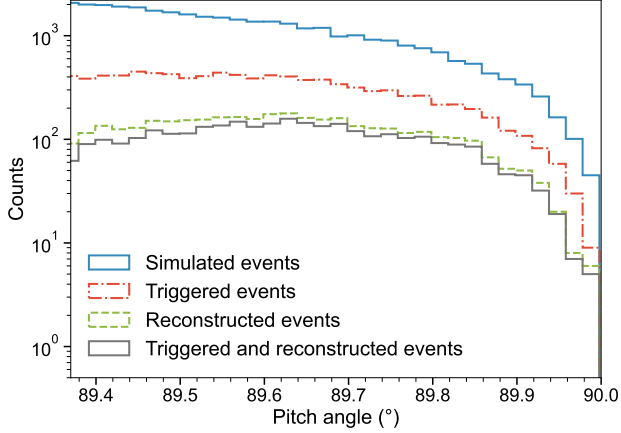


FIG. 31. Number of simulated trapped electrons vs. pitch angle (blue) in the quad trap. The grey histogram shows the subset of events that were detected by the DAQ trigger (red) and the reconstruction methods (green). From the fraction of detected events the efficiency vs. pitch angle is determined.

contiguous with the endpoint. Reduced to the bare essentials, the optimum analysis window and the uncertainty in m_β^2 are

$$\Delta E \simeq \sqrt{\frac{b\epsilon_0^3}{r} + (\Delta E_{\text{res}})^2}, \quad (23)$$

$$\sigma_{m_\beta^2} \simeq \frac{2}{3} \sqrt{\frac{\epsilon_0^3}{rt} \left(\Delta E + \frac{b\epsilon_0^3}{r\Delta E} \right)}, \quad (24)$$

where t is the run time and ΔE_{res} is the FWHM of the

combined resolution contributions. In regimes where ΔE is dominated by ΔE_{res} , the curves fall with a logarithmic slope of $-1/2$. Where ΔE is dominated by $b\epsilon_0^3/r$, the slope steepens to $-3/4$. The curves flatten out when systematic uncertainties become important, in this case taken to be a 1% uncertainty in the resolution. The curves shown in Fig. 32(a) are calculated for a run time of 3×10^7 s and the effective volume for the Phase II data point is scaled to the actual run time. This rescaling is strictly only valid in the regime dominated by ΔE_{res} because the signal scales with volume and time while the background scales only with time. The expanded view in panel (b) is calculated with the actual running time of 82 days. The sensitivity determined for Phase II agrees well with the sensitivity curve.

D. Considerations for future designs

A major motivation in Phase II of Project 8 was to obtain information of value for the future scaling up of the CRES technology for neutrino mass measurement. The waveguide CRES cell is quite efficient in coupling the electron to the propagating electromagnetic field. However, because the electron's guiding center in the trap moves along the direction of propagation, the Doppler effect is maximal. This limits the pitch-angle range that can be used, and hence the efficiency with which useful signals can be obtained from the gas in the trap region. Two approaches to circumventing this limitation in a large volume are to use an antenna array that is directed at signals emitted by the electron perpendicular to its axial motion, and to use a resonant cavity wherein the

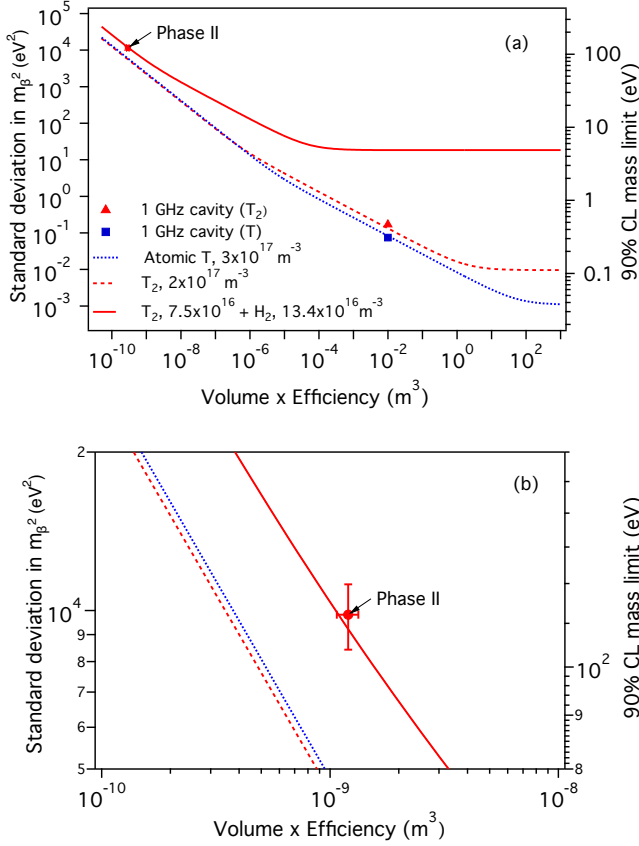


FIG. 32. (a) Statistical uncertainty in neutrino mass from Phase II data compared to the predicted sensitivity for a T_2 density of 7.5×10^{16} molecules m^{-3} , resolution of 50 eV FWHM, and a background limit of $3 \times 10^{-10} \text{ eV}^{-1} \text{ s}^{-1}$ (90% C.L.). The data point is from the frequentist analysis. The evolution with volume and efficiency is shown for experiments run for 3×10^7 s: with the Phase II gas mixture, resolution and background (red solid line); with improved resolution (1.5 eV FWHM), and pure T_2 (red dashed line); and with atomic T for 0.5 eV FWHM resolution and a density that optimizes the experimental reach in neutrino mass (blue dotted line). Systematic uncertainties have not been fully quantified, however. (b) Expanded view of the region with the Phase II data point and the actual run time of 7.2×10^6 s. Uncertainty in the gas density is included with the data point rather than by broadening the theoretical curve.

phase velocity is much larger and the Doppler shift correspondingly smaller. The sensitivities of large-volume cavity experiments are marked in Fig. 32.

The CRES method is inherently capable of high resolution, as may be seen simply from the widths of tracks in Fig. 4. These tracks are roughly a single bin wide in frequency space, about 1 part per million, which corresponds to an energy width at the tritium endpoint of 0.5 eV. That measure of the intrinsic resolution depends on the signal-to-noise ratio, and the system noise temperature in Phase II was about 132 K when the CRES cell was at 85 K. Substantially lower physical temper-

atures can be realized, especially for atomic tritium in a magnetic trap. The total experimental resolution has other contributions, primarily the varying magnetic field experienced by electrons moving in a trap that may itself not be ideal, with spatial inhomogeneities and temporal instabilities.

The zero background observed is both encouraging and expected. In the CRES method there are no physical detectors for electrons (for example, silicon detectors) that can be background sources due to radioactivity and cosmic rays. Cosmic ray interactions with the source gas itself are negligible even for very large-scale versions. Electrons or gammas from external radioactivity do not produce trapped electrons unless an interaction with a gas atom occurs. In a differential spectrometer, to be a background, an event must not merely be present but must also be in the right energy range. Electrons in a CRES system are not slowed nearly to rest and reaccelerated as in a retarding-field analyzer, and the counting of ubiquitous slow electrons is thereby avoided. The primary background that remains is false tracks created by random aggregations of noisy pixels. It is that background that was the target of a detailed study before data-taking began in Phase II, so that a power threshold could be set to limit false events to less than 1 in 100 days at 90% C.L. The success of this strategy is one of the most important conclusions of this study. A good signal-to-noise ratio is key to eliminating this background at minimal cost in efficiency, and in future CRES designs it is a basic requirement.

With the waveguide-based CRES apparatus described in this work, we have carried out the first measurement of the tritium beta spectrum by this new method. We report an upper limit on neutrino mass at 90% C.L. of 155 (152) eV in a Bayesian (frequentist) analysis. In both analyses, the extrapolated endpoint energy for molecular T_2 decay and the neutrino mass limit are found to be consistent with literature values obtained by traditional methods. No background events were observed in the 82-day running period. These results from a small-scale apparatus are the first steps in a phased approach to a CRES-based experiment with high sensitivity to neutrino mass.

ACKNOWLEDGMENTS

This material is based upon work supported by the following sources: the U.S. Department of Energy Office of Science, Office of Nuclear Physics, under Award No. DE-SC0020433 to Case Western Reserve University (CWRU), under Award No. DE-SC0011091 to the Massachusetts Institute of Technology (MIT), under Field Work Proposal Number 73006 at the Pacific Northwest National Laboratory (PNNL), a multiprogram national laboratory operated by Battelle for the U.S. Department of Energy under Contract No. DE-AC05-76RL01830, under Early Career Award No. DE-

SC0019088 to Pennsylvania State University, under Award No. DE-FG02-97ER41020 to the University of Washington, and under Award No. DE-SC0012654 to Yale University; the National Science Foundation under Award No. PHY-2209530 to Indiana University, and under Award No. PHY-2110569 to MIT; the Cluster of Excellence “Precision Physics, Fundamental Interactions, and Structure of Matter” (PRISMA+ EXC 2118/1) funded by the German Research Foundation (DFG) within the German Excellence Strategy (Project ID 39083149); the Karlsruhe Institute of Technology (KIT) Center Elementary Particle and Astroparticle Physics (KCETA); Laboratory Directed Research and

Development (LDRD) 18-ERD-028 and 20-LW-056 at Lawrence Livermore National Laboratory (LLNL), prepared by LLNL under Contract DE-AC52-07NA27344, LLNL-JRNL-845409; the LDRD Program at PNNL; Indiana University; and Yale University. Portions of the research were performed using the Core Facility for Advanced Research Computing at CWRU, the Engaging cluster at the MGHPCC facility, Research Computing at PNNL, and the HPC cluster at the Yale Center for Research Computing. The $^{83}\text{Rb}/^{83\text{m}}\text{Kr}$ isotope used in this research was supplied by the United States Department of Energy Office of Science through the Isotope Program in the Office of Nuclear Physics.

-
- [1] Y. Fukuda *et al.* (Super-Kamiokande), *Phys. Rev. Lett.* **81**, 1562 (1998), arXiv:hep-ex/9807003.
- [2] Q. Ahmad *et al.* (SNO), *Phys. Rev. Lett.* **87**, 071301 (2001), arXiv:nucl-ex/0106015.
- [3] B. Pontecorvo, *Sov. Phys. JETP* **6**, 429 (1957).
- [4] Z. Maki, M. Nakagawa, and S. Sakata, *Prog. Theor. Phys.* **28**, 870 (1962).
- [5] P. A. Zyla *et al.* (Particle Data Group), *Prog. Theor. Exp. Phys.* **2020**, 10.1093/ptep/ptaa104 (2020), 083C01.
- [6] N. Aghanim *et al.* (Planck), *Astron. Astrophys.* **641**, A6 (2020), [Erratum: *Astron. Astrophys.* 652, C4 (2021)], arXiv:1807.06209 [astro-ph.CO].
- [7] J. A. Formaggio, A. L. C. de Gouvêa, and R. G. H. Robertson, *Phys. Rept.* **914**, 1 (2021), arXiv:2102.00594 [nucl-ex].
- [8] M. Aker *et al.* (KATRIN), *Nature Phys.* **18**, 160 (2022), arXiv:2105.08533 [hep-ex].
- [9] M. Aker *et al.* (KATRIN), *J. Instrum.* **16** (08), T08015, arXiv:2103.04755 [physics.ins-det].
- [10] M. Aker *et al.* (KATRIN), *J. Phys. G* **49**, 100501 (2022).
- [11] N. Doss, J. Tennyson, A. Saenz, and S. Jonsell, *Phys. Rev. C* **73**, 025502 (2006).
- [12] A. Saenz, S. Jonsell, and P. Froelich, *Phys. Rev. Lett.* **84**, 242 (2000).
- [13] Y. T. Lin *et al.* (TRIMS), *Phys. Rev. Lett.* **124**, 222502 (2020), arXiv:2001.11671 [nucl-ex].
- [14] A. Ashtari Esfahani *et al.* (Project 8), *J. Phys. G* **44**, 054004 (2017), arXiv:1703.02037 [physics.ins-det].
- [15] A. Ashtari Esfahani *et al.* (Project 8), *Phys. Rev. C* **103**, 065501 (2021), arXiv:2012.14341 [physics.data-an].
- [16] B. Monreal and J. A. Formaggio, *Phys. Rev. D* **80**, 051301 (2009), arXiv:0904.2860 [nucl-ex].
- [17] D. M. Asner *et al.* (Project 8), *Phys. Rev. Lett.* **114**, 162501 (2015), arXiv:1408.5362 [physics.ins-det].
- [18] A. Ashtari Esfahani and the rest of P8, *Phys. Rev. Lett.* (2022).
- [19] A. Ashtari Esfahani *et al.* (Project 8), in preparation (2023).
- [20] A. Ashtari Esfahani *et al.* (Project 8), *Phys. Rev. C* **99**, 055501 (2019), arXiv:1901.02844 [physics.ins-det].
- [21] D. Vénos, A. Spalek, O. Lebeda, and M. Fiser, *Appl. Radiat. Isot.* **63**, 323 (2005).
- [22] C. Colmenares, E. G. Shapiro, P. E. Barry, and C. T. Prevo, *Nucl. Instrum. Methods* **114**, 277 (1974).
- [23] J. Hickish *et al.* (CASPER), *J. Astron. Instrum.* **5**, 1641001-12 (2016), arXiv:1611.01826 [astro-ph.IM].
- [24] D. L. Furse, *Techniques for direct neutrino mass measurement utilizing tritium [beta]-decay*, Ph.D. thesis, Massachusetts Institute of Technology (2015).
- [25] A. Ashtari Esfahani *et al.* (Project 8), in preparation (2023).
- [26] A. A. Esfahani *et al.* (Project 8), in preparation (2023).
- [27] D. D. Joy, in *Monte Carlo Modeling for Electron Microscopy and Microanalysis* (Oxford University Press, 1995) Chap. 3.
- [28] V. Aseev *et al.*, *Eur. Phys. J. D* **10**, 39 (2000).
- [29] J. W. Liu, *Phys. Rev. A* **35**, 591 (1987).
- [30] S. T. Perkins, D. E. Cullen, and S. M. Seltzer, *ge.infn.it* (1991), UCRL-50400.
- [31] P. Nagy, A. Skutlartz, and V. Schmidt, *J. Phys. B* (1968-1987) **13**, 1249 (1980).
- [32] R. S. Brusa, G. P. Karwasz, and A. Zecca, *Z. Phys. D* **38**, 279 (1996).
- [33] A. Zecca, G. P. Karwasz, and R. S. Brusa, *J. Phys. B* **33**, 843 (2000).
- [34] D. C. Cartwright, G. Csanak, S. Trajmar, and D. F. Register, *Phys. Rev. A* **45**, 1602 (1992).
- [35] W. Hwang, Y. K. Kim, and M. E. Rudd, *J. Chem. Phys.* **104**, 2956 (1996).
- [36] D. Rapp and P. Englander Golden, *J. Chem. Phys.* **43**, 1464 (1965).
- [37] I. Kanik, S. Trajmar, and J. C. Nickel, *J. Geophys. Res. E Planets* **98**, 7447 (1993).
- [38] B. Carpenter, A. Gelman, M. Hoffman, D. Lee, B. Goodrich, M. Betancourt, M. Brubaker, J. Guo, P. Li, and A. Riddell, *J. Stat. Softw., Articles* **76**, 1 (2017).
- [39] M. Inokuti, *Rev. Mod. Phys.* **43**, 297 (1971).
- [40] W. F. Chan, G. Cooper, and C. E. Brion, *Phys. Rev. A* **44**, 186 (1991).
- [41] W. Chan, G. Cooper, X. Guo, G. Burton, and C. Brion, *Physical Review A* **46**, 149 (1992).
- [42] T. N. Olney, N. Cann, G. Cooper, and C. Brion, *Chemical physics* **223**, 59 (1997).
- [43] E. Carbone, W. Graef, G. Hagelaar, D. Boer, M. M. Hopkins, J. C. Stephens, B. T. Yee, S. Pancheshnyi, J. van Dijk, and L. Pitchford, *Atoms* **9**, 16 (2021).
- [44] L. C. Pitchford, L. L. Alves, K. Bartschat, S. F. Biagi, M.-C. Bordage, I. Bray, C. E. Brion, M. J. Brunger, L. Campbell, A. Chachereau, *et al.*, *Plasma Processes*

- and *Polymers* **14**, 1600098 (2017).
- [45] S. Pancheshnyi, S. Biagi, M.-C. Bordage, G. Hagelaar, W. Morgan, A. Phelps, and L. C. Pitchford, *Chemical Physics* **398**, 148 (2012).
- [46] The Plasma Data Exchange Project, Lxcat data base (2022), <https://fr.lxcat.net>.
- [47] A. Ashtari Esfahani *et al.* (Project 8), *New J. Phys.* **21**, 113051 (2019), arXiv:1907.11124 [physics.comp-ph].
- [48] R. G. H. Robertson and V. Venkatapathy, *Phys. Rev. C* **102**, 035502 (2020).
- [49] D. Vénos, J. Sentkerestiová, O. Dragoun, M. Slezák, M. Ryšavý, and A. Špalek, *J. Instrum.* **13** (02), T02012.
- [50] C. Rodenbeck, *Eur. Phys. J. C* **82**, 700 (2022), arXiv:2205.01484 [physics.ins-det].
- [51] S. Baker and R. D. Cousins, *Nucl. Instrum. Methods Phys. Res.* **221**, 437 (1984).
- [52] K. Altenmüller *et al.* (KATRIN), *J. Phys. G* **47**, 065002 (2020), arXiv:1903.06452 [physics.ins-det].
- [53] M. E. Rudd, *Physical Review A* **44**, 1644 (1991).
- [54] Stan modeling language users guide and reference manual, version 2.30 (2022), Stan Development Team.
- [55] M. Betancourt, arXiv e-prints, arXiv:1701.02434 (2017), arXiv:1701.02434 [stat.ME].
- [56] R. G. H. Robertson and D. A. Knapp, *Annu. Rev. Nucl. Part. Sci.* **38**, 185 (1988).
- [57] M. Guigue, J. A. Formaggio, J. Johnston, J. Kofron, B. LaRoque, N. S. Oblath, and T. E. Weiss, *Morpho* (2021), doi:10.5281/zenodo.5117728.
- [58] M. Betancourt, *Toward a principled Bayesian workflow (PyStan)* (2018), retrieved from https://github.com/betanalphabet/jupyter_case_studies/tree/master/principled_bayesian_workflow, commit 2580fdeac38f77859b2d1c60f9c4a37237864e63.
- [59] A. Gelman, J. B. Carlin, H. S. Stern, D. B. Dunson, A. Vehtari, and D. B. Rubin, *Bayesian Data Analysis*, 3rd ed. (Chapman and Hall/CRC, 2014) Chap. 2.
- [60] A. Gelman, *Prior choice recommendations* (2020).
- [61] M. Betancourt, *Stan Documentation: How the Shape of a Weakly Informative Prior Affects Inferences* (2017).
- [62] G. D’Agostini, *Rep. Prog. Phys.* **66**, 1383 (2003), arXiv:0304102 [physics.data-an].
- [63] C. Kraus *et al.* (Mainz), *Eur. Phys. J. C* **40**, 447 (2005), arXiv:hep-ex/0412056.
- [64] H. Dembinski and P. Ongmongkolkul 10.5281/zenodo.3949207 (2020).
- [65] F. James and M. Roos, *Comput. Phys. Commun.* **10**, 343 (1975).
- [66] B. A. Murtagh and M. A. Saunders, *Mathematical Programming* **14**, 41 (1978).
- [67] G. Cowan, K. Cranmer, E. Gross, and O. Vitells, *Eur. Phys. J. C* **71**, 1554 (2011), [Erratum: *Eur.Phys.J.C* **73**, 2501 (2013)], arXiv:1007.1727 [physics.data-an].
- [68] G. J. Feldman and R. D. Cousins, *Phys. Rev. D* **57**, 3873 (1998), arXiv:physics/9711021.
- [69] R. L. Workman *et al.* (Particle Data Group), *PTEP* **2022**, 083C01 (2022).
- [70] M. Kleesiek *et al.*, *Eur. Phys. J. C* **79**, 204 (2019), arXiv:1806.00369 [physics.data-an].
- [71] S. R. Cook, A. Gelman, and D. B. Rubin, *J. Comput. Graph. Stat.* **15**, 675–92 (2006).
- [72] L. I. Bodine, D. S. Parno, and R. G. H. Robertson, *Phys. Rev. C* **91**, 035505 (2015), arXiv:1502.03497 [nucl-ex].
- [73] E. G. Myers, A. Wagner, H. Kracke, and B. A. Wesson, *Phys. Rev. Lett.* **114**, 013003 (2015).